APPLICATIONS OF THE GUIDED-MODE RESONANCE SENSOR IN MULTIPARAMETRIC, TRANSMISSIVE, AND PICOMOLAR REGIMES

by

JOSEPH ANTHONY BUCHANAN-VEGA

DISSERTATION

Submitted in partial fulfillment of the requirements
for the degree of Doctor of Philosophy at
The University of Texas at Arlington
December, 2023

Arlington, Texas

Supervising Committee:

Robert Magnusson, Supervising Professor
Minerva Cordero
Jonathan Bredow
Yeong Hwan Ko

Acknowledgements

I truly appreciate Professor Robert Magnusson for being a consistent force in my journey through my doctoral studies. His concise advice, and high expectations have given me perspective on achievement in academia and industry.

I owe Dr. Mohammad G. Abdallah a debt of gratitude for serving as a mentor through a key time in my doctoral degree process. I am grateful to Dr. Kyu Jin Lee for helping me learn and apply the fabrication principles that have been integral to my scholarly work. I am grateful to Dr. Yeong Hwan Ko; he has been a valuable source of knowledge in the field of nanophotonics. I am very thankful to Dr. Minerva Cordero for her unwavering belief in my abilities as a scholar.

Thank you to my colleagues former and current in the Nanophotonics Device Group: Dr. Alex Fannin, Dr. Daniel Carney, Dr. Sun-Goo Lee, Dr. Subrata Das, Dr. Pawarat (Fern) Bootpakdeetam, Nasrin Razmjooei, Ren-Jie Chen, Fairooz Simlan, and Robert Wood.

I truly appreciate the friends that I have made through UTA NSBE. They have motivated me to persevere and helped me stay engaged during my doctoral studies.

October 7, 2023

Dedications

I dedicate this work

To my wife Lauren Buchanan-Vega

for showing me love and lightening my load

To my mother Brenda and my father Ishmael Vega

for teaching me how to stay positive, and how to maintain my integrity and character

To my grandmother Elaine White

for guiding me along the trail she blazed

To my grandmother Marie Buchanan

for keeping me spiritually grounded and rooted in God

To my sister, my nephews, and my in-laws

for your words of encouragement and for the many fond memories we created

To my friends

for laughter, motivation, and support

I am extremely blessed to have all of you in my life.

Joseph Buchanan-Vega

October 7, 2023

Abstract

APPLICATIONS OF THE GUIDED-MODE RESONANCE SENSOR IN MULTIPARAMETRIC, TRANSMISSIVE, AND PICOMOLAR REGIMES

JOSEPH ANTHONY BUCHANAN-VEGA, Ph.D.

The University of Texas at Arlington, 2023

Supervising Professor: Robert Magnusson

Guided-mode resonance (GMR) sensors are developed and implemented for multiparametric label-free sensing, transmission sensing, enhanced reflection sensing, and low analyte concentration sensing; these are the topics presented in this work. The complete biosensor – capable of label-free multiparametric data collection – is designed, fabricated, and implemented. Multiparametric data collection has previously been relegated to one variable on the sensor surface and one bulk media variable. We use a lookup table and the novel application of an inversion algorithm to simultaneously determine two variables on the sensor surface and one bulk media variable.

Multiparametric data sets are required to monitor multiple variables in one spectral measurement. Interpreting and deconvolving this spectral data can be done in a myriad of ways with varying degrees of success. We explore different coding algorithm concepts to interpret multimode data.

GMR sensors primarily use the reflection response of resonant structures. We introduce a replicable method to design GMR-assisted Rayleigh sensors dependent on guided-modes shaping

the spectral profile which allows the Rayleigh anomaly to produce a transmittance peak. The Rayleigh sensor designs have transmission peaks that shift by one device period per RIU. Multiple high-performance transmissive devices are presented.

Development of high sensitivity reflection GMR sensors is a prevalent concept in the GMR biosensor field. It is found that the addition of a thin silicon layer produces mode confinement in/near the bulk media of a sensor and increases the sensitivity of reflection based GMR sensors.

Lastly, we present a sandwich detection method to improve the limit of detection of neuropeptide Y (NPY) molecules that adhere to a GMR sensors functionalized surface. The sandwich detection method yields a 20-fold increase in the limit of detection of NPY molecules: these molecules are significant in the physical and emotional trauma response in the human brain.

Through this work we explore guided-mode resonance (GMR) devices implemented for multiparametric sensors, transmission applications, high sensitivity sensors, and low concentration biomolecule detection. Each of these designs and applications are significant when considering the wide range of implementation of GMR sensors.

Table of Contents

Acknowledgements iii

Dedications iv

Abstract v

List of Illustrations xi

Chapter 1 Introduction and background 1

Chapter 2 Multiparametric guided-mode resonance biosensors 4

2.1 Summary 4

2.2 Introduction 5

2.3 Experiments and methods 11

2.3.1 Fabricated sensor specifications 11

2.3.2 Yeast cell preparation 13

2.3.3 Sensor surface functionalization 13

2.3.4 Inversion: translating resonant shifts to sensor variables 14

2.4 Results and discussion 17

2.4.1 Lookup table 17

2.4.2 Simulated input wavelengths compared to the calculated output sensor variable values 21

2.4.3 Measured resonance shifts and inversion for Con A incubation 23

2.4.4 Measured resonance shifts and inversion for yeast incubation 28

2.5 Conclusions 32

Chapter 3 Best fit line inversion algorithm 33

3.1 Inversion results 35

3.2 Simulated input wavelength shifts and best fit line algorithm output 39

3.3 Trends in inversion accuracy 42

3.4 Conclusion 43

Chapter 4 Rayleigh-anomaly-transmission sensors assisted by modal resonance effects 44

4.1 Physics behind transmission GMR 44

4.2 Past implementation of transmission resonance in GMR devices 44

4.3 Design parameters 47

4.3.1 Favorable spectrum description 48

4.4 Rayleigh sensor characterization 54

4.4.1 Additional Rayleigh sensor designs 57

4.5 Discussion 59

4.5.1 Coupling orders 59

4.5.2 Resonance-assisted Rayleigh sensor substrate options 67

4.5.3 Rayleigh sensor explanation 72

4.6 Conclusion 73

Chapter 5 Silicon-enhanced GMR sensors 74

5.1 Introduction 74

5.1.1 Multiparametric GMR sensor 74
5.1.2 Silicon-incorporated multiparametric sensor 77
5.1.3 Silicon-incorporated high-Q sensor 81
5.1.4 Si-incorporated fiber-faceted-integrated sensor 83
5.1.5 Silicon-incorporated sensor fabrication 87
5.2 Sensor EM field distribution 87
5.2.1 Multiparametric sensor EM field distribution 87
5.2.2 High-Q sensor EM field distribution 93
4.3.3 Fiber-facet-integrated sensor EM field distribution 94
5.3 Conclusion 96
Chapter 6 GMR enabled quantification of neuropeptide Y 98
6.1 Introduction 98
6.2 Materials and methods 101
6.2.1 Materials and instruments 101
6.2.2 Sensor plate preparation 102
6.2.3 Surface immobilization of avidin-D 106
6.2.4 Surface Immobilization of anti-NPY [biotin] 107
6.2.5 Sandwich NPY assay 107
6.3 Results and discussion 108
6.3.1 Avidin-D characterized 108

6.3.2 Anti-NPY characterization 109

6.3.3 Sandwich NPY assay.....110

6.4 Conclusions.....113

Chapter 7 Future work.....115

List of publications 117

References.....118

Biographical Information..... 126

List of Illustrations

Figure 1-1 Diagram of a guided-mode resonance sensor (GMR)..... 1

Figure 2-1 Multiparametric sensor..... 10

Figure 2-2 AFM data for the multiparametric sensor. 12

Figure 2-3 Schematic of the sensor layout..... 13

Figure 2-4 Bulk index shift vs. resonant wavelength shift. 19

Figure 2-5 Visual representation of the lookup table..... 20

Figure 2-6 Multiparametric sensor reflection response. 24

Figure 2-7 Multiparametric sensor in Con A response over time. 26

Figure 2-8 Resonance shift during Con A incubation..... 27

Figure 2-9 Biolayer variable shift vs. time due to Con A. 27

Figure 2-10 Yeast concentration vs. resonance shift..... 28

Figure 2-11 Multiparametric sensor in yeast response over time. 30

Figure 2-12 Resonance shift during yeast incubation..... 31

Figure 2-13 Biolayer variable shift vs. time due to yeast. 31

Figure 3-1 Planes of inversion values for resonant modes. 35

Figure 3-2 Inversion biolayer shift values. 38

Figure 4-1 TE-polarization transmission colormap for wavelength vs. fill-factor. 47

Figure 4-2 TE-polarization transmission colormap for wavelength vs. waveguide thickness. 49

Figure 4-3 TE-polarization sensor response to optimize waveguide thickness..... 50

Figure 4-4 TE-polarization transmission colormap for wavelength vs. grating thickness. .. 52

Figure 4-5 TE-polarization wavelength vs. transmissivity for grating thickness optimization. 53

Figure 4-6 Optimized GMR-assisted Rayleigh transmission sensor. 55

Figure 4-7 Performance of the sensor in **Figure 4-6**. 56

Figure 4-8 Second optimized sensor schematic and performance. 57

Figure 4-9 Third optimized sensor schematic and performance. 58

Figure 4-10 Neighboring GMR assists Rayleigh transmission peak for the sensor in **Figure 4-6** 61

Figure 4-11 Rayleigh anomaly produced by the sensor in **Figure 4-6** with substrate index of refraction set to 3.0 RIU. 61

Figure 4-12 Two neighboring guided-mode resonances assist the Rayleigh transmission peak for the sensor in **Figure 4-8**a 63

Figure 4-13 Rayleigh anomaly produced by the sensor in **Figure 4-8**a with substrate index of refraction set to 3.75 RIU. 64

Figure 4-14 Two neighboring guided-mode resonances assist the Rayleigh transmission peak for the sensor in **Figure 4-9**a 66

Figure 4-15 The Rayleigh anomaly produced by the sensor in **Figure 4-9**a with substrate index of refraction set to 3.75 RIU. 67

Figure 4-16 The TE-polarization transmissivity vs. wavelength for the sensor in **Figure 4-8**a. 68

Figure 4-17 The TE-polarization transmissivity vs. wavelength for the sensor in **Figure 4-9**a. 69

Figure 4-18 The device response from the sensor in **Figure 4-6** with varied substrate. 71

Figure 5-1 Multiparametric sensor TM sensitivity. 76

Figure 5-2 Multiparametric sensor TE sensitivity..... 77

Figure 5-3 Multiparametric sensor schematic implementing the GMR sensor in **Figure 5-1**a with a thin layer of silicon on top of the grating..... 78

Figure 5-4 Silicon-enhanced multiparametric sensor TM data..... 79

Figure 5-5 Silicon-enhanced multiparametric sensor TE data..... 80

Figure 5-6 High-Q sensor. 82

Figure 5-7 Silicon-enhanced high-Q sensor performance. 83

Figure 5-8 Fiber-faceted-integrated (FFI) sensor TE spectrum and sensitivity. 84

Figure 5-9 Silicon-enhanced fiber-faceted-integrated (FFI) sensor performance. 86

Figure 5-10 Multiparametric sensor TM_1 fields. 89

Figure 5-11 Multiparametric sensor TE_2 fields..... 91

Figure 5-12 Multiparametric sensor TE_1 fields. 92

Figure 5-13 High-Q sensor TE fields..... 94

Figure 5-14 FFI sensor TE_1 fields..... 96

Figure 6-1 RSI sensor**. .....** 104

Figure 6-2 The sandwich neuropeptide Y (NPY) assay principle used in this work. 106

Figure 6-3 Avidin-D incubation. 109

Figure 6-4 Biotin incubation. 110

Figure 6-5 NPY sandwich incubation. 112

Figure 6-6 GMR NPY detection. 113

Chapter 1

Introduction and background

Rapid spectral variations produced by subwavelength waveguide gratings arise upon excitation of guided-mode resonance (GMR) by an incident beam of light [1]–[6]. The output of GMR devices is generally characterized by their spectral reflection response, but transmission based devices have also be designed [7]–[15]. The figure below diagrams a GMR device and its parameters.

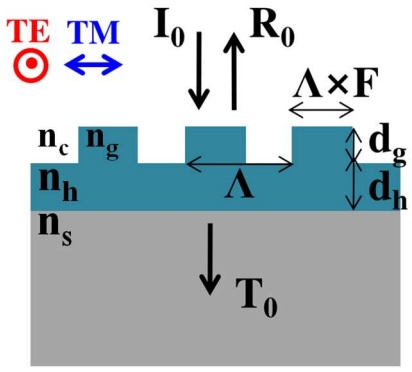

Figure 1-1 Diagram of a guided-mode resonance sensor (GMR). The substrate is gray region, the waveguide is indicated by d_h, the grating is indicated by d_g, the region above the grating is the cover [16].

In the figure above. I_0, R_0, and T_0 are the zero-orders of incident, reflected and transmitted light, respectively. Λ, F, d_g, and d_h are the period, fill factor, grating thickness, and waveguide thickness, respectively. n_c, also known as n_{bulk}, is the index of refraction of the cover. n_g, n_h, and n_s are the index of refraction of the grating material, the waveguide, and the substrate, respectively. TE is the transverse electric light which has its electric field parallel to the grating

grooves. TM is the transverse magnetic light which has its electric field perpendicular to the grating grooves.

Guided mode resonance (GMR) utilized to detect biomolecules and changes in the bulk surrounding environment has been studied by many research groups. There are studies that focus on implementing GMR sensors to detect a particular analyte. There are also studies that explore enhancing the effectiveness of GMR devices as sensors. It is of value to have an overview of the past work done using GMR devices as sensors.

Magnusson et al. utilized a multiparametric GMR biosensor to simultaneously quantify biolayer thickness change and background index change [17]. Meleki et al. analyzed the performance of different GMR grating types to tailor the sensor selection for gas sensing, moderate index liquid sensing, and high index liquid sensing [18]. GMR sensors have been used to detect a surface layer of yeast involved in biofouling [19]. Kaja et al. have used GMR sensors to detect protein biomarkers for ovarian cancer [20]. A PDMS grating coated with compounds that detect hazardous chemicals has been shown to detect volatile organic compounds with enough predictability to institute machine learning [21]. Joo et al. designed device using long-range plasmon polaritons for refractive index sensing and temperature determination [22]. Ramano et al. used a 2D GMR device of periodically placed holes to generate a BIC for biolayer sensing [23]. These works and numerous others focus on using GMR sensors to quantify biolayer and bulk changes.

Mesli et al. studied bulk refractive index GMR sensors – utilizing bound states in the continuum (BIC): that form reflection peaks at off normal incidence – to achieve an optimal sensor design [24]. Lan et al. designed a GMR sensor working at a high angle of incidence with high sensitivity in the IR range and a high figure of merit [25]. Dual GMR structures working in

concert have been used to enhance bulk RIU sensitivity [26]. GMR sensors with asymmetric gratings and metal sublayers have been simulated to increase field concentration in the bulk media and thus bulk RIU sensitivity [27]. Vyas et al. investigated perturbations in the width of grating pillars and perturbations in gaps between grating pillars to design a device with a high bulk and biolayer sensitivity, and a high figure of merit [28]. Through this work it was found that simultaneous implementation of both perturbations produced two resonances in the spectrum of interest (visible spectrum) instead of the one original resonance. The resonances produced are quasi-BICs, and the resonant peaks are sensitive to bulk and surface changes in refractive index. These studies, and several others, focus on enhancing the response of a GMR sensor in ways that suit several sensing applications [29]–[31].

The chapters in this dissertation detail projects on the enhancement of GMR sensors, and other projects on the application of GMR sensors to detect a particular analyte. This dissertation explores GMR sensors yielding multiparametric data, and GMR sensors detecting biomolecules at picomolar levels. In addition, we investigate GMR-assisted transmission sensors with high sensitivity and silicon-enhanced GMR sensors. The projects detailed in the chapters that follow contribute to the field of GMR sensors in novel and innovative ways.

Chapter 2

Multiparametric guided-mode resonance biosensors

2.1 Summary

A guided-mode resonance (GMR) sensor with multiple resonant modes is used to measure the collection of biomolecules on the sensor surface and the index of refraction of the sensor environment (bulk). The number of sensor variables that can be monitored (biolayer index of refraction, biolayer thickness, and bulk, or background, index of refraction) is determined by the number of supported resonant modes that are sensitive to changes in these variable values. The sensor we use has a grating and homogeneous layer, both of which are made of silicon nitride (Si_3N_4), on a quartz substrate. In this work, we simulate the sensor reflection response as a biolayer grows on the sensor surface at thicknesses from 0 to 20 nm and biolayer indices of refraction from 1.334 to 1.43 RIU; simultaneously, we vary the bulk index of refraction from 1.334 to 1.43 RIU. In the specified span of sensor variable values, the resonance wavelength shifts for 2023 permutations of the biolayer index of refraction, biolayer thickness, and bulk index of refraction are calculated and accurately inverted. Inversion is the process of taking resonant wavelength shifts, for resonant modes of a sensor, as input, and finding a quantitative variation of sensor variables as output. Analysis of the spectral data is performed programmatically with MATLAB. Using experimentally measured resonant wavelength shifts, changes in the values of biolayer index of refraction, biolayer thickness, and bulk index of refraction are determined. In a model experiment, we deposit Concanavalin A (Con A) on our sensor and subsequently deposit yeast, which preferentially bonds to Con A. A unique contribution of our work is that biolayer refractive index and biolayer thickness are simultaneously determined.

2.2 Introduction

In industry, sensors/transducers have applications which include healthcare and medicine, air quality, food safety, and fuel storage. A problem in the aviation industry is the contamination of fuel with foreign organisms such as yeast [32]–[34]. The accumulation of bio-organisms, which feed on the carbon in fuels, reduces fuel stability, corrodes storage tanks, and degrades the functions of valves, pumps, and other mechanisms in a fuel system – all of these problems are termed fuel biofouling [19] [35]. Portable transducers that are inexpensive, collect data for long time intervals, and generate data quickly after a binding event, can be used to monitor the status of jet fuel stored in tankers.

When detecting chemicals or organisms, it can be important to quantify the thickness and index of refraction of an adhered layer of analyte on the transducer surface as well as the refractive index of the background/bulk media [17] [36]. Quantifying these three variables requires multiparametric transducer input: in the case of a GMR sensor, three or more resonant peaks that shift due to these sensor variables [17]. A GMR sensor produces resonant peaks that can be interrogated with white light. As the sensor variables change, the resonant peaks shift, and these shifts can be correlated to the magnitude the sensor variables have changed [17] [37].

There has been past work that determined sensor variable values using a sensor's sensitivity: the magnitudes of resonant wavelength shifts are monitored as one sensor variable is fixed and the other sensor variables are solved for [38]. This method usually requires that one biolayer variable is held constant as the other varies [39] [40]. The sensitivities can be expressed as

$$S(n_{bio}) = {\Delta\lambda}/{\Delta n_{bio}} \quad (2.1)$$

$$S(d_{bio}) = {\Delta\lambda}/{\Delta d_{bio}} \quad (2.2)$$

$$S(n_{bulk}) = {\Delta\lambda}/{\Delta n_{bulk}} \quad (2.3)$$

These expressions denote biolayer index of refraction sensitivity $\{S(n_{bio})\}$, biolayer thickness sensitivity $\{S(d_{bio})\}$, and bulk index of refraction sensitivity $\{S(n_{bulk})\}$, respectively. In the above expressions $\Delta\lambda$, Δn_{bio}, Δd_{bio}, and Δn_{bulk}, are the change in resonance wavelength, change in biolayer index of refraction, change in biolayer thickness, and change in bulk index of refraction, respectively. Using sensitivity to determine biolayer sensor values falls short because the biolayer thickness (biolayer index of refraction) sensitivity is dependent on the value of the biolayer index of refraction (biolayer thickness). For instance, a greater biolayer thickness yields a greater absolute value of biolayer index of refraction sensitivity. This is because the evanescent tail of a resonant mode sees a larger change for a thicker layer. The analogue of this concept applies to the magnitude of biolayer thickness sensitivity: a greater biolayer index of refraction yields a greater absolute value of biolayer thickness sensitivity. Restricting one biolayer variable to a constant value, during biolayer growth, to calculate the other biolayer variable is a method to recon with the interdependence of the biolayer variables' sensitivities; we avoid this restriction using our method of analysis. Our method expands on past work that used a GMR sensor with 2 resonant modes and simulation tools to create a lookup table [17]. In the work done by Magnusson et al., the lookup table is used to solve for biolayer index of refraction and bulk index of refraction while biolayer thickness is held constant [17].

There have been methods proposed to interpret transducer output and deconvolve the biolayer/adlayer thickness and biolayer/adlayer index of refraction [41]–[43]. These works include using a surface plasmon resonance sensor to conduct 2 experiments to get 2 data sets,

then interpreting the data to determine the dielectric constant and thickness of a dielectric layer [44]. Another related work discusses the theory of using a combination GMR-SPR (guided mode resonance-surface plasmon resonance) sensor with 3 resonant modes: among the 3 resonant modes, the biolayer sensitivities differ by orders of magnitude and the bulk sensitivities also differ – to a lesser extent [45]. Using the values of sensitivity, matrix methods are proposed to calculate the biolayer thickness, biolayer index of refraction, and bulk index of refraction [45]. In addition to a sensor being multiparametric, like those mentioned above, it is also of great importance that a sensor does not require the analyte to be tagged or altered for detection (label-free) [46].

A bio-selective layer can be applied to the sensor surface to capture the desired analyte and reject other substances in the environment [19] [17] [47] [48]. Thus, a GMR sensor can be tailored to detect an analyte of choice without the use of labels, as in label-free sensing. Multiparametric and label-free sensing is in high demand in industry, and it can be performed using a GMR sensor [17] [49].

Other label-free sensors include surface plasmon resonance sensors, integrated interferometers, MEMS-based sensors, nano-sensors (rods and particles), Bragg grating sensors, photonic crystal-based sensors, ring-resonator sensors, ellipsometry, and grating coupled sensors [17] [50] [51]. Sensor schemas that utilize labels include immunomagnetic separation, polymerase chain reaction, and standard immunoassay; these sensor types use luminescent, radioactive, absorptive, and fluorescent labels [17]. Sensors that utilize labels require the extra step of altering the analyte for detection. In contrast, the GMR sensor surface is altered to selectively capture and detect the analyte of interest.

Surface plasmon resonance (SPR) sensors, which are most like GMR sensors, utilize a resonance effect at the interface between a dielectric and metal [52] [53]. When a TM polarized electromagnetic wave reaches a dielectric and metal interface at a specific angle of incidence, the electromagnetic wave becomes evanescent at the interface while interacting with the free electrons in the metal [54]. This phenomenon produces an absorption minimum in the spectrum that has high angular and spectral sensitivity [55]. The linewidth of SPR sensors is large, and only a TM mode produces an SPR response. In contrast, GMR sensors have a smaller linewidth, preferred over a large one, and the resonance effect can be produced using both the TE and TM modes which allows monitoring the changes in a greater number of sensor variables with mixed polarization states.

The GMR sensor produces resonant modes by diffracting incident broadband light into leaky waveguide modes allowing standing waves to form in the sensor at specific wavelengths (frequencies) as eigenmodes [2]. The GMR properties that admit these selected wavelengths into the sensor (coupled in) also allow these wavelengths out of the sensor (coupled out). Because standing waves have allowed multiple photons to constructively interfere, the efficiency of the light coupled out of the sensor is high [2]. The light coupled out at high efficiency is referred to as being resonant. These resonant wavelength spectra are narrow and sensitive to changes on the surface of the GMR structure; for example, chemical reactions or the presence of a biomaterial [36] [48] [2] [56].

Magnusson and Wang proposed the use of the GMR effect for sensor applications due to the GMR filter's tunable properties based on the resonance structure parameters and refractive indices [2]. Tibuleac et al. and Wawro et al. introduced new GMR biosensor devices in addition to applications of the sensors integrated with optical fibers [36] [57]. Utilization of modal and

polarization differentiation for multiparametric biosensors is a pivotal attribute of this technology [17].

GMR sensors are highly sensitive to their resonance parameters which is innate in the fundamental resonance effect [17]. The resonant wavelength values of the GMR device are perturbed as the structure parameters change due to the attachment of a biomolecular layer on the device. A bio-selective layer on the GMR device can preferentially bind with a target analyte; this avoids additional data processing and foreign tags [17]. The GMR sensor has attributes including enriched data sets, label free sensing, and economic fabrication. These are qualities that will lead to the continued application of this sensor technology in several fields [58].

The sensor used in this work is required to have 3 or more resonant modes and it must be easily fabricated. To achieve the goal of 3 or more resonant modes, a sensor with a relatively thick homogeneous layer is developed. The thick homogeneous layer supports the resonant modes. Here we fabricate a 1-D grating with a two-part period. Also, an aspect ratio is chosen such that the pillars in the grating are easily formed with a low probability of collapsing.

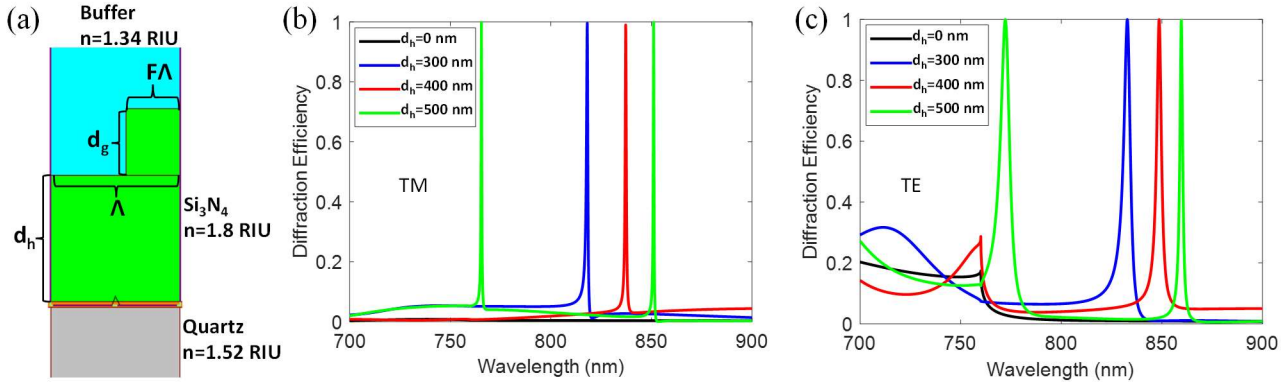

Figure 2-1 Multiparametric sensor. (a) The sensor used in this work consists of a silicon nitride (Si_3N_4) grating and homogeneous layer on a quartz substrate. The orange horizontal line at the substrate/homogeneous layer interface represents a light source directed upward. The grating parameters are as follows: fill factor (F) = 0.42, grating depth (d_g) = 260 nm, homogeneous layer depth (d_h) = 500 nm, and period (Λ) = 500 nm. (b) The RCWA simulated zero-order TM reflection spectrum from 700 to 900 nm for homogeneous layer thicknesses 0, 300, 400, and 500 nm. (c) The same for the TE spectrum. TE polarization has the electric field vector normal to the plane of incidence, whereas TM polarization has the magnetic field vector normal to the plane of incidence.

The sensor model shown in **Figure 2-1**(a) is simple and easily fabricated with a grating aspect ratio of 0.81. In **Figure 2-1**(b) and (c) the TM and TE spectra are shown for a simple grating (d_h = 0 nm) and for d_h values from 300 to 500 nm: these simulations use the rigorous coupled-wave analysis (RCWA) module in RSoft DiffractMOD software (Synopsys, Inc.) [59] [60]. The grating without a homogenous layer has no resonant peaks in the spectrum of interest. At a d_h value of 500 nm, 2 resonances occur in each polarization state for a total of 4 resonant peaks. The thicker homogeneous layer results in more resonant peaks that are used to detect changes in the multiple sensor variables. To this end, a homogeneous layer of 500 nm is chosen

for this work to allow for multiparametric data collection from the sensor (**Figure 2-1**(b) and (c) green line).

In this work we use simulation tools, with our multiparametric sensor, to generate an extensive library of biolayer thicknesses, biolayer indices of refraction, bulk indices of refraction, and the associated resonant wavelength shifts produced by our sensor. We use our library (also termed lookup table) and an inversion algorithm to take an input of measured shifts of 3 resonant wavelengths (measured in one spectrometer reading) and then output the shifts in the value of 3 sensor variables (biolayer thickness, biolayer index of refraction, and bulk index of refraction). This method of determining biolayer and bulk sensor value shifts is novel specifically because we simultaneously determine shifts in the values of 2 biolayer variables. To add to the usefulness of our method, we also determine shifts in value of 1 bulk variable. The creation of a lookup table through a quick automated process and the utilization of an inversion algorithm expands what can be done with multiparametric sensors/transducers.

2.3 Experiments and methods

2.3.1 Fabricated sensor specifications

The guided-mode resonance (GMR) sensor consists of a quartz substrate overlayed with silicon nitride (Si_3N_4) via plasma enhanced chemical vapor deposition (PECVD). The Si_3N_4 was deposited at a rate of 290 Angstrom/min. After Si_3N_4 is deposited on the substrate, it is patterned using laser interference lithography (LIL) and reactive ion etching (RIE) to achieve the fill factor and grating depth needed (**Figure 2-2**).

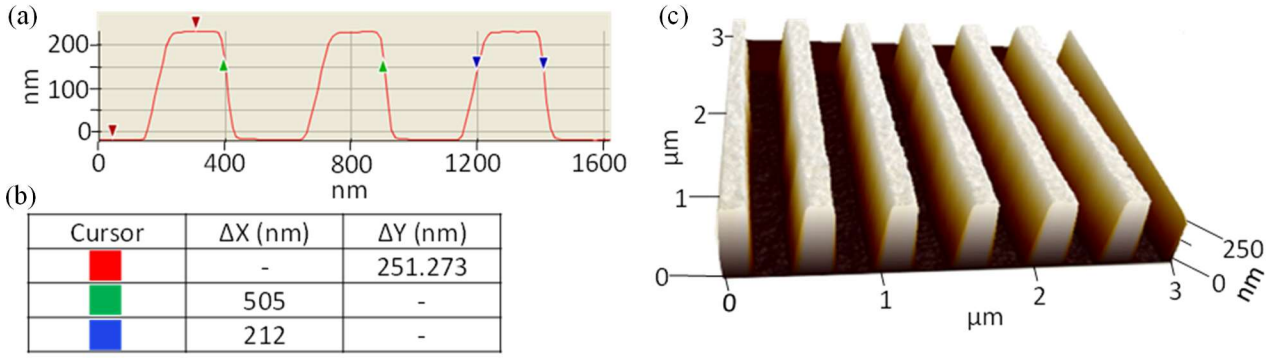

Figure 2-2 AFM data for the multiparametric sensor. (a) An atomic force microscope (AFM) generated profile of the sensor grating. The colored arrows indicate the positions used to measure grating depth (red), period (green), and fill factor (blue). (b) A table with horizontal (ΔX) and vertical (ΔY) measurements based upon the colored arrow locations in (a): red indicates the grating depth, green indicates the period, and blue indicates the grating width. The cursor locations indicate the grating depth (d_g=251 nm), period (Λ=505 nm), and fill factor (F=0.42). The fabricated parameters are close to the design parameters which are d_g = 260 nm, Λ = 500 nm, and F = 0.42. (c) An AFM generated 3D rendering of the sensor grating.

The sensor described above was used to quantify Concanavalin A (Con A) and Yarrowia yeasts that bind to the sensor surface. The sensor surface was functionalized with Con A because it attracts the glycoproteins found on the cell wall of the yeasts [19]. The reflection response of the sensor was measured with an Ocean Optics USB4000-VIS-NIR spectrum analyzer via an Ocean Optics bifurcated optical fiber. The layout of the sensor setup is illustrated in **Figure 4-6**.

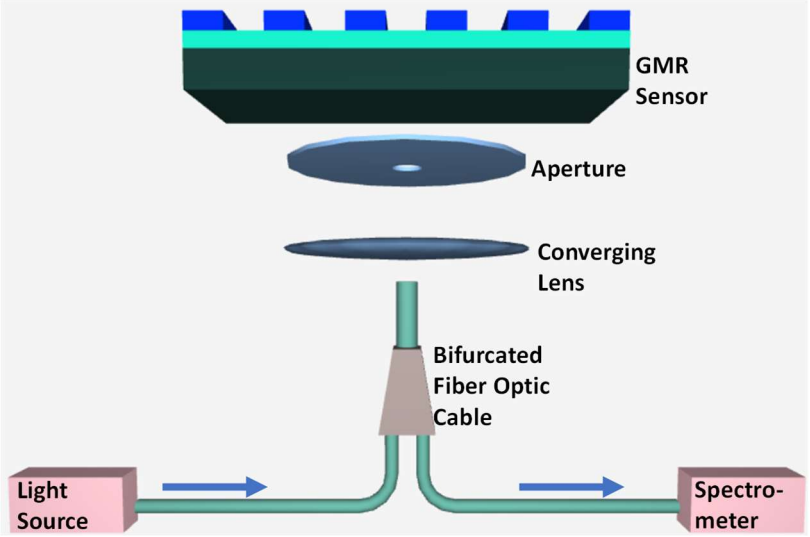

Figure 2-3 Schematic of the sensor layout. The broadband light from the source is sent through the fiber optic cable, the converging lens, and the aperture. The light then interacts with the GMR sensor and travels back through the optical elements to reach the spectrometer.

2.3.2 Yeast cell preparation

The yeast cells used were in a suspension media including 20% glycerol. The yeast cells were of the fungal genus Yarrowia in the Ascomycota phylum family. There are 4 to 6 chromosomes in the yeast cells, and the genome encodes 6448 genes [19]. The Yarrowia species of yeast characteristically form biofilms [61]. The yeast cells were reduced from a concentration of 8.25×10^7 to 8.25×10^5 cells/mL by diluting them in phosphate buffer saline (PBS).

2.3.3 Sensor surface functionalization

The methanol used in this work was from Sigma-Aldrich (St. Louis, MO, USA); Concanavalin A (Con A) and glutaraldehyde were from Santa Cruz Biotechnology, Inc. (Dallas, TX, USA); and (3-Aminopropyl)triethoxysilane (APTES) was from Acros Organics (Carlsbad, CA, USA).

The sensor surface was functionalized in accordance with the work carried out by Abdallah et al. [19]. The molecules used on the sensor surface were meant to promote specific binding to the desired analyte (yeast cells) and simultaneously reduce non-specific binding. The silane in the APTES solution was used to capture the protein Con A. Con A has a high affinity to bind to the polysaccharides that are readily found on the cell wall of yeasts—the analyte of choice [62].

First, the sensor was placed in 3% (3-Aminopropyl)triethoxysilane (APTES) and 97% methanol for 30 min to salinize the surface. The sensor was then gently agitated for 60 s in a 60:40 mixture of methanol and deionized (DI) water; it was then dried in a vacuum furnace for 30 min at a temperature of 95 °C and a pressure of 15 mm Hg. A mixture consisting of 0.7% glutaraldehyde (GA) and 99.3% DI water was prepared and the sensor was submerged in the mixture for 60 min. Subsequently, the sensor was agitated in DI water for 60 s. The sensor was then incubated in 1 mg/mL of Con A in PBS for 120 min; for part of this time, the reflection spectrum was measured, and the resonant wavelength shifts at the end of the period were recorded as the total shifts. Then, the sensor was placed in a DI water bath and gently agitated for 60 s. A dilution of yeast cells in PBS with a concentration of 8.25×10^5 cells/mL was used to soak the sensor surface for 120 min; the spectrum was measured for part of the incubation period. The wavelength shifts at the end of the recorded portion of this interval were recorded as the total shifts.

2.3.4 Inversion: translating resonant shifts to sensor variables

A lookup table of simulated resonance shifts, and corresponding sensor variable value changes was used to invert resonant shift values to changes in the biolayer and bulk environment of the sensor. The RCWA module in RSoft DiffractMOD software (Synopsys, Inc., Mountain View, USA) was used for all simulations in this work [60]. A valuable feature of RSoft is the

ability to set a value range of GMR structure parameters (like depth/thickness and index of refraction) and step sizes through the value range. For example, the grating depth range can be set from 50 nm to 250 nm and the step size can be chosen as 10 nm. This would result in producing 21 simulations that iterate through grating depth values from 50 nm to 250 nm (i.e., 50, 60, 70, … 250 nm) with all other GMR parameters held constant. Each simulation consists of reflectance over a wavelength spectrum, with the wavelength range and resolution selected by the user. The RSoft software can also perform iterative RCWA calculations over multiple sensor parameters based on ranges of values and step sizes through the ranges set by the user.

To produce the lookup table in this work, the sensor's structural parameters (period, fill factor, grating depth, and homogeneous layer depth) and indices of refraction of materials were held constant, and a biolayer was modeled on the sensor surface. The term, sensor variables, is used to refer to the values of the modeled biolayer and a value of the bulk environment. Iterative simulations were set to cycle through values of biolayer thickness, biolayer index of refraction, and the bulk index of refraction; each simulation generates the reflectance spectrum for a set of sensor variable values.

In our work, the iteration settings were as follows: the biolayer thickness range was 2 nm to 20 nm and the step size was 3 nm (i.e., 2, 5, 8, … 20 nm), the biolayer index of refraction range was 1.334 RIU to 1.430 RIU and the step size was 0.006 RIU (i.e., 1.334, 1.340, 1.346, … 1.430 RIU), and the bulk index of refraction range was 1.334 RIU to 1.430 and the step size was 0.006 RIU (i.e., 1.334, 1.340, 1.346, … 1.430 RIU). This resulted in 7 values of biolayer thickness, 17 values of biolayer index of refraction, and 17 values of bulk index of refraction. A simulation was performed for every permutation of the biolayer and bulk sensor variable values set by the user; this resulted in a total of 2023 reflectance spectra produced via RSoft simulation. We

developed a MATLAB program to quickly evaluate the peak wavelength values for each of the 4 resonant modes by finding the maximum reflectance value in a wavelength range corresponding to a given mode. For a single simulation, a set of 4 resonant wavelengths, biolayer thickness, biolayer index of refraction, and bulk index of refraction were grouped together and inserted into a digital file referred to as the lookup table; this was all performed within our MATLAB program. The lookup table consisted of all permutations of the sensor variables set by the user and the corresponding resonant wavelength values for the 4 resonant modes. Our use of the iterative ability of RSoft and the MATLAB code we developed were key to taking experimental resonance wavelength shifts as input and producing GMR biolayer thickness, biolayer index of refraction, and bulk index of refraction as output. For the results reported herein, out of the set of 4 available modes (see **Figure 2-1**), we used the 3 modes with the highest sensitivity.

The experimentally measured wavelength shifts were taken as input and compared to the wavelength shifts from the lookup table using the formula $S_{min} \approx \sqrt{\sum_i (\Delta\lambda_{Ti} - \Delta\lambda_{Ei})^2}$. Here, $\Delta\lambda_{Ti}$ is the change in resonant wavelength ($\Delta\lambda$) from the lookup table (T) for the resonant mode (i). $\Delta\lambda_{Ei}$ is the change in resonant wavelength ($\Delta\lambda$) from the experimental input (E) for the resonant mode (i). The set of resonant wavelength shifts from the lookup table for which S is minimized correlates to a set of sensor variables that were taken as the output.

Let us detail how S_{min} was calculated. We determined the difference between the lookup table resonance wavelength shift for resonant mode TM_0 and the experimental resonance wavelength shift for resonant mode TM_0; this value was then squared. This computation was also performed for the TM_1 and TE_1 modes. These 3 values (one for each mode used) were summed and then square rooted to get S. This calculation was performed for all 2023 lookup table entries.

Of the 2023 lookup table entries, the 10 with the lowest values of S were kept (S_1 to S_{10}) and all others were discarded. The 2nd lowest value of S (S_2) was used to gauge the significance of the 8 S values that were greater (S_3 to S_{10}). Any S_3 to S_{10} value that had a percent difference from S_2 that was greater than ~30% was discarded. Statistical analysis of our data led us to using ~30% as the best cutoff point. As stated above, each S value corresponded to an entry in the lookup table. The biolayer thicknesses, biolayer indices of refraction, and the bulk indices of refraction corresponding to the remaining values of S were averaged and taken as the output biolayer thickness, biolayer index of refraction, and bulk index of refraction. Finally, to verify, these 3 physical values are inserted into the RCWA simulation software, and they generated a set of $\Delta\lambda$(simulation) that was approximately equal to the set of $\Delta\lambda$(experimental); this fact supports our use of this method.

2.4 Results and discussion

2.4.1 Lookup table

In this work, a GMR sensor was designed via simulation with the goal of having three or more resonant modes (**Figure 2-1**b, c); this was carried out to monitor changes in the single bulk variable and dual biolayer variables during the detection of an analyte. The values of resonant shifts for three of the modes of the GMR sensor were simulated for a range of bulk and biolayer variable changes. The resonant modes chosen for simulation were TM_0, TM_1, and TE_1. These resonant modes were chosen because they had the highest sensitivity to changes of bulk and biolayer sensor variables. The sensitivities were determined by shifting one sensor variable at a time, by a marginal amount, while holding the other two sensor variables constant. To calculate the sensitivities, the sensor variable values were chosen to be near the median based on the value ranges specified in Section 2.4: bulk index of refraction (1.382 RIU), biolayer thickness (11 nm),

and biolayer index of refraction (1.388 RIU). For clarity, to determine the biolayer/adlayer index of refraction sensitivity, the value of bulk index of refraction was held constant at 1.382 RIU and the value of biolayer thickness was held constant at 11 nm, while the biolayer index of refraction was varied marginally; the ratio of resonance wavelength shift and biolayer index shift is the sensitivity. An analogous process was applied to determine the GMR sensor sensitivity to biolayer thickness shifts and bulk index of refraction shifts.

The bulk index of refraction sensitivity for each mode was calculated as: TM_1 (56 nm/RIU), TM_0 (21 nm/RIU), TE_1 (65 nm/RIU), and TE_0 (17 nm/RIU). The biolayer thickness sensitivity for each mode was calculated as: TM_1 (0.0057 nm/nm), TM_0 (0.0027 nm/nm), TE_1 (0.0027 nm/nm), and TE_0 (0.0013 nm/nm). The biolayer index of refraction sensitivity for each mode was calculated as: TM_1 (12 nm/RIU), TM_0 (5.8 nm/RIU), TE_1 (4 nm/RIU), and TE_0 (2.2 nm/RIU). All sensitivities were determined via simulation with rigorous coupled-wave analysis as referenced above. The bulk index sensitivities were approximately linear for the range considered in this study as supported by **Figure 2-4**.

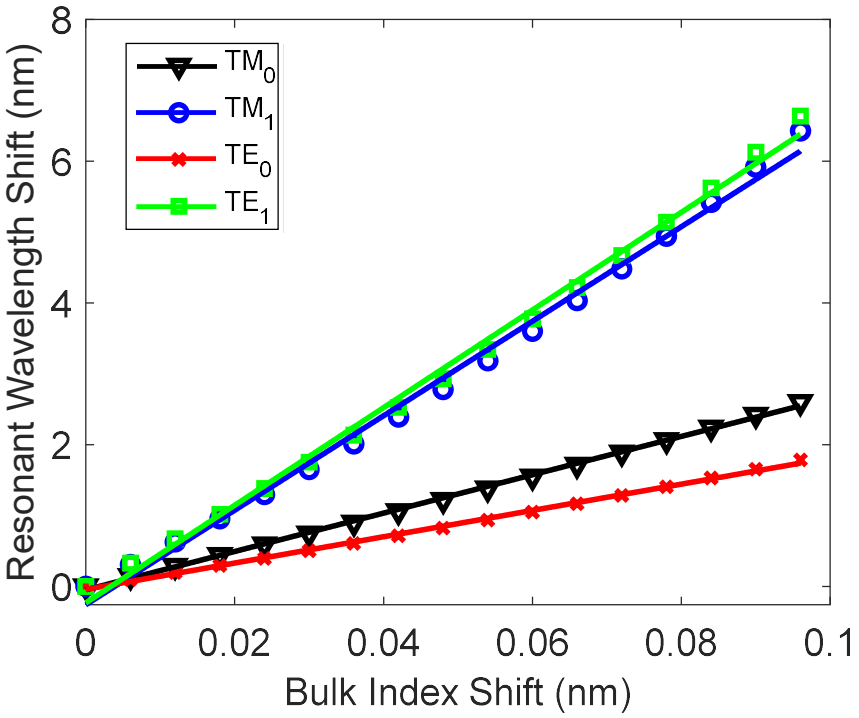

Figure 2-4 Bulk index shift vs. resonant wavelength shift. Simulated bulk index of refraction shifts and the resultant resonant wavelength shifts for the TM and TE resonant modes: the biolayer thickness for these simulations is 0 nm. Each resonant mode is plotted with its best fit line of corresponding color.

Recapitulating, the purpose of our work and the sensor proposed is to have three resonant modes to enable multiparametric data collection for use with a lookup table and inversion algorithm.

Figure 2-5 is a visual representation of a small portion of the lookup table that is generated via simulation. Each data point represents a combination of biolayer index of refraction, biolayer thickness, bulk index of refraction, and the resultant resonance wavelength shift. The greater the slope of a line taken across a plane in **Figure 2-5** , the more sensitive the resonant mode is to changes in the biolayer. In addition, the greater the difference in resonance wavelength shift between the planes, in a plot for a given mode, the more sensitive the mode is to a change in the

bulk index of refraction. While the TM_1 and the TE_1 modes of light have comparable sensitivities to the bulk index of refraction, the warped nature of the TM_1 planes is indicative of the greater sensitivity to changes in the biolayer for the TM_1 mode. The lookup table, which is visually represented in **Figure 2-5** , is used to invert from experimentally measured resonant wavelength shifts to changes in sensor variables.

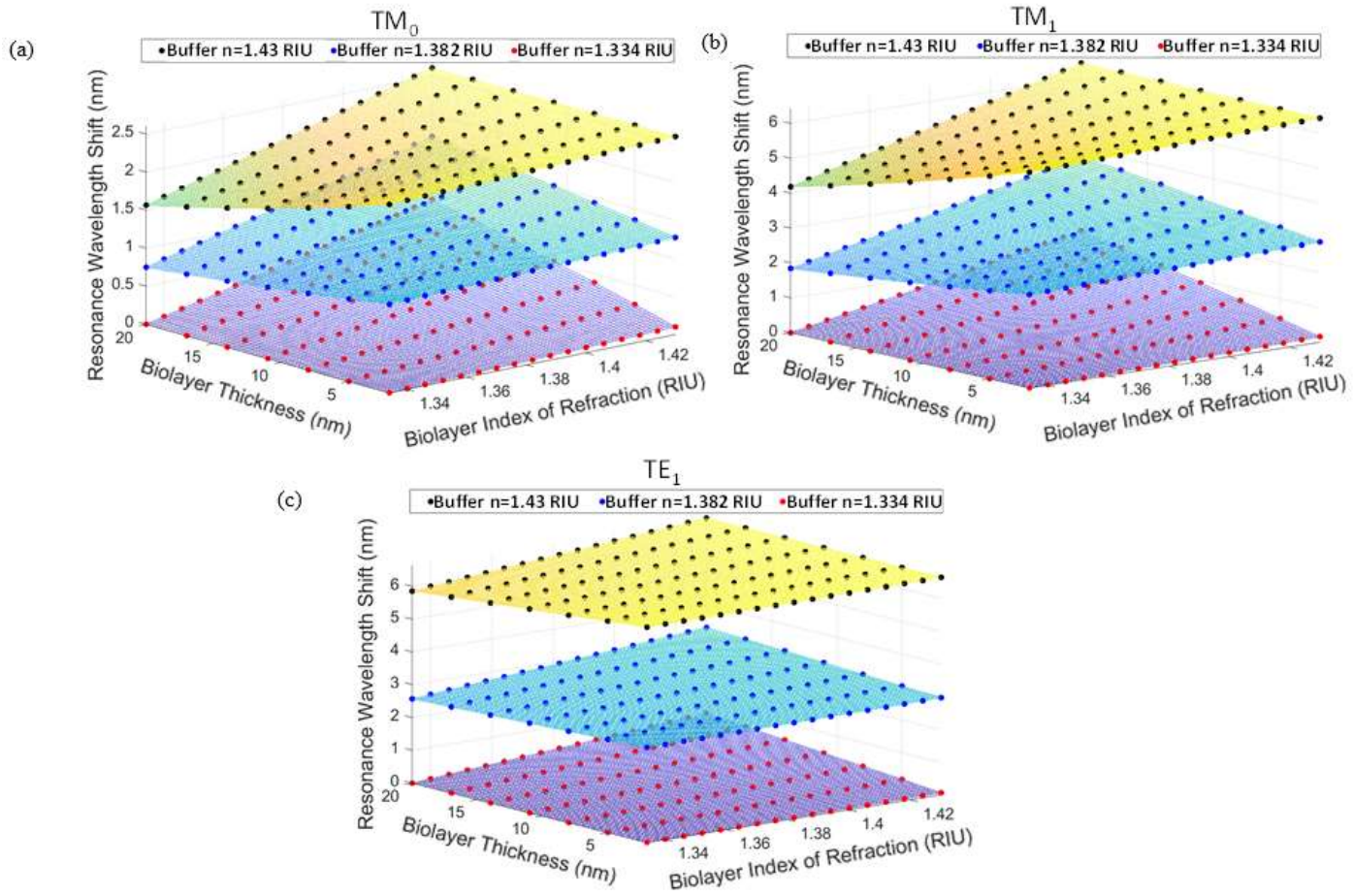

Figure 2-5 Visual representation of the lookup table. A plot of the simulated (a) TM_0 resonance wavelength shifts for a given biolayer index of refraction and biolayer thickness for the biosensor shown in Figure 2-1a; each sheet of simulation data represents a different value of bulk index of refraction (buffer) as indicated in the legend. This plot is also produced for the (b) TM_1 and (c) TE_1 modes of light.

The use of a lookup table of sets of resonance wavelengths with their accompanying sensor variable values is a novel aspect of our work. Specifically, the use of a lookup table to determine both biolayer thickness and the biolayer index of refraction in one spectral measurement is nuanced. Many past studies, focused on determining sensor biolayer variable values, are restricted to holding one biolayer variable constant as the other biolayer variable is solved for. Our method of analysis, using a lookup table, overcomes this issue. Additionally, we use our method to determine the bulk index of refraction. This enhances the use of sensors with multiparametric output. Equation 2.4 is the fully expanded equation used to determine the sensor variable values as applied in practice. Minimization of the differences between experimental and theoretical resonance shifts determines the sought sensor variables. Thus, we minimize:

$$S_{min} \approx \sqrt{(\Delta\lambda_{TTE_1} - \Delta\lambda_{ETE_1})^2 + (\Delta\lambda_{TTM_0} - \Delta\lambda_{ETM_0})^2 + (\Delta\lambda_{TTM_1} - \Delta\lambda_{ETM_1})^2} \quad (2.1)$$

The three resonant wavelength shifts are used to determine S_{min}, and S_{min} is used to determine the biolayer index, biolayer thickness, and bulk index. These four sets of values (S_{min} and the sensor variables) define the four-dimensional numerical space in which the inversion algorithm operates.

2.4.2 Simulated input wavelengths compared to the calculated output sensor variable values

The lookup table used in the inversion algorithm consists of 2023 simulations with three sensor variables, the values of which are specified in Section 2.4; each one of the simulations is used to generate a corresponding set of three resonant wavelength shifts. To test the accuracy of our method, a set of the three resonant wavelength shifts are used as input in the inversion algorithm to determine if the expected biolayer thickness, biolayer index of refraction, and bulk index of refraction are produced as the output. This test resulted in an accurate output for all 2023 permutations of biolayer and bulk value shifts. To further test the accuracy of the inversion

algorithm, sensor variable sets with changes in biolayer thickness and biolayer index that deviate from those used to create the lookup table are chosen, and via simulation the corresponding resonance wavelength shifts for the TM_0, TM_1, and TE_1 modes are determined. These sets of three resonance shifts are input into the inversion algorithm, and the output of the inversion algorithm is compared to the known shifts of sensor variable values (**Table 2-1**). In **Table 2-1**, Δn_{bio}, Δd_{bio}, and Δn_{bulk} refer to the change in biolayer/adlayer index of refraction, change in biolayer/adlayer thickness, and change in bulk/background index of refraction, respectively.

Table 2-1 Simulation Input and Algorithm Output.

Simulation Input			**Algorithm Output**		
Δn_{bio} (RIU)	Δd_{bio} (nm)	Δn_{bulk} (RIU)	Δn_{bio} (RIU)	Δd_{bio} (nm)	Δn_{bulk} (RIU)
0.010	2.0	0	0.009	2.0	0
0.058	11.0	0	0.062	11.0	0
0.086	15.5	0	0.087	15.5	0
0.086	20.0	0	0.090	19.0	0
0.058	2.0	0.048	0.057	2.0	0.048
0.077	11.0	0.048	0.075	12.5	0.048
0.010	15.5	0.048	0.012	17.0	0.048
0.010	20.0	0.048	0.009	18.5	0.048
0.086	2.0	0.096	0.087	2.0	0.096
0.038	11.0	0.096	0.034	11.0	0.096
0.010	15.5	0.096	0.009	15.5	0.096
0.010	20.0	0.096	0.006	19.0	0.096

The first three columns are the shifts in sensor variable values used in the RSoft RCWA simulations to generate resonant wavelength shifts. The resonant wavelength shifts are then used as input for the inversion algorithm. The last three columns are the algorithm output, namely, calculated shifts in sensor variable values. The change in bulk refractive index is calculated with very high accuracy because the values simulated exist in the lookup table and because a slight shift in bulk RIU results in significant resonant wavelength shifts. The calculated changes in biolayer refractive index and biolayer thickness have slight deviations from the input values. This is because the input values do not exist in the lookup table, so a direct match is not possible.

However, the output of the algorithm is very close to the expected sensor variable shifts as seen by comparing the left three columns with the corresponding columns on the right.

In **Table 2-1**, the largest biolayer thickness deviation (that is the difference between the expected value and the value produced by the inversion algorithm) is 1.5 nm, the largest biolayer index of refraction deviation is 0.004 RIU, and the largest bulk index of refraction deviation is approximately 0 RIU. These relatively small deviations, and the accuracy of the inversion algorithm when values from the lookup table are used as input (this is described in detail at the beginning of this section), provide a strong case for the usefulness and credibility of our inversion algorithm.

2.4.3 Measured resonance shifts and inversion for Con A incubation

The experimentally measured reflection response of the fabricated sensor is shown in **Figure 2-6**, where four resonant peaks, within the wavelength spectrum of interest, are produced. In addition, **Figure 2-6** shows that each peak position is distinguishable from other peaks, so a polarizer is not necessary to monitor the shifts in peak position. It is shown here that the wavelength shifts over time can be used to simultaneously monitor the growth of a biofilm on a sensor surface, as well as changes in the bulk index of refraction.

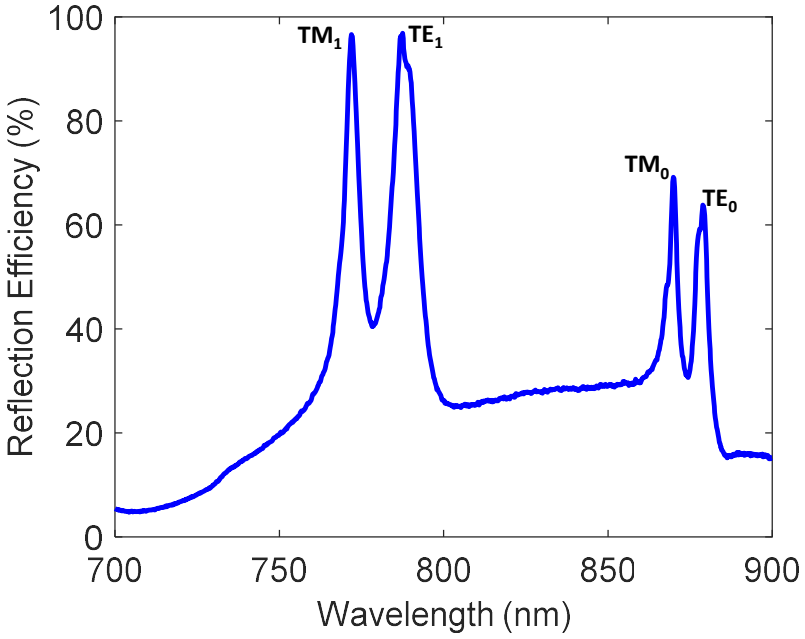

Figure 2-6 Multiparametric sensor reflection response. Measured unpolarized reflection spectrum of our bare GMR biosensor, with deionized (DI) water background, whose AFM is shown in **Figure 2-2**c. From lowest to highest wavelength, the peaks are due to TM_1, TE_1, TM_0, and TE_0 resonant modes as labeled on the figure.

During the functionalization process, to prepare the sensor to receive the analyte, glutaraldehyde (GA) is used to activate the amine groups from the APTES already deposited on the sensor. During incubation in the solution of Con A and PBS, an amide bond is formed between Con A and the amine groups on the sensor surface; this immobilizes Con A on the sensor. After incubation in Con A, the sensor is washed in DI water. The measured resonant shifts for Con A detection are 0.074, 0.18, and 0.058 nm for TM_0, TM_1, and TE_1, respectively. **Table 2-2** shows the output sensor variables determined using the inversion algorithm.

Table 2-2 Experimental Input and Algorithm Output for Con A Detection.

Experimental Input			Algorithm Output		
$\Delta\lambda$ TM_0 (nm)	$\Delta\lambda$ TM_1 (nm)	$\Delta\lambda$ TE_1 (nm)	Δn_{bio} (RIU)	Δd_{bio} (nm)	Δn_{bulk} (RIU)
0.074	0.18	0.058	0.047	7.2	0

Table 2-2 shows that the largest wavelength shift occurs for the TM_1 mode, with smaller shifts for the TM_0 and TE_1 modes. This is in line with the TM_1 mode being more sensitive to biolayer variable changes than the TM_0 and TE_1 modes. Additionally, the TM_0 mode is more sensitive to biolayer thickness changes than the TE_1 mode, and this accounts for TM_0 having a greater resonant wavelength shift than TE_1. The expectation is that Con A precipitates out of solution and adheres to the sensor surface due to the amide bond formed between Con A and the glutaraldehyde (GA) on the sensor surface. As Con A accumulates on the sensor surface during the incubation period, the shifts in the TM_1 and TM_0 modes are indicative of a change in the biolayer; because no process occurs that changes the bulk refractive index, the TE_1 mode has a relatively small shift.

During Con A incubation, the reflection spectrum of the GMR sensor is recorded every ~10 seconds. We have included the spectrum of the measurements at 0.17 min and 80 min in **Figure 2-7**.

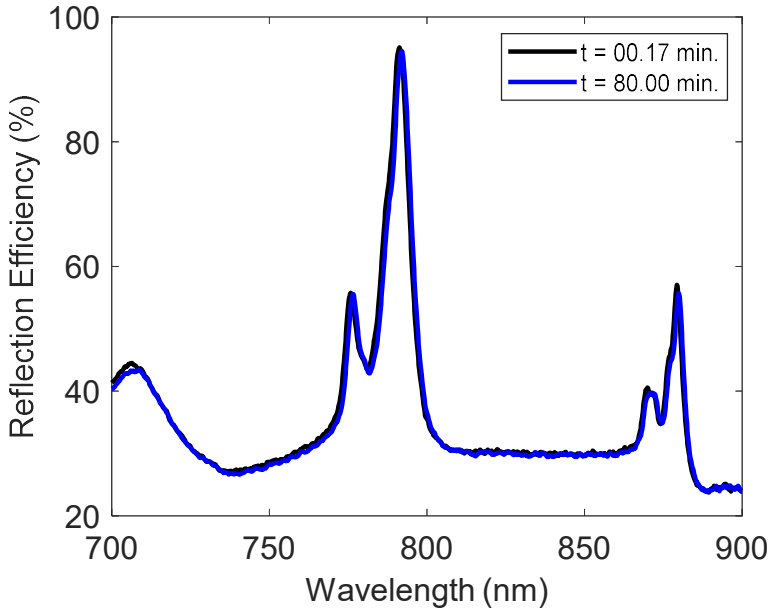

Figure 2-7 Multiparametric sensor in Con A response over time. Experimentally measured reflection spectrum during sensor incubation in a Con A and PBS solution (1 mg/mL). The spectra displayed are at beginning incubation time 0.17 min and at final incubation time 80.00 min.

Figure 2-8 shows the increase in the resonant shifts for the three modes of interest over time: during incubation in the Con A and PBS solution. This increase in resonant wavelength shift over time is due to the gradual accumulation of Con A on the surface of the GMR sensor. The spot of the sensor being monitored was altered at the 80-min mark. Thus, monitoring the development of a biolayer in a single spot on the sensor was stopped and data collection ceased after 80 min. Using the measured shifts of the resonant modes in **Figure 2-8**, the sensor variables are calculated. The algorithm output shows the progressive accumulation of Con A on the sensor surface (**Figure 2-9**).

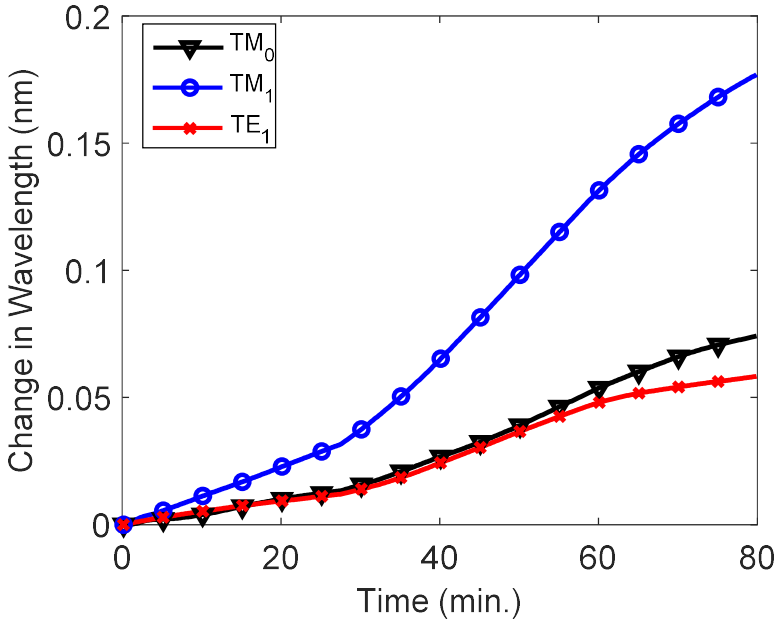

Figure 2-8 Resonance shift during Con A incubation. Experimentally measured resonance wavelength shifts during sensor incubation in a Con A and PBS solution (1 mg/mL). The TM_0, TM_1, and TE_1 modes are labeled in the legend as black, blue, and red, respectively.

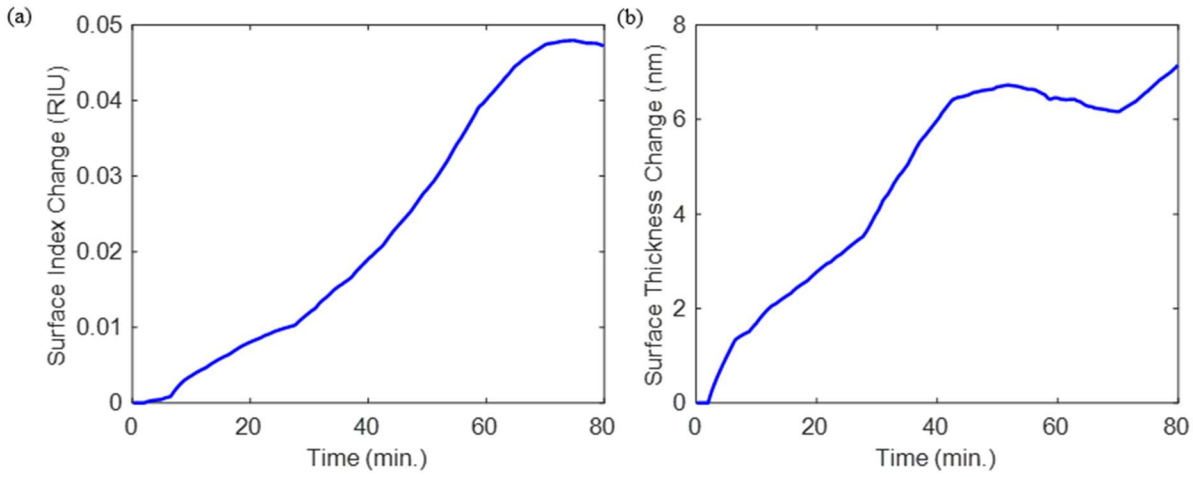

Figure 2-9 Biolayer variable shift vs. time due to Con A. Changes in the (a) biolayer index of refraction and (b) biolayer thickness during the incubation of the sensor in Con A. During this process, the change in the bulk refractive index (Δn_{bulk}) is calculated to be 0 RIU.

The biolayer index of refraction increases gradually until the ~70-min mark. After ~70 min the biolayer index of refraction stabilizes, and the shift is within the 0.006 RIU resolution of the lookup table. The biolayer thickness increases until the ~50-min mark. Thereafter, the biolayer thickness stabilizes, and the shift is within the 3 nm resolution of the lookup table.

2.4.4 Measured resonance shifts and inversion for yeast incubation

In our previous work with yeast cell detection, we calculated the limit of detection (LOD) to indicate the capability of the sensor used in that work [19]. Scaling the data collected in that work, by comparing the bulk sensitivity of the sensor in this work to the bulk sensitivity of the sensor used by Abdallah et al. (107 nm/RIU), we produce the graph of Log_{10}[Concentration] (or Log_{10}[C]) vs. resonant wavelength shift in **Figure 2-10**. The unit of concentration is cells/mL.

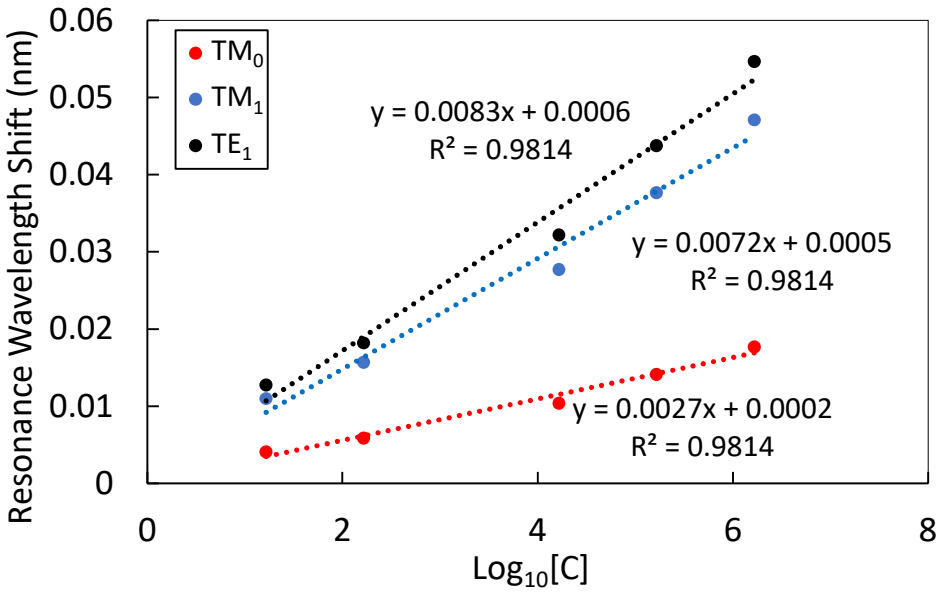

Figure 2-10 Yeast concentration vs. resonance shift. Scaled GMR sensor response from a series dilution of yeast cells in suspension with PBS. This data is based on our past work published in Abdallah et al. [19].

The yeast cell detection for a concentration range of 1.2–6.2 Log_{10}[C] has sensitivities of 0.0027 nm/ Log_{10}[C] for the TM_0 mode, 0.0072 nm/Log_{10}[C] for the TM_1 mode, and 0.0084 nm/ Log_{10}[C] for the TE_1 mode. The formula used for limit of detection is LOD = (3.3σ)/S: S is the slope of the response curve, and σ (0.005) is the standard deviation [19] [63]. The LOD values for yeast cells in PBS are 6.09 Log_{10}[C] (TM_0), 2.28 Log_{10}[C] (TM_1), and 1.97 Log_{10}[C] (TE_1).

During incubation in the mixture containing yeast in PBS, with a concentration of 8.25×10^5 cells/mL, the polysaccharides on the cell wall of the yeast cells preferentially bind to Con A. **Table 2-3** lists the measured resonant shifts for yeast detection for the TM_0, TM_1, and TE_1 modes. The inversion algorithm determines the output sensor variable value changes, quantified in **Table 2-3**.

Table 2-3 Experimental Input and Algorithm Output for Yeast.

Experimental Input			**Algorithm Output**		
$\Delta\lambda$ TM_0 (nm)	$\Delta\lambda$ TM_1 (nm)	$\Delta\lambda$ TE_1 (nm)	Δn_{bio} (RIU)	Δd_{bio} (nm)	Δn_{bio} (RIU)
0.051	0.061	0.016	0.02	6.7	0

The resonant wavelength shifts are smaller than those produced by Con A, with changes in sensor variables correspondingly smaller. This is in line with data collected by Abdallah et al. [4]. The resonant mode with the greatest sensitivity to changes in the biolayer is the TM_1 mode, and the mode with the least biolayer sensitivity is the TE_1 mode, as illustrated by the data in **Table 2-3**.

While the sensor is incubating in the yeast and PBS mixture, the resonance shifts are measured for the time interval from ~20 min to ~80 min, in ~10 s increments, and the changes in the biofilm and bulk are quantified. We have included the spectrum of the measurements at 20 min and 80 min in **Figure 2-11**.

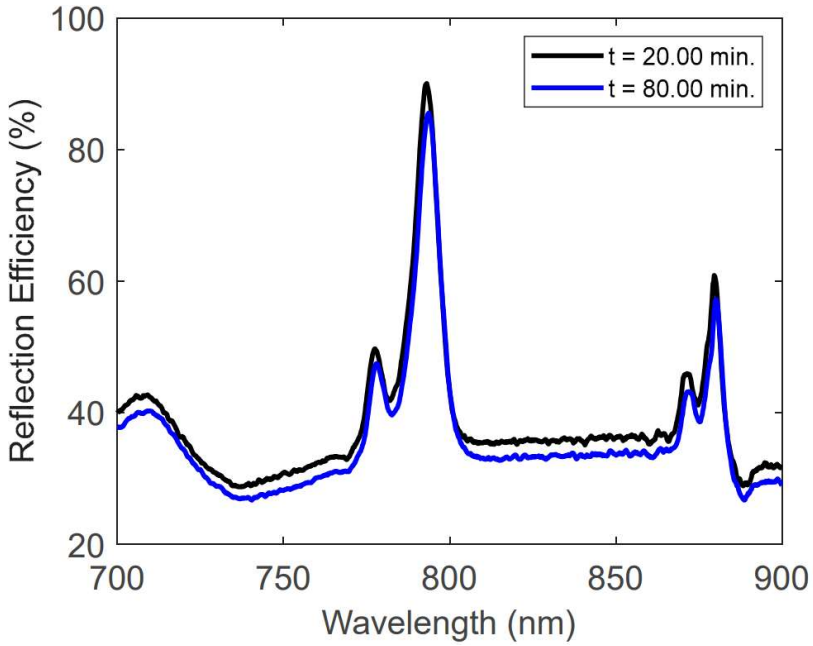

Figure 2-11 Multiparametric sensor in yeast response over time. Experimentally measured reflection spectrum during sensor incubation in a yeast and PBS solution (8.25×10^5 cells/mL). The spectra displayed are at incubation times 20.00 min and at 80.00 min.

Figure 2-12 displays the measured resonance peak shifts, with **Figure 2-13** showing the computed biolayer parameters.

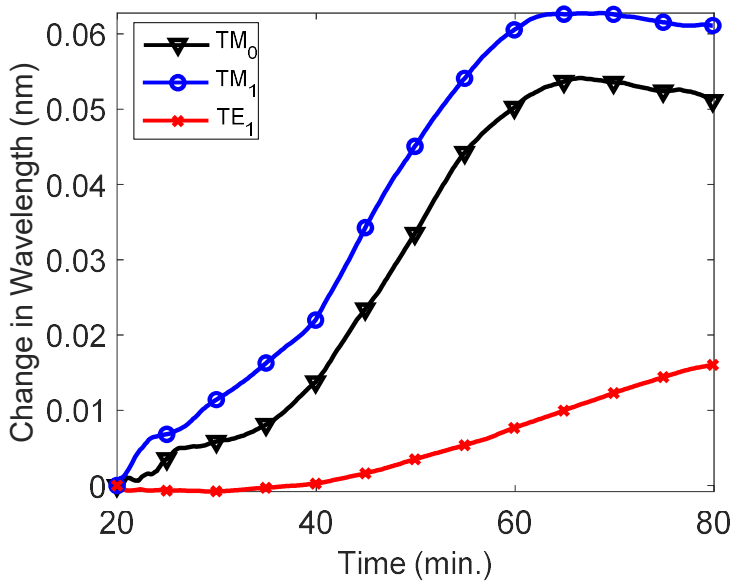

Figure 2-12 Resonance shift during yeast incubation. Resonance wavelength shifts while the sensor is incubated in a yeast and PBS solution (8.25×10^5 cells/mL). The TM_0, TM_1, and TE_1 modes are labeled in the legend as black, blue, and red, respectively.

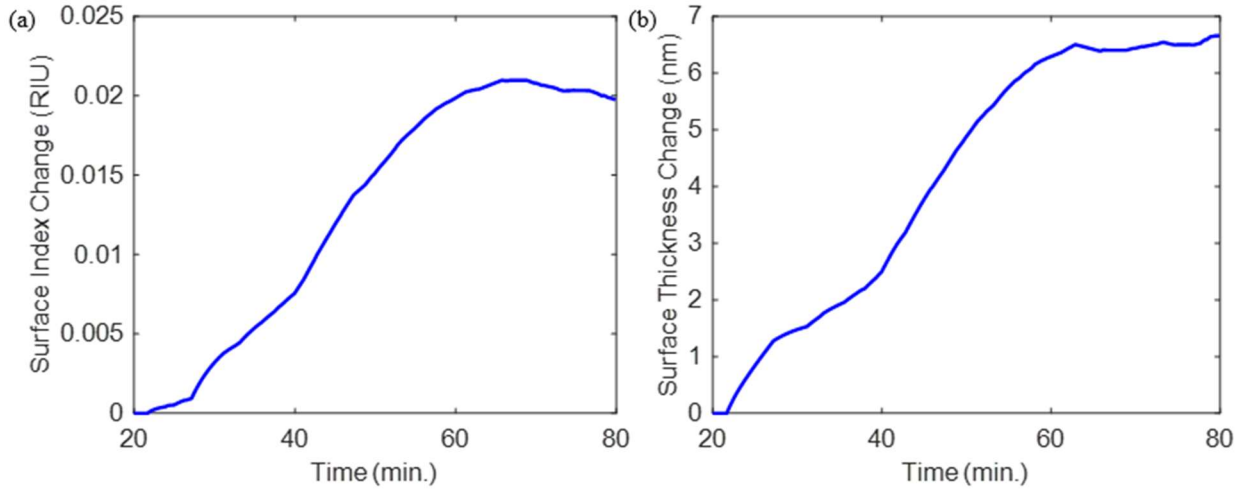

Figure 2-13 Biolayer variable shift vs. time due to yeast. Changes in the (**a**) biolayer refractive index and (**b**) biolayer thickness during the incubation of the sensor in yeast. During this process, the change in the bulk refractive index (Δn_{bulk}) is calculated to be 0 RIU.

2.5 Conclusions

Shifts in the wavelength of three resonant modes produced by a GMR sensor are used to simultaneously quantify the change in biolayer thickness, biolayer index of refraction, and bulk index of refraction. Extracting shifts in value for these three sensor variables using one spectral measurement is an improvement in the field of biosensing. In past work, GMR sensors have been used to monitor the bulk index of refraction and only one biolayer variable at a time.

The sensor used in this work is functionalized, with the protein Con A, for detection of Yarrowia yeast cells. During analyte accumulation, a set of three measured resonant wavelength shifts are used as inputs in an algorithm using a lookup table, and the outputs are three sensor variable value shifts: bulk index of refraction, biolayer thickness, and biolayer index of refraction. A label-free process that uses a single spectral measurement to determine changes in biolayer and bulk sensor variables is novel in practice. The multiparametric sensor, demonstrated via experiment and simulation in this work, is used to quickly obtain detailed information about the sensor environment and the accumulation of a desired analyte over time. The key to our study is the use of a lookup table and an inversion algorithm to simultaneously monitor three sensor variables (two biolayer and one bulk) as biomolecules are captured on a sensor surface; this is a feat that has not been accomplished in past research – based on our review of the literature.

The simulation of the 2023 reflection spectra, each with a different variable value set, is an automated process using rigorous numerical models. This process can be applied to other sensors of interest and the number of variable value sets can be chosen freely, exceeding the modest set count applied here. Implementing our inversion method with sensors that have a high sensitivity is expected to lead to a more accurate inversion; this would be important future work.

Chapter 3

Best fit line inversion algorithm

The purpose of the best fit line inversion algorithm, discussed below, is to take resonant wavelength shifts as input and yield the output of biolayer index of refraction shift, biolayer thickness shift, and bulk index of refraction shift. The best fit line inversion algorithm is robust and can be applied to a wide range of sensors. The process uses software to simulate the resonant wavelength response to shifts in sensor variables: the data from these simulations is stored and utilized as a lookup table. An entry in the lookup table is a set of sensor variables and the corresponding set of resonant wavelength shifts; 2023 entries make up the lookup table used in this work. A lookup table and the coding functions in a best fit line algorithm are the key components in determining the sensor variable value shifts given resonant wavelength shifts. Here, we test the algorithm by applying it to a known model, inputting chosen changes in biolayer index of refraction, biolayer thickness, and bulk index of refraction; and checking if the algorithm can determine these changes and with what accuracy.

The sensor used in this work consists of a silicon nitride (Si_3N_4) grating and homogeneous layer on a quartz substrate. The grating parameters are as follows: fill factor (F) = 0.42, grating depth (d_g) = 260 nm, homogeneous layer depth (d_h) = 500 nm, and period (Λ) = 500 nm. The reflection spectrum is analyzed to determine the resonant wavelength shifts.

The resonance wavelength shifts for TM_1, TM_0, and TE_1 are input into the best fit inversion algorithm: they are inputs in a MATLAB function. The MATLAB function loads the lookup table corresponding to the sensor being used. First, the shifts of the resonant modes are used to determine the change in bulk index of refraction.

The bulk index of refraction is determined by collecting 30 resonance shifts from the lookup table for each of the 3 resonant modes of interest. The resonant shifts are selected by finding the smallest absolute value difference between lookup table resonant shifts and the input resonant shifts (Equation 3.1).

$$s_i(min) = |\Delta\lambda_{Ti} - \Delta\lambda_{Ii}| \tag{3.1}$$

$\Delta\lambda_{Ti}$ is the change in resonant wavelength ($\Delta\lambda$) from the lookup table (T) for the resonant mode (i). $\Delta\lambda_{Ii}$ is the change in resonant wavelength ($\Delta\lambda$) from the input (I) for the resonant mode (i). In s_i(min), the subscript (i) is the resonant mode. The lookup table resonant wavelength shift for which s_i is minimized $\{s_i(\text{min})\}$ correlates to a set of sensor variables that are used to determine the shift in bulk index of refraction. This is done by taking a collection of 30 s_i(min) values for a single mode and plotting the shifts of biolayer index of refraction, biolayer thickness, and bulk index of refraction on the x, y, and z axes, respectively: this is done for the TE_1, TM_0, and TM_1 modes. A best fit surface, based on a cubic approximation, is produced for the 3 resonant modes. The value of bulk index of refraction shift where the greatest occurrence of points at which the surfaces intersect is taken as the output bulk index of refraction shift.

Once the output bulk index of refraction shift is determined, all lookup table values with bulk index of refraction shifts that differ – by more than the step size in the iterative simulations – are discarded. The input resonance wavelength shifts for the 3 resonant modes are now used to determine which lookup table entries have the smallest absolute value difference from the input resonant shift (Equation 3.1). For example, the absolute value of the differences between the input TE_1 shift ($\Delta\lambda_{ITE1}$) and the TE_1 shift from all remaining entries of the lookup table ($\Delta\lambda_{TTE1}$) are determined. A collection of 4 s_i(min) values from Equation 3.1 are used to generate a best fit line on a graph of biolayer index of refraction and biolayer thickness on the x and y axis,

respectively. This process is also used to get best fit lines for the TM_0 and TM_1 modes for a total of 3 best fit lines. The best fit lines for the 3 modes are plotted, and the biolayer index of refraction and biolayer thickness where the 3 lines intersect, or come the closest to intersecting, is taken as the output.

3.1 Inversion results

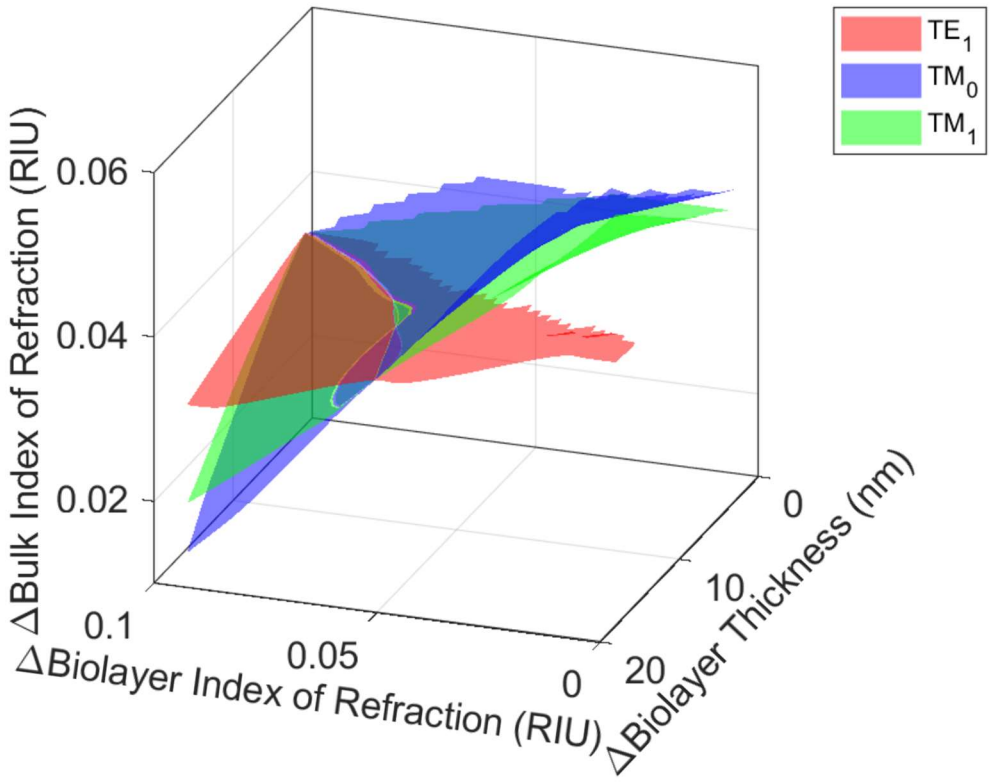

Figure 3-1 Planes of inversion values for resonant modes. A plot of the bulk and surface variable value planes produced by collecting the 30 variable sets from the lookup table that have a resonance shift closest to the input TE_1 mode resonance shift (red). The same is done for the TM_0 (blue), and TM_1 (green) modes.

We will now traverse an example beginning with a set of resonance wavelength shifts as input into the best fit line algorithm (resonant wavelength shifts are $\Delta\lambda_{TTE1}$=2.255 nm, $\Delta\lambda_{TTM0}$=1.074 nm, and $\Delta\lambda_{TTM1}$=2.344 nm); the sensor variable value shifts for the bulk and surface that correspond to these resonance shifts will be stated later in this discussion. Using the MATLAB utility for modeling the path between a collection of coordinates, a cubic plane is produced to approximate the best fit plane given the 30 variable sets (gathered using Equation 3.1). A separate plane is created for the 3 resonant modes used in the algorithm: TM_0, TM_1, and TE_1. In **Figure 3-1** the planes intersect at a bulk index of refraction shift of 0.066 RIU. The known bulk index of refraction shift is 0.066 RIU. Therefore, the determination of bulk index of refraction shift is accurate.

Figure 3-1 shows the best fit planes for the TE_1, TM_0, and TM_1 modes. The purpose of representing the collection of lookup table values in this way is to interpolate the bulk and surface variable values that are not simulated in the lookup table but are within the range of lookup table variable values. The results of the interpolated planes are used to output a value of bulk index of refraction shift for a set of input resonance wavelength shifts.

In **Figure 3-1**, the plane with the least change in the z-axis (bulk index of refraction) is the TE_1 plane. This characteristic of the TE_1 plane is indicative of the high sensitivity to bulk index of refraction for the TE_1 mode: TE_1 (65 nm/RIU), TM_1 (56 nm/RIU), and TM_0 (21 nm/RIU). Lookup table entries for which the TE_1 mode resonant wavelength shift ($\Delta\lambda_{TTE1}$) differs the least from the input ($\Delta\lambda_{ITE1}$) will have a low standard deviation of bulk index of refraction shifts, but they may have a wide deviation in the biolayer variable values. This is because a change in the bulk index of refraction of the sensor significantly shifts the resonance wavelength of the TE_1 mode. Due to the low sensitivity to biolayer variables for the TE_1 mode, changes in biolayer

values have a much smaller effect on the resonance wavelength shift of the TE_1 mode. This characteristic of the TE_1 plane (**Figure 3-1**) is common irrespective of what input resonances are used.

In **Figure 3-1**, the TM_0 plane has the greatest range with respect to the z-axis (bulk index of refraction) because the TM_0 mode has a low sensitivity to bulk index of refraction. This produces overlap in TM_0 resonance wavelength shift ($\Delta\lambda_{TTM0}$) among higher shifts of bulk index of refraction with low shifts of biolayer variables and lower shifts of bulk index of refraction with high shifts of biolayer variables. For example, variable shifts (biolayer index) Δn_{bio}=0.072 RIU, (biolayer thickness) Δd_{bio}=14 nm, and (bulk index) Δn_{bulk}=0.006 RIU produce a $\Delta\lambda_{TTM0}$=0.589 nm; and Δn_{bio}=0.054 RIU, Δd_{bio}=8 nm, and Δn_{bulk}=0.018 RIU produce a $\Delta\lambda_{TTM0}$=0.590 nm. The sensor variable sets listed differ significantly, although the TM_0 resonance shifts differ by only 0.001 nm. This characteristic of the TM_0 plane (**Figure 3-1**) is common irrespective of what input resonances are used.

In **Figure 3-1**, the TM_1 plane has a relatively large change in the z-axis (bulk index of refraction shift) because although the TM_1 mode has a high sensitivity to bulk index of refraction, the TM_1 mode has a very high sensitivity to biolayer variables. The biolayer thickness sensitivity for each mode is TE_1 (0.0027 nm/nm), TM_1 (0.0057 nm/nm), and TM_0 (0.0027 nm/nm) and the biolayer index of refraction sensitivity for each mode is TE_1 (4 nm/RIU), TM_1 (12 nm/RIU), TM_0 (5.8 nm/RIU). This results in an overlap in resonance wavelength shifts for TM_1 among higher shifts of bulk index of refraction with low shifts of biolayer variables and lower shifts of bulk index of refraction with high shifts of biolayer variables – analogous to the TM_0 mode. This characteristic of the TM_1 plane (**Figure 3-1**) is common irrespective of what input resonances are used.

After the shift of bulk index of refraction is determined, the algorithm then determines the shift of biolayer thickness and the shift of biolayer index of refraction. The 4 smallest absolute value differences between an input resonance shift and the remaining lookup table values are used to generate a best fit line; this process is performed for the TE_1, TM_0, and the TM_1 modes. The purpose of this is to find a single point where the 3 lines intersect or come the closest to intersecting (**Figure 3-2**).

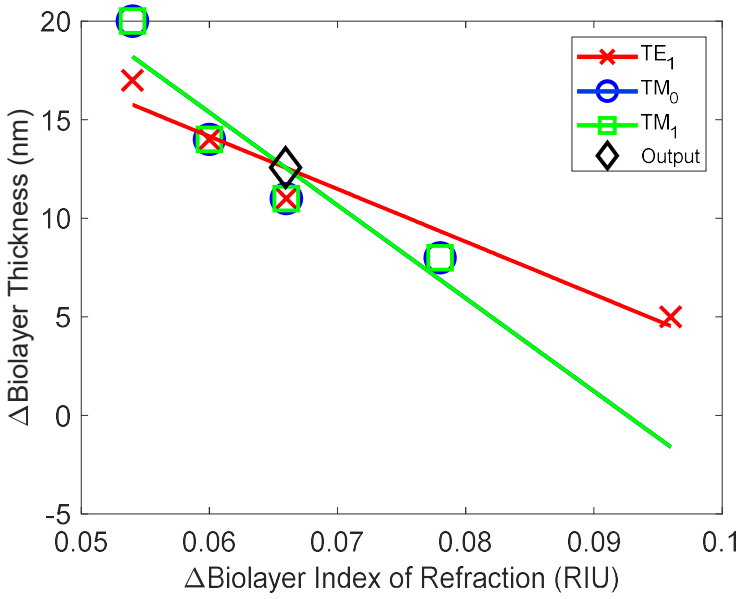

Figure 3-2 Inversion biolayer shift values. A plot of the biolayer variable shifts for the TE_1 (red X) that have the smallest absolute value difference in resonance shift from the input resonance shift. The same is done for the TM_0 (blue circle), and TM_1 (green square) modes. Also included are the best fit lines for the biolayer variable shifts for the TE_1 (red), TM_0 (blue), and TM_1 (green) modes – the TM_0 and TM_1 lines are colinear.

In **Figure 3-2** there are 4 sets of biolayer value shifts plotted for each mode of interest. The 3 best fit lines are evaluated to determine at what point (biolayer value set) they intersect or

come the closest to intersecting. Using the described algorithm, the output biolayer thickness shift and biolayer index of refraction shift are Δd_{bio}=12.57 nm and Δn_{bio}=0.0659 RIU, respectively; the actual simulated input biolayer variable shifts are Δd_{bio}=11 nm and Δn_{bio}=0.0660 RIU. The difference in shifts of biolayer thickness is 1.57 nm and for biolayer index of refraction it is 0.0001 RIU. Each of these differences are smaller than the biolayer thickness and biolayer index of refraction step sizes of the iterative simulations which are 3 nm and 0.006 RIU, respectively.

3.2 Simulated input wavelength shifts and best fit line algorithm output

The lookup table used in the best fit line inversion algorithm consists of 2023 simulations with three sensor variables. Included below is a collection of sensor variables used in the RSoft DiffractMOD software (Synopsys, Inc., Mountain View, USA) RCWA simulations to get resonant shifts for the TE_1, TM_0, and TM_1 modes [60]. The resonant shift sets are input into the best fit inversion algorithm and the output is a corresponding set of sensor variables. The table below (**Table 3-1**) compares known sensor variable values (simulation input) to algorithmically determined sensor variable values (algorithm output): a collection of the most accurate values was chosen for **Table 3-1**. The simulation input in **Table 3-1** are sensor variables that exist in the lookup table used for inversion.

Table 3-1 Lookup Table Simulation Input and Best Fit Algorithm Output.

Simulation Input			Algorithm Output		
Δnbio (RIU)	Δdbio (nm)	Δnbulk (RIU)	Δnbio (RIU)	Δdbio (nm)	Δnbulk (RIU)
0.006	2.0	0	0.006	2.2	0
0.084	14.0	0	0.084	14.0	0
0.072	17.0	0	0.074	16.7	0
0.054	20.0	0	0.054	19.2	0
0.012	2.0	0.048	0.012	2.0	0.048
0.090	14.0	0.048	0.087	15.5	0.048
0.066	17.0	0.048	0.066	15.9	0.048
0.090	20.0	0.048	0.090	18.5	0.048
0.048	2.0	0.096	0.048	2.0	0.096
0.006	14.0	0.096	0.006	13.9	0.096
0.042	17.0	0.096	0.042	17.6	0.096
0.030	20.0	0.096	0.029	19.5	0.096

The largest deviation between simulation input and best fit algorithm output for biolayer index of refraction shift is 0.003 RIU, for biolayer thickness shift it is 1.5 nm, and for bulk index of refraction shift it is approximately 0 RIU. While these deviations are within acceptable ranges, this is the inversion output for resonant shift sets directly from the lookup table. The expectation is that the best fit line algorithm would perform with near perfect accuracy for resonant shift sets directly from the lookup table. A factor that contributes to low accuracy output from the best fit line algorithm is biolayer variable sets used for the best fit line (**Figure 3-2**) with a high spread of biolayer thicknesses and/or biolayer indices of refraction. This translates into the collection of points for a single mode (the points used to produce the best fit line) having a spread of biolayer thicknesses greater than 12 nm and a spread of biolayer indices of refraction greater than 0.048 RIU: determined by statistical analysis of the output. Another factor that contributes to low accuracy is the need for all three lines (TE_1, TM_0, and TM_1 best fit lines) to intersect at the same point to have a definitive output.

Table 3-2 Non-Lookup Table Simulation Input and Best Fit Algorithm Output

Simulation Input			**Algorithm Output**		
Δn_{bio} (RIU)	Δd_{bio} (nm)	Δn_{bulk} (RIU)	Δn_{bio} (RIU)	Δd_{bio} (nm)	Δn_{bulk} (RIU)
0.0096	2.0	0.000	0.0097	2.9	0
0.077	11.0	0.000	0.075	11.3	0
0.086	15.5	0.000	0.089	15.2	0
0.019	20.0	0.000	0.018	18.1	0
0.058	2.0	0.048	0.058	2.9	0.048
0.019	11.0	0.048	0.020	12.6	0.048
0.086	15.5	0.048	0.087	15.5	0.048
0.010	20.0	0.048	0.012	19.8	0.048
0.067	2.0	0.096	0.066	2.0	0.096
0.077	11.0	0.096	0.079	13.6	0.096
0.058	15.5	0.096	0.058	16.4	0.096
0.019	20.0	0.096	0.024	20.0	0.096

Table 3-2 consists of a set of simulation input values and algorithm output values. While the biolayer and bulk variable value inputs are in the range of the values simulated in the lookup table, they are not actual values that are simulated in the lookup table thus interpolation is performed to determine an output value. A collection of the most accurate values was chosen for **Table 3-2**. The largest deviation between simulation input and best fit algorithm output for biolayer index of refraction shift is 0.005 RIU, for biolayer thickness shift is 2.6 nm, and for bulk index of refraction shift is approximately 0 RIU. In comparison to the biolayer and bulk variable input values from the lookup table (**Table 3-1**), the values that are not in the lookup table (**Table 3-2**) result in a lower percent of accurate inversion results. This is due to the lack of accurate biolayer value sets in the points used to generate best fit lines for the input of **Table 3-2**. The values from the lookup table (**Table 3-1**) have a smaller range of biolayer values for the set of points used to produce the best fit lines: this results in higher accuracy inversion output.

3.3 Trends in inversion accuracy

Statistically, the sets of biolayer variable shifts with greater biolayer thickness shifts (11 nm to 20 nm) are in general more accurate than biolayer variable sets with smaller biolayer thickness shifts. A large thickness shift causes larger resonance shifts as biolayer index of refraction changes: this is because the evanescent tail of a resonant mode sees a larger change for a thicker biolayer. At greater biolayer thickness shifts, the significant difference in resonance shifts among adjacent biolayer index of refraction shifts (e.g. 0, 0.006, 0.012 RIU) translates into less erroneous biolayer value sets being used in the generation of best fit lines. Also, the biolayer shifts with biolayer index of refraction shifts near the limits of the lookup table's operational range are more accurate than those near the median of the biolayer index of refraction shift with respect to the operational range.

At biolayer index of refraction shifts less than 0.0299 RIU and greater than 0.0699 RIU, the inversion results are more accurate than biolayer index of refraction shifts near the median of 0.048 RIU. This trend is due to high and low values of biolayer index of refraction shift producing resonant shifts far from the median resonance wavelength shift with respect to the lookup table. Resonance shifts produced near the median resonance shift for each mode are a more common occurrence in the lookup table and will result in erroneous biolayer value sets being used to generate a best fit line.

Biolayer value sets that generate resonance shifts near the median of the resonance shift range have the greatest error. This occurs for biolayer index of refraction shifts that are approximately 0.048 RIU. There are a myriad of combinations of biolayer thickness and biolayer index of refraction that can achieve the resonance shifts produced by having biolayer indices of refraction near the median. The biolayer index of refraction shifts near the median of the lookup

table produces an elevated number of erroneous biolayer sets used to generate best fit lines compared to the lowest and highest index of refraction shifts. This specifically applies to biolayer index of refraction shifts because the sensor is 3 orders of magnitude more sensitive to biolayer index than to biolayer thickness.

3.4 Conclusion

The best fit algorithm works most effectively when the sensor variables produce resonance shifts at the extremes of the range of the lookup table. The most accurate inversion results occur when the biolayer thickness shifts are large, and accurate inversion results occur when the biolayer index of refraction shifts are far from the median (different from the median by an absolute value of about 0.022 RIU or 23% of the range). As with other inversion methods, the best fit algorithm accuracy would improve when applied to a sensor with greater sensitivity. This is because the larger resonance shifts for sensor variable shifts would result in biolayer variable shift sets used in the best fit lines that have a smaller range of biolayer variable shifts and thus more accurate biolayer shift sets used to generate the best fit line.

A method to improve the algorithm is to add a denser grid of simulated sensor variable values to the lookup table. The denser grid should focus on the biolayer variables: biolayer thickness and biolayer index of refraction. The number of computations is directly proportional to the time necessary for the computations. In this work the biolayer index of refraction computation density is 0.006 RIU and the biolayer thickness density is 3 nm. To make both densities twice as granular (i.e., a biolayer index of refraction density of 0.003 RIU and a biolayer thickness density of 1.5 nm) would increase the computational time 4-fold which would approach the limits of a medium grade workstation. The computational time would be about 48 hours.

Chapter 4

Rayleigh-anomaly-transmission sensors assisted by modal resonance effects

4.1 Physics behind transmission GMR

The rapid spectral variations produced by subwavelength waveguide gratings arise upon excitation of guided-mode resonance (GMR) by an incident beam of light [1]–[6]. The output of GMR devices is generally characterized by their spectral reflection response [7]–[15]. While not as widespread, there has been significant work done characterizing the transmission response of GMR devices [64]–[68]. In 1995, Magnusson and Wang first proposed bandpass, or transmission filters, which utilize multiple layers of high and low index dielectrics with a quarter-wavelength thickness, and two diffraction gratings [69]. The use of multiple layers to produce a transmission filter was further explored by Tibuleac in 1997 [70]. Ding and Magnusson designed and simulated a single layer device consisting of a diffractive grating that produces two resonances that occur near the same resonance wavelength [71]: they showed that a resonant mode strongly coupled to the diffraction grating and another mode with less coupling strength can produce low transmission sidebands and a high transmission peak, respectively [71]. The concept of multiple resonances forming the low transmission sidebands and high transmission peak was further analyzed and elaborated upon by Niraula et al. [7]. Lee et al. used a single grating with dual waveguides separated by an air gap to produce a transmission peak [72]. These works help form the foundation upon which GMR transmission filters exist.

4.2 Past implementation of transmission resonance in GMR devices

Guided-mode resonance (GMR) transmission filters have been designed and fabricated to serve as filters in the visible range to produce red, blue, and green light [73]. GMR transmission

devices have been applied to spectral imaging, and tunable filters among other applications [74]–[76].

Lord Rayleigh makes the first mention of the Rayleigh anomaly [77]. The Rayleigh anomaly has been used to limit the transmission bandwidth of a GMR-SPR (guided-mode resonance and surface plasmon resonance) bandpass transmission filter [78]. Fannin et al. demonstrated shifting a spectral feature by shifting the Rayleigh point of a device; this device utilized GMR and SPR simultaneously [79].

Amin et al. designed a guided-mode resonance (GMR) transmission filter and investigated the Rayleigh anomaly in theory and experiment [1]. This study utilizes amorphous silicon (a-Si) as a grating and waveguide, and silicon oxide (SiO_2) as the substrate to make a GMR structure in air. Multiple GMR parameters are simulated to demonstrate the interaction between a guided-mode resonance transmission peak and the Rayleigh anomaly. The initial GMR design is established via particle swarm optimization, and subsequent designs include parameter deviations to achieve a desired resonance wavelength. In the work by Amin et al., a guided-mode resonance transmission peak is designed to be coincident with the Rayleigh anomaly, and it is shown that the result is a sharper and more efficient transmission peak [1]. There are multiple designs and simulations used to illustrate the transmission peak enhancement by the Rayleigh anomaly. In addition, a device is fabricated, and the Rayleigh enhanced transmission peak is shown via experiment. The sharp transmission peak is explained as the result of the first order transmission ($T_{\pm 1}$) decreasing rapidly at the Rayleigh point and converting from a propagation mode to an evanescent mode.

The article by Magnusson [80] simulates the design of a GMR structure to illustrate the use of the Rayleigh angle in concert with the GMR effect. A flat top reflector over an angular

spectrum, from the negative Rayleigh angle to the positive Rayleigh angle, is designed and the spectrum simulated. The higher transmission orders rapidly gain diffraction efficiency at angles greater than the absolute value of the Rayleigh angle, and they rapidly lose diffraction efficiency to the first order reflection (R_0) wave at angles less than the absolute value of the Rayleigh angle.

Gao et al. [81] showed that surface plasmon polariton effects can be enhanced using the Rayleigh anomaly. Deb et al. [82] designed, fabricated, and experimentally measured super-modes produced by a GMR sensor. Super-mode is the nomenclature given to the guided-mode reflection peak assisted by the Rayleigh anomaly (affected by the superstrate or bulk index of refraction). This work shows, via simulation and experiment, that sensitivities to bulk refractive index can approach the period of the device. In the work by Deb et al. [82], a 2D GMR device design is used; in our work reported here, we use a less complex 1D device, and we utilize transmission peaks to monitor bulk RIU.

Nazirizadeh et al. [83] use an industry available GMR sensor to monitor the surface mass of biomolecules on the sensor. To do this, a GMR peak at the cut-off wavelength (Rayleigh wavelength) is monitored. The bulk media is chosen such that the effective refractive index of the grating is equal to that of the substrate. As biomolecules accumulate on the sensor surface, the effective refractive index of the grating increases and the GMR peak at the Rayleigh wavelength increases in intensity. Thus, this study monitors GMR peak intensity and correlates this value to biomolecule agglomeration on the GMR sensor surface.

It has been demonstrated in a GMR-SPR hybrid device that as the bulk index shifts, features of the spectrum can shift at the same rate as the Rayleigh wavelength produced by the cover of the device [79]. This is similar to our work; however, we use GMR interacting with the Rayleigh anomaly, therefore, we do not require metal in our device.

4.3 Design parameters

First, we selected materials for the grating, waveguide, and substrate: we chose silicon (~3.49 RIU) for the grating and waveguide, and quartz (1.5 RIU) as the substrate. An advantage of this choice is that SOQ (silicon on quartz) wafers are prevalent in industry and readily available from suppliers. Also, silicon is non-absorptive in the telecom band – the spectrum of interest. To find device parameters that have the potential to produce a resonance-assisted Rayleigh transmission peak in the telecom band, we ran nearly 100 simulations and evaluated the resultant spectrum. To keep the investigative process simple, we set the period of the periodic structure to 1000 nm, and we cycled through permutations of grating thicknesses and waveguide thicknesses. For each set of given grating thickness and waveguide thickness values, we evaluate the transmissivity by running an RCWA (rigorous coupled-wave analysis) simulation, via MATLAB, across the wavelength spectrum of interest versus values of fill factor (**Figure 4-1**).

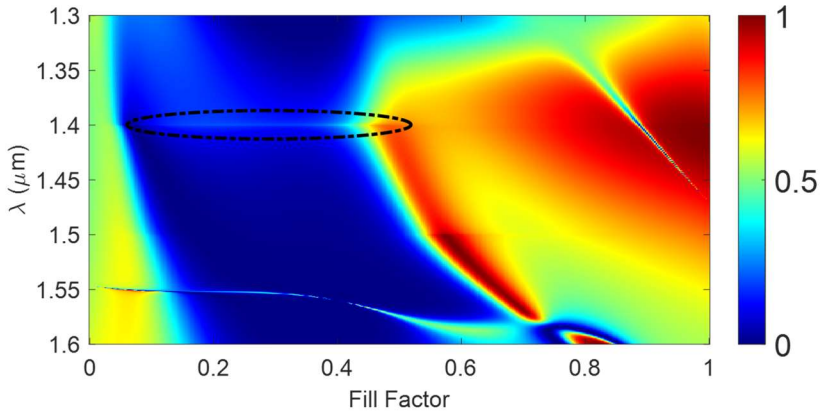

Figure 4-1 TE-polarization transmission colormap for wavelength vs. fill-factor. The periodic structure has a period (Λ) of 1000 nm, grating thickness (d_g) of 300 nm, homogeneous layer thickness (d_h) of 300 nm, and a bulk index of refraction (n_{bulk}) of 1.4 RIU. The spectrum feature of interest near the Rayleigh wavelength is indicated inside the black dash-dot oval.

In our search for ideal GMR parameters, grating thicknesses from 300 nm to 2100 nm were cycled through in increments of 300 nm, and waveguide thicknesses from 0 nm to 2100 nm were cycled through in increments of 350 nm.

The ideal bulk index of refraction sensor will have an operation span of index of refraction from about 1.35 RIU to 1.45 RIU. Therefore, the bulk refractive index unit (RIU) is set to 1.4 RIU (the median of the desired operation range) for the simulations. For a given simulation, the 2D color map is analyzed to determine if there is a transmission peak at the Rayleigh wavelength. The Rayleigh wavelength is 1400 nm for a period of 1000 nm and a bulk refractive index of 1.4 RIU; this calculation is based on Equation 4.1.

$$\lambda_R = n_{bulk} \times \Lambda \tag{4.1}$$

In Equation 4.1 λ_R, n_{bulk}, and Λ are Rayleigh wavelength, bulk index of refraction, and period, respectively. As shown in **Figure 4-6**, from a fill factor of about 0.1 to 0.4 there is a transmission peak that is present but not very efficient for a waveguide (homogeneous layer) thickness (d_h) of 300 nm and a grating thickness (d_g) of 300 nm.

4.3.1 Favorable spectrum description

We selected a fill factor (F) of 0.145 from the area of interest in **Figure 4-1**. At this F value there is a distinct transmission peak at the Rayleigh wavelength (1400 nm), and the sidebands of the peak do not decrease to zero for several tens of nanometers. This is important because for the Rayleigh anomaly to produce a peak of interest, a GMR evanescent mode must shape the spectrum over ~100 nm. For our device, the operational range for n_{bulk} is 1.35 to 1.45 RIU; according to Equation 4.1, since Λ equals 1000 nm, the Rayleigh peak will shift from 1350 to 1450 nm. Device parameters are selected such that a GMR shapes the spectrum from about 1350

to 1450 nm, and over this span of wavelengths the Rayleigh anomaly will produce a transmission peak.

After selecting a fill factor (F) of 0.145, we simulate the spectrum of interest at various waveguide thickness (d_h) values to determine at what value is the transmission peak best suited to a device: d_g is fixed at 300 nm **Figure 4-6**. As shown in **Figure 4-6**, the transmission peak at 1400 nm is present for values of d_h within the dash-dot oval. We select d_h values of interest from this region due to the large FWHM caused by GMR spectral shaping and the high transmissivity at 1400 nm.

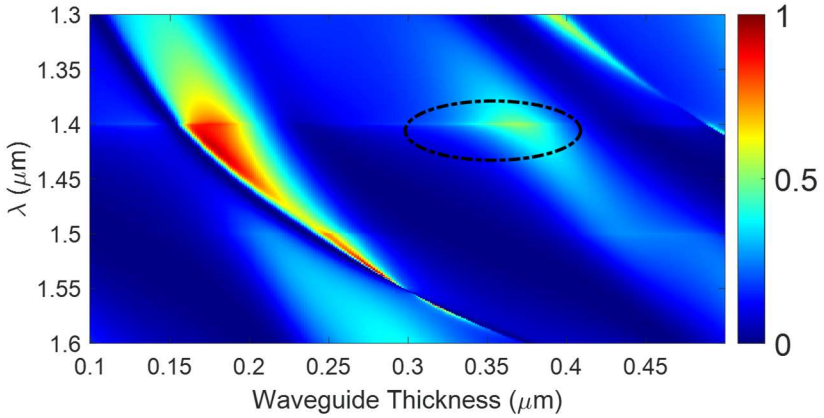

Figure 4-2 TE-polarization transmission colormap for wavelength vs. waveguide thickness. The periodic structure has a period (Λ) of 1000 nm, grating thickness (d_g) of 300 nm, fill factor (F) of 0.145, and a bulk index of refraction (n_{bulk}) of 1.4 RIU. The spectrum feature of interest near the Rayleigh wavelength is indicated inside the black dash-dot oval.

Analyzing the 2D transmittance color map of wavelength vs. waveguide thickness, it is not immediately evident which value of waveguide thickness would contribute to the best device. Thus, the 2D transmissivity color map of wavelength vs. waveguide thickness is used to narrow down the best potential waveguide thicknesses. The waveguide thicknesses (d_h) of interest are in

the interval from 290 nm to 400 nm (**Figure 4-6**). Next in the parameter selection process, the peak transmittance, and the span of bulk refractive indexes for which the device is effective are evaluated for the narrowed down set of waveguide thicknesses (**Figure 4-6**).

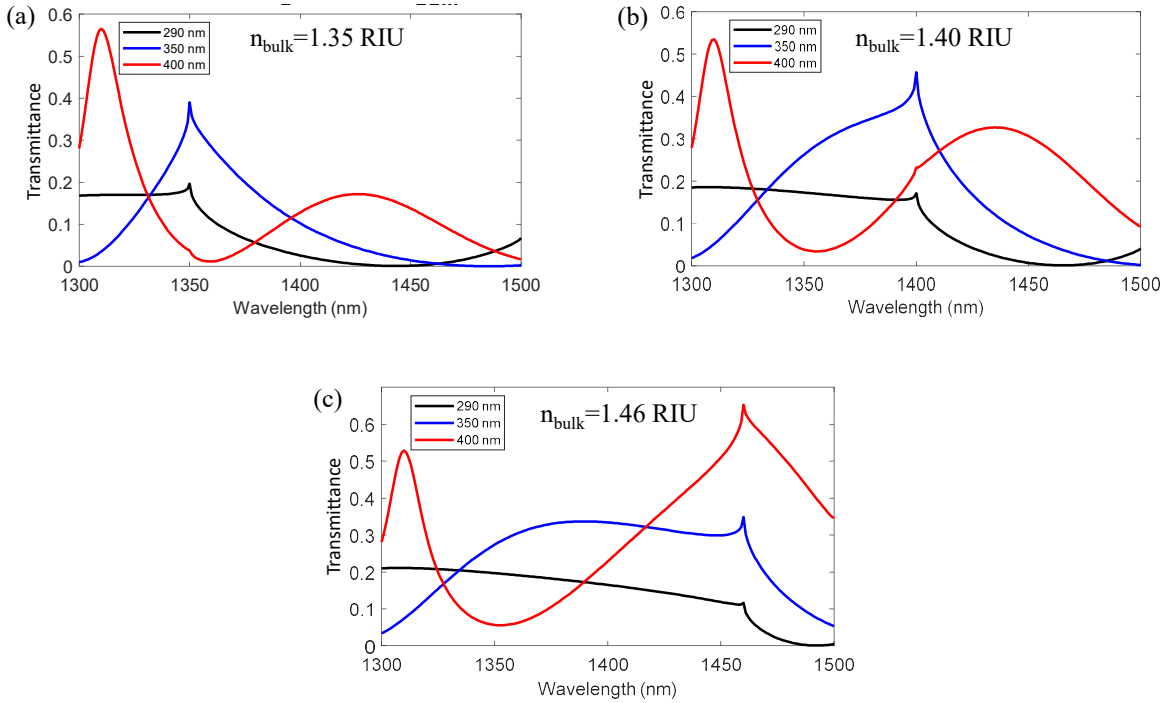

Figure 4-3 TE-polarization sensor response to optimize waveguide thickness. TE wavelength vs. transmissivity for a GMR structure with a period (Λ) of 1000 nm, grating thickness (d_g) of 300 nm, and fill factor (F) of 0.145. The black, blue, and red lines indicate a waveguide thickness (d_h) of 290 nm, 350 nm, and 400 nm, respectively. The transmission spectra are shown at bulk index of refraction (n_{bulk}) (a) 1.35, (b) 1.40, and (c) 1.46 RIU.

To determine the ideal waveguide thickness, we simulate the transmittance for the Rayleigh sensor at three values of d_h (290 nm, 350 nm, and 400 nm). For each value of d_h we simulate the bulk index of refraction n_{bulk} at 1.35 RIU, 1.4 RIU, and 1.46 RIU. We choose n_{bulk} values in this span because these indexes are well suited to biological sensing – the proposed use of the sensor.

At n_{bulk}=1.35 RIU, **Figure 4-6**a shows that d_h=400 nm does not produce a detectable peak at the Rayleigh wavelength 1350 nm: a disturbance can be seen at this wavelength, but the feature is not suited to sensing applications. At n_{bulk}=1.35 RIU and d_h=350 nm the transmission peak is detectable and prominent. At n_{bulk}=1.35 RIU and d_h=290 the transmission peak is detectable in the simulated spectrum, but it is weak.

For the other simulated n_{bulk} values, the device with d_h=400 nm has a peak that is not detectable at n_{bulk}=1.4 RIU (**Figure 4-6**b), but at n_{bulk}=1.46 RIU this device has a peak with relatively high transmittance (~0.65) (**Figure 4-3** c). For the device with d_h=350, there is a detectable transmission peak at n_{bulk}=1.4 RIU (**Figure 4-3** b),and at 1.46 RIU the transmission peak has decreased in transmissivity but it is still detectable (**Figure 4-3** c). For the device with d_h=290 nm, there is a notch at n_{bulk}=1.4 RIU but the peak has a low transmissivity (**Figure 4-3** b), and at n_{bulk}=1.46 RIU the device has a notch with even lower transmissivity (**Figure 4-3** c).

Evaluating the device's performance over the n_{bulk} span of interest, we select a waveguide grating thickness of 350 nm. The device with d_h=350 nm produces a detectable transmission peak over the n_{bulk} span of interest (1.35 to 1.46 RIU).

After comparing different waveguide thickness (d_h) values and determining a d_h value of 350 nm to be ideal, the last GMR-assisted Rayleigh device parameter that we optimize is the grating thickness (d_g). To do this we simulate the transmission response of the device over the spectrum of interest for d_g values from 100 nm to 500 nm as shown in **Figure 4-4** .

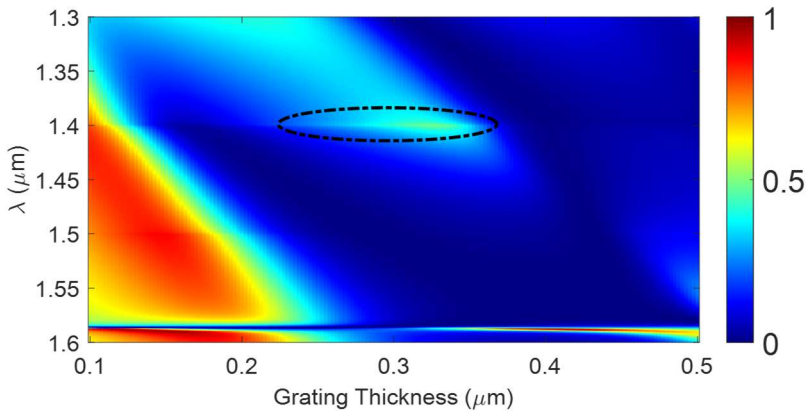

Figure 4-4 TE-polarization transmission colormap for wavelength vs. grating thickness. The periodic structure has a period (Λ) of 1000 nm, waveguide thickness (d_h) of 350 nm, fill factor (F) of 0.145, and a bulk index of refraction (n_{bulk}) of 1.4 RIU. The spectrum feature of interest at the Rayleigh wavelength is indicated by the black dash-dot oval.

The limited set of d_g values, which have a transmission peak at the Rayleigh wavelength (1400 nm), include the interval from 260 nm to 350 nm. To determine which d_g is best suited to our device we simulated d_g values 260 nm, 300 nm, and 350 nm for bulk refractive index (n_{bulk}) values in our device's ideal operating range (**Figure 4-5**).

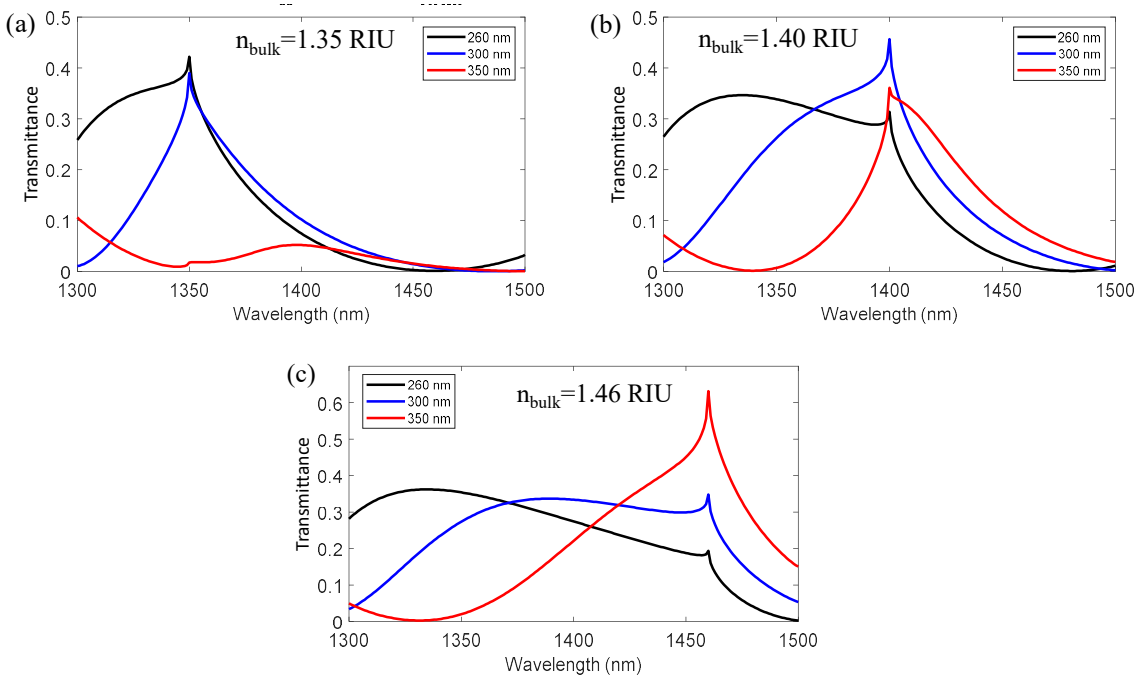

Figure 4-5 TE-polarization wavelength vs. transmissivity for grating thickness optimization. The periodic structure has a period (Λ) of 1000 nm, waveguide thickness (d_h) of 350 nm, and fill factor (F) of 0.145. The black, blue, and red lines indicate a grating thickness (d_g) of 260 nm, 300 nm, and 350 nm, respectively. The transmission spectra are shown at bulk indexes of refraction (n_{bulk}) (a) 1.35, (b) 1.40, and (c) 1.46 RIU.

For the simulated device with d_g=350 nm, at n_{bulk}=1.35 RIU (**Figure 4-5**a) there is a disturbance at the Rayleigh wavelength (1350 nm) but not a detectable transmission peak; at n_{bulk}=1.4 RIU the device has a detectable transmission peak (**Figure 4-5**b); and at n_{bulk}=1.46 RIU the device has a detectable transmission peak with a relatively high transmissivity (~0.63) (**Figure 4-5**c). For the device with d_g=300 nm, at n_{bulk}=1.35 RIU there is a detectable peak (**Figure 4-5**a); at n_{bulk}=1.4 RIU there is a detectable peak with a relatively high transmissivity (~0.47) (**Figure 4-5**b); and at n_{bulk}=1.46 RIU there is a peak that has a prominent shoulder on the

lower wavelength side, but it should be detectable (**Figure 4-5**c). Finally, for the device with d_g=260 nm, at n_{bulk}=1.35 RIU there is a detectable peak with a relatively high transmissivity (~0.41) (**Figure 4-5**a); at n_{bulk}=1.4 RIU the peak has a prominent shoulder on the lower wavelength side, although the shoulder has a higher transmissivity than the peak, the peak may be detectable (**Figure 4-5**b); and at n_{bulk}=1.46 RIU there is a notch at the Rayleigh wavelength (1460 nm) and this feature is not ideal for our sensor (**Figure 4-5**c).

Based on the attributes of the sensors at each evaluated value of grating thickness (d_g), the selected value of d_g is 300 nm. At d_g=300 nm the Rayleigh anomaly can be detected at values of bulk refractive index (n_{bulk}) from 1.35 RIU to 1.46 RIU.

The procedure traversed details how fill factor, waveguide thickness, and grating thickness are varied to determine which parameter values will result in an efficient transmission peak that is detectable for the bulk index values of interest.

A relatively broad peak is found to be an indicator of a transmission peak that will shift with the Rayleigh wavelength (controlled by adjusting the bulk or substrate index of refraction). In this simulation we change the bulk index of refraction to shift the transmission peak. The resultant device, from the process detailed in this section, is a GMR-assisted Rayleigh sensor for bulk index of refraction with a high sensitivity. The Rayleigh anomaly occurs at the bulk (cover) RIU multiplied by the period. Thus, our GMR-assisted Rayleigh transmission sensor can have a sensitivity of 1000 nm/RIU: this is because the period of the device was chosen to be 1000 nm.

4.4 Rayleigh sensor characterization

Based on the parameter optimization that was performed in the last section, the GMR-assisted Rayleigh bulk index of refraction sensor parameters are grating thickness (d_g) equal to

300 nm, waveguide thickness (d_w) equal to 350 nm, fill factor (F) equal to 0.145, and period (Λ) equal to 1000 nm ().

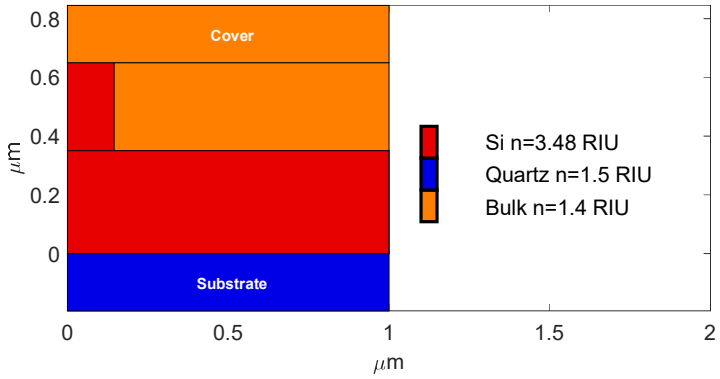

Figure 4-6 Optimized GMR-assisted Rayleigh transmission sensor. The sensor optimized in the last section consists of silicon on quartz (SOQ): a silicon grating and homogeneous layer with a quartz substrate. The grating parameters are as follows: fill factor (F) = 0.145, grating thickness (d_g) = 300 nm, waveguide thickness (d_h) = 350 nm, and period (Λ) = 1000 nm.

Figure 4-7 shows the transmission response of the device across the n_{bulk} operational range.

(a)

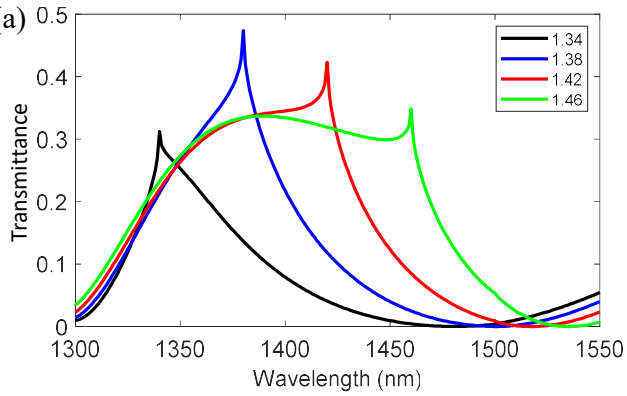

(b)

Bulk Index (RIU)	Peak Wavelength (nm)	Sensitivity (nm/RIU)
1.34	1340	-
1.46	1460	1000

Figure 4-7 Performance of the sensor in **Figure 4-6**. (a) The TE-polarization transmittance vs. wavelength for the sensor in **Figure 4-6** at different values of bulk index of refraction: 1.34 (black), 1.38 (blue), 1.42 (red), and 1.46 RIU (green). (b) A table with values of bulk index, peak wavelength, and bulk index sensitivity.

The Rayleigh assisted transmission peak is shown to shift significantly as the n_{bulk} is varied from 1.34 RIU to 1.46 RIU (**Figure 4-7**a). This device has a bulk refractive index sensitivity $\{S(n_{bulk})\}$ of 1000 nm/RIU. This value surpasses the sensitivity of various sensors, published previously.

$$S(n_{bulk}) = {\Delta\lambda}/{\Delta n_{bulk}} = \Lambda \tag{4.2}$$

The expression above denotes the bulk index of refraction sensitivity $\{S(n_{bulk})\}$. In the above expression, $\Delta\lambda$, and Δn_{bulk} are the change in resonance wavelength, and the change in bulk index of refraction, respectively. Λ is the period of the device. Equation 4.2 states that the sensitivity of the GMR-assisted Rayleigh sensor is equal to the period of the device. Using the optimization method detailed in this work, different sets of GMR parameter values can be realized and used to produce additional GMR-assisted Rayleigh sensors/devices.

4.4.1 Additional Rayleigh sensor designs

The GMR-assisted Rayleigh device in **Figure 4-8**a has a grating and waveguide that both consist of silicon, and the substrate is quartz. The period, fill factor, grating thickness, and waveguide thickness are 1000 nm, 0.4, 300 nm, and 500 nm, respectively. This device has a detectable Rayleigh anomaly transmission peak for bulk refractive indexes from 1.35 RIU to 1.42 RIU. The sensitivity of this Rayleigh device is 1000 nm/RIU. This device has a detection range that is smaller than the device in **Figure 4-6** , but the fill factor is larger than that of the device in **Figure 4-6** : increasing the ease of fabrication – a significant attribute.

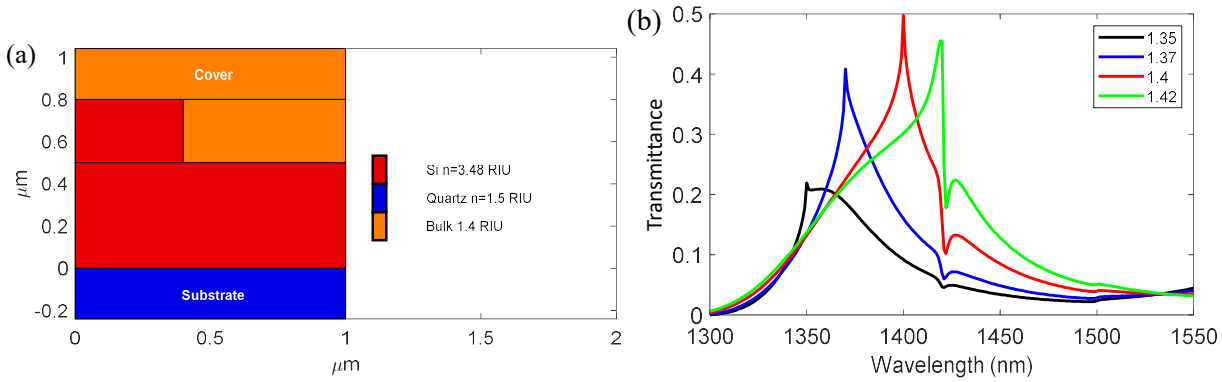

(c)

Bulk Index (RIU)	Peak Wavelength (nm)	Sensitivity (nm/RIU)
1.35	1350	-
1.42	1420	1000

Figure 4-8 Second optimized sensor schematic and performance. (a) Periodic structure with grating parameters as follows: fill factor (F) = 0.4, grating thickness (d_g) = 300 nm, waveguide thickness (d_h) = 500 nm, and period (Λ) = 1000 nm. (b) The TE-polarization transmittance vs. wavelength for the sensor in (a) at different values of bulk index of refraction: 1.35 (black), 1.37 (blue), 1.4 (red), and 1.42 RIU (green). (c) A table with values of bulk index, peak wavelength, and bulk index sensitivity.

The next GMR-assisted Rayleigh device is diagramed and characterized in **Figure 4-6**, and it consists of a silicon grating and silicon waveguide on a quartz substrate. The period, fill factor, grating thickness, and waveguide thickness are 1000 nm, 0.4, 300 nm, and 880 nm, respectively. The range over which bulk refractive index can be detected is from 1.355 RIU to 1.415 RIU. The sensitivity of this device over the effective detection range is 1000 nm/RIU. This device has the smallest range of n_{bulk} detection of the three original sensor designs presented in this work, but this device has the highest transmittance compared to the other two devices. Additionally, this device has a larger fill factor, compared to the sensor in **Figure 4-6** – making it easier to fabricate.

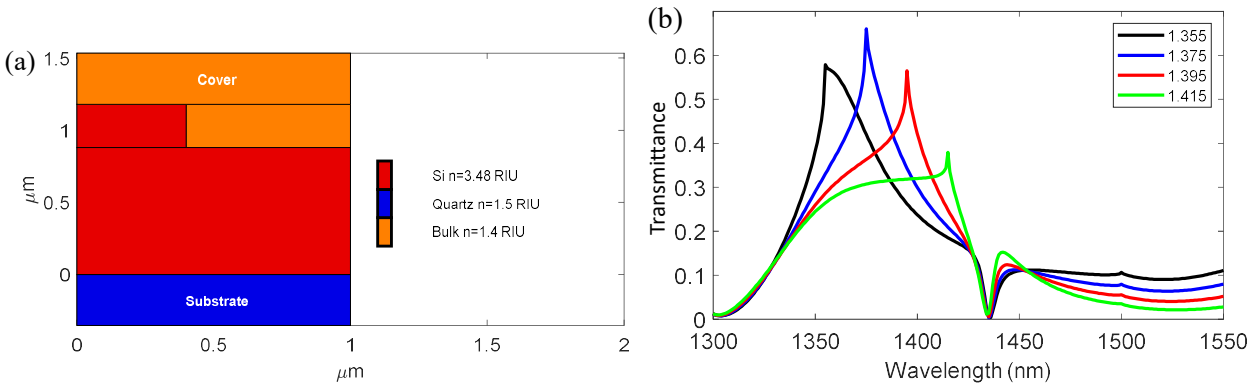

(c)

Bulk Index (RIU)	Peak Wavelength (nm)	Sensitivity (nm/RIU)
1.355	1355	-
1.415	1415	1000

Figure 4-9 Third optimized sensor schematic and performance. (a) GMR sensor with grating parameters as follows: fill factor (F) = 0.4, grating thickness (d_g) = 300 nm, waveguide thickness (d_h) = 880 nm, and period (Λ) = 1000 nm. (b) The TE transmissivity vs. wavelength for the sensor in (a) at different values of bulk index of refraction: 1.355, 1.375, 1.395, and 1.415 RIU. (c) A table with values of bulk index, peak wavelength, and bulk index sensitivity.

4.5 Discussion

4.5.1 Coupling orders

It is important to understand the reasons for the presence of Rayleigh transmission peaks; to this end we analyze the coupling orders for the sensors referenced previously in this paper (**Figure 4-6**, **Figure 4-8**a, and **Figure 4-9**a).

Figure 4-10 shows the zero-order reflection and transmission spectrum for the device in **Figure 4-6** . There is a reflection dip in the spectrum at 1242 that corresponds to the 2^{nd} diffraction order coupling to a TE_1 mode ($TE_{2,1}$) (**Figure 4-10**a and b). In the nomenclature $TE_{m,v}$, m is the diffraction order and v is the mode of resonant light. The half maxima of the transmission peak occur at 1343 nm and 1416 nm where the $TE_{2,1}$ mode is still present in the analysis of coupling order amplitudes (**Figure 4-10**c and e); the $TE_{2,1}$ mode is also present at the GMR-assisted Rayleigh transmission peak at 1400 nm (**Figure 4-10**d). The $TE_{2,1}$ evanescent mode shapes the spectrum over the wavelength range of the Rayleigh sensor, and this fact allows the Rayleigh anomaly to produce a peak. Typically, the Rayleigh anomaly is a simple spectral irregularity.

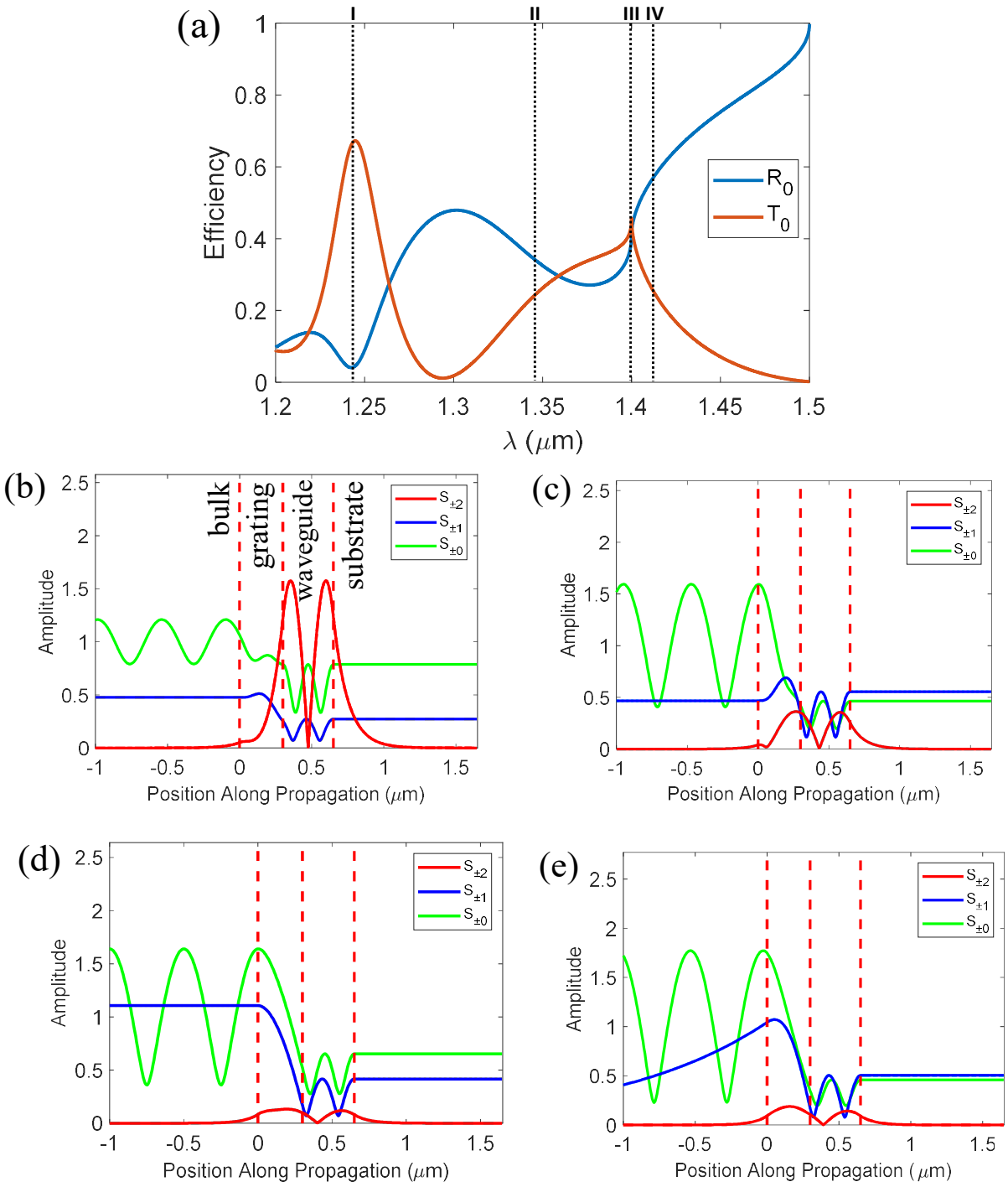
(a)
I
II
III IV
Efficiency
λ (μm)
R0
T0
(b)
bulk
grating
waveguide
substrate
Amplitude
Position Along Propagation (μm)
S±2
S±1
S±0
(c)
(d)
(e)

Figure 4-10 Neighboring GMR assists Rayleigh transmission peak for the sensor in **Figure 4-6** (a) TE-polarization wavelength vs. efficiency response for the sensor in **Figure 4-6** with bulk index set to 1.4 RIU: zero-order reflection (blue) and transmission (orange). In graph (a) the roman numerals I, II, III, and IV indicate the wavelengths 1242, 1343, 1400, and 1416 nm, respectively. Amplitudes of coupling orders for graph (a) at the resonant wavelength (b) 1242 nm, the half maxima of the Rayleigh transmission peak (c) 1343 nm and (e) 1416 nm, and at the Rayleigh transmission peak (d) 1400 nm.

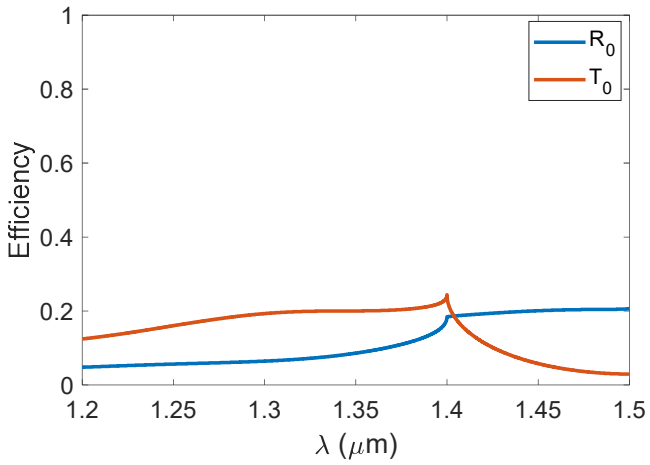

Figure 4-11 Rayleigh anomaly produced by the sensor in **Figure 4-6** with substrate index of refraction set to 3.0 RIU. The bulk index of refraction is 1.4 RIU. The zero-order transmission is shown with the orange line and the zero-order reflection is shown with the blue line.

When the substrate index of refraction is changed to 3.0 RIU for the sensor in **Figure 4-6**, the Rayleigh anomaly no longer generates a high efficiency peak (**Figure 4-11**). The neighboring GMR is not present to shape the spectrum. The high substrate RIU does not allow evanescent orders to couple to the device, and the lack of GMR spectral shaping causes the Rayleigh anomaly to produce a notch instead of a peak.

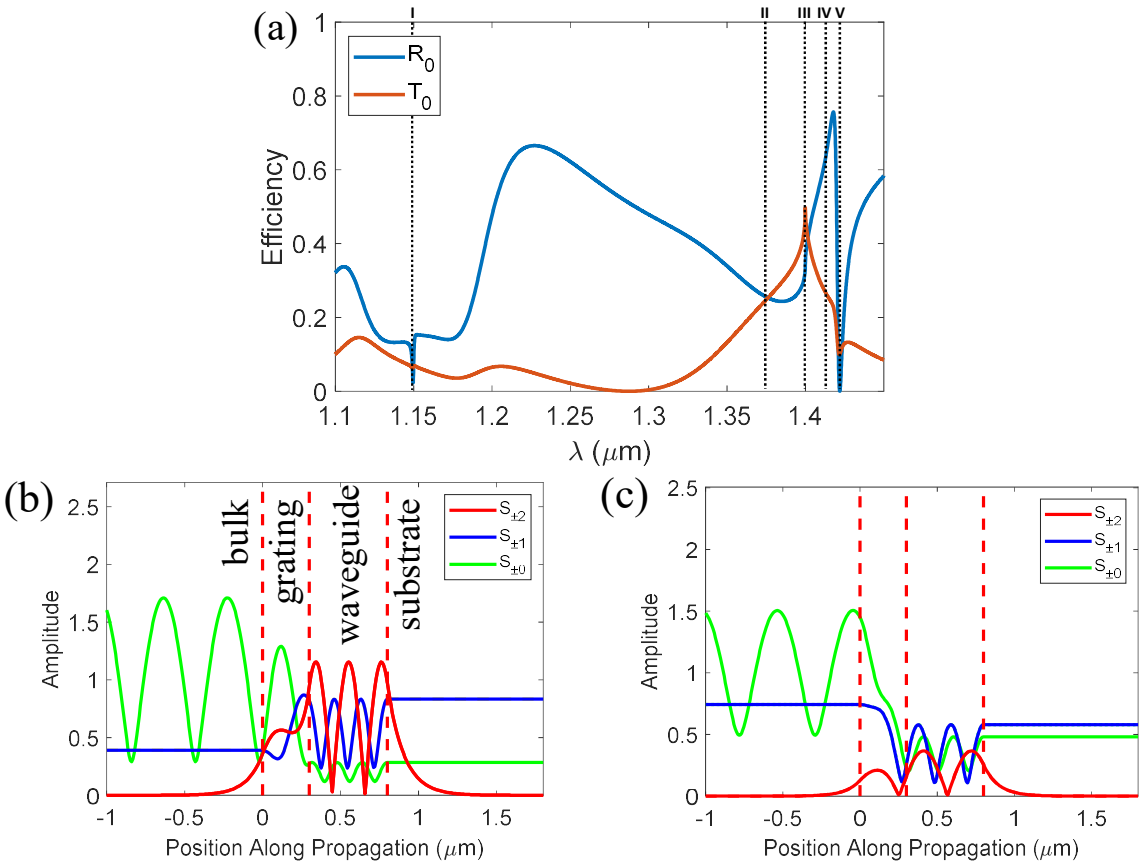
(a)
I
II
III
IV
V
R0
T0
Efficiency
λ (μm)
(b)
bulk
grating
waveguide
substrate
S±2
S±1
S±0
Amplitude
Position Along Propagation (μm)
(c)
S±2
S±1
S±0
Amplitude
Position Along Propagation (μm)

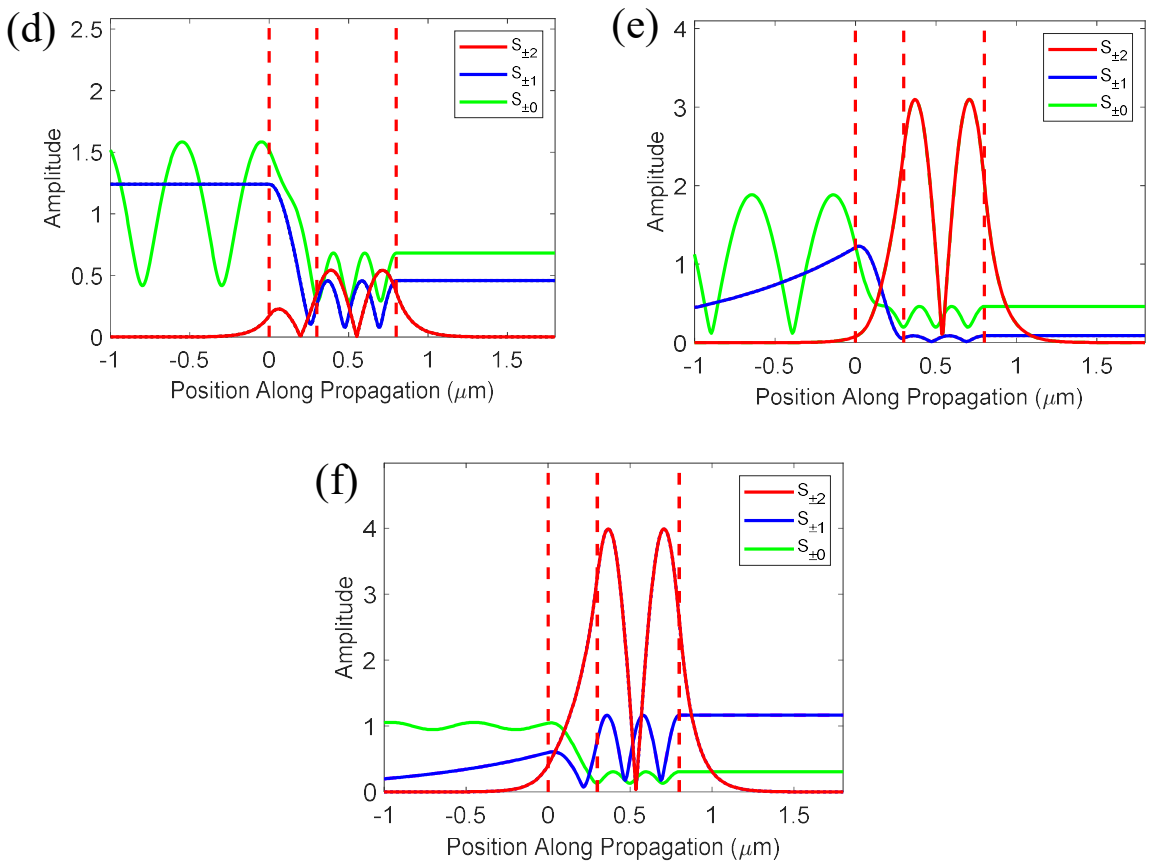

Figure 4-12 Two neighboring guided-mode resonances assist the Rayleigh transmission peak for the sensor in **Figure 4-8**a. (a) TE-polarization wavelength vs. efficiency response for the sensor in **Figure 4-8**a with bulk index set to 1.4 RIU: zero-order reflection (blue) and transmission (orange). In graph (a) the roman numerals I, II, III, IV, and V indicate the wavelengths 1150, 1375, 1400, 1418 nm, and 1422 nm, respectively. Amplitudes of coupling orders for graph (a) at the resonant wavelengths (b) 1150 nm and (f) 1422, the half maxima of the transmission Rayleigh peak (c) 1375 nm and (e) 1418 nm, and at the Rayleigh transmission peak (d) 1400 nm.

The spectrum for the GMR-assisted Rayleigh sensor in **Figure 4-8** a (n_{bulk} = 1.4 RIU) is shown in **Figure 4-12**a. The $TE_{2,2}$ mode produces a reflection dip caused by GMR at 1150 nm (**Figure 4-12**a). The coupling order amplitudes at 1150 nm show that the 2nd diffraction order couples to a TE_2 mode (**Figure 4-12**b). The Rayleigh peak lower wavelength half maximum

(1375 nm) and the Rayleigh peak (1400 nm) are shaped by the 2nd diffraction order coupling to a TE_2 mode (**Figure 4-12**c and d). The GMR generated by the $TE_{2,1}$ mode produces a fano-shaped response in the reflection spectrum near 1422 nm (**Figure 4-12**a). The coupling order amplitudes at 1422 nm show the 2nd diffraction order coupling to a TE_1 mode (**Figure 4-12**f). The higher wavelength half maximum (1418 nm) is shaped by the 2nd diffraction order coupling to a TE_1 mode (**Figure 4-12**e).

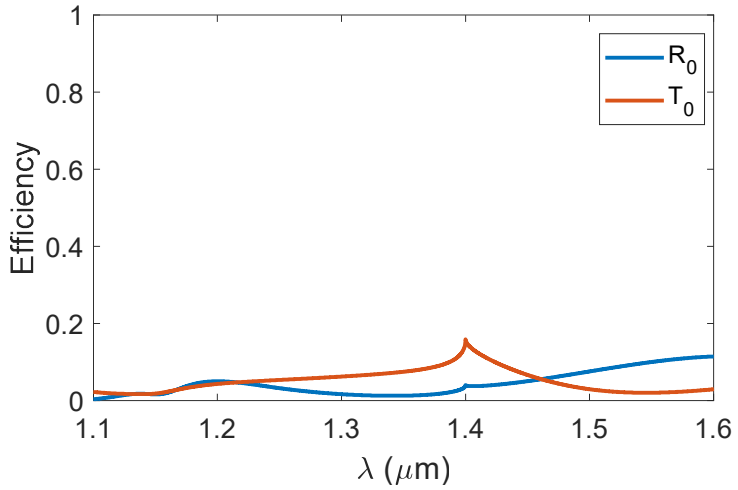

Figure 4-13 Rayleigh anomaly produced by the sensor in **Figure 4-8**a with substrate index of refraction set to 3.75 RIU. The bulk index of refraction is 1.4 RIU. The zero-order transmission is shown with the orange line and the zero-order reflection is shown with the blue line.

When the substrate index of refraction is increased to 3.75 RIU for the sensor in **Figure 4-8** a, the guided-mode resonances are no longer present (**Figure 4-13**). As a result, the Rayleigh anomaly at 1400 nm no longer produces a peak with high efficiency.

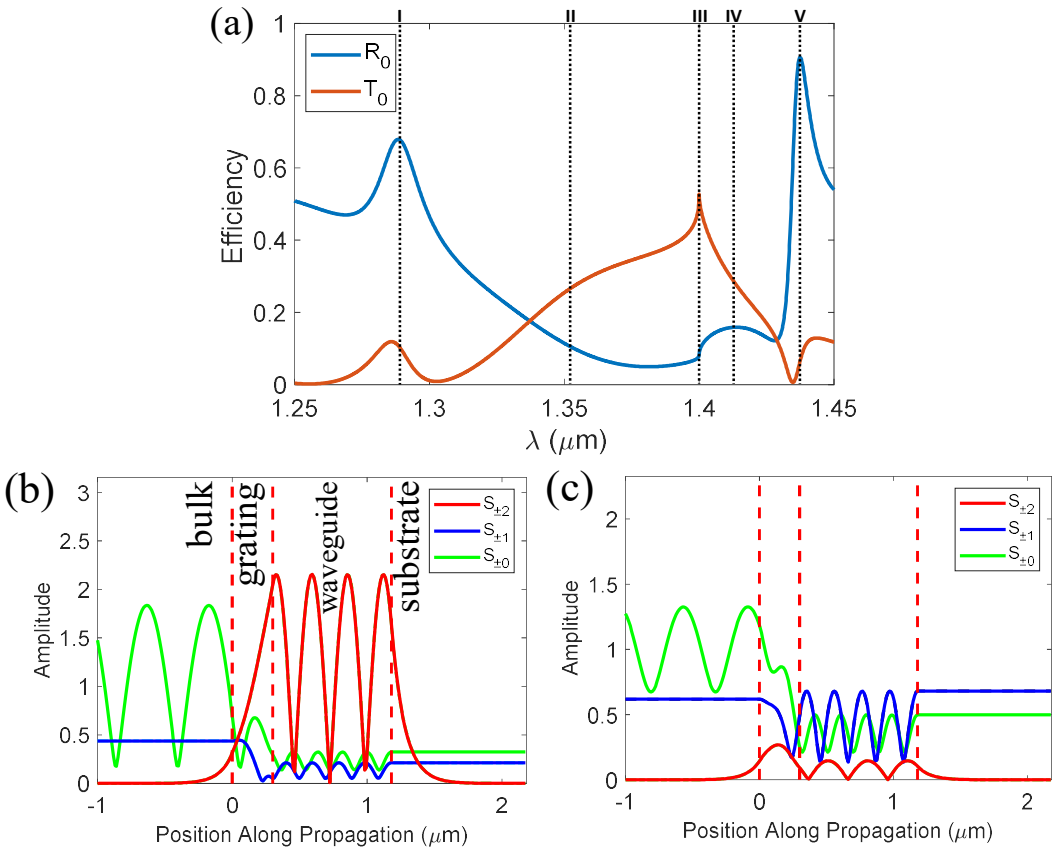
(a)
I
II
III
IV
V
R0
T0
Efficiency
λ (μm)
(b)
bulk
grating
waveguide
substrate
S±2
S±1
S±0
Amplitude
Position Along Propagation (μm)
(c)
S±2
S±1
S±0
Amplitude
Position Along Propagation (μm)

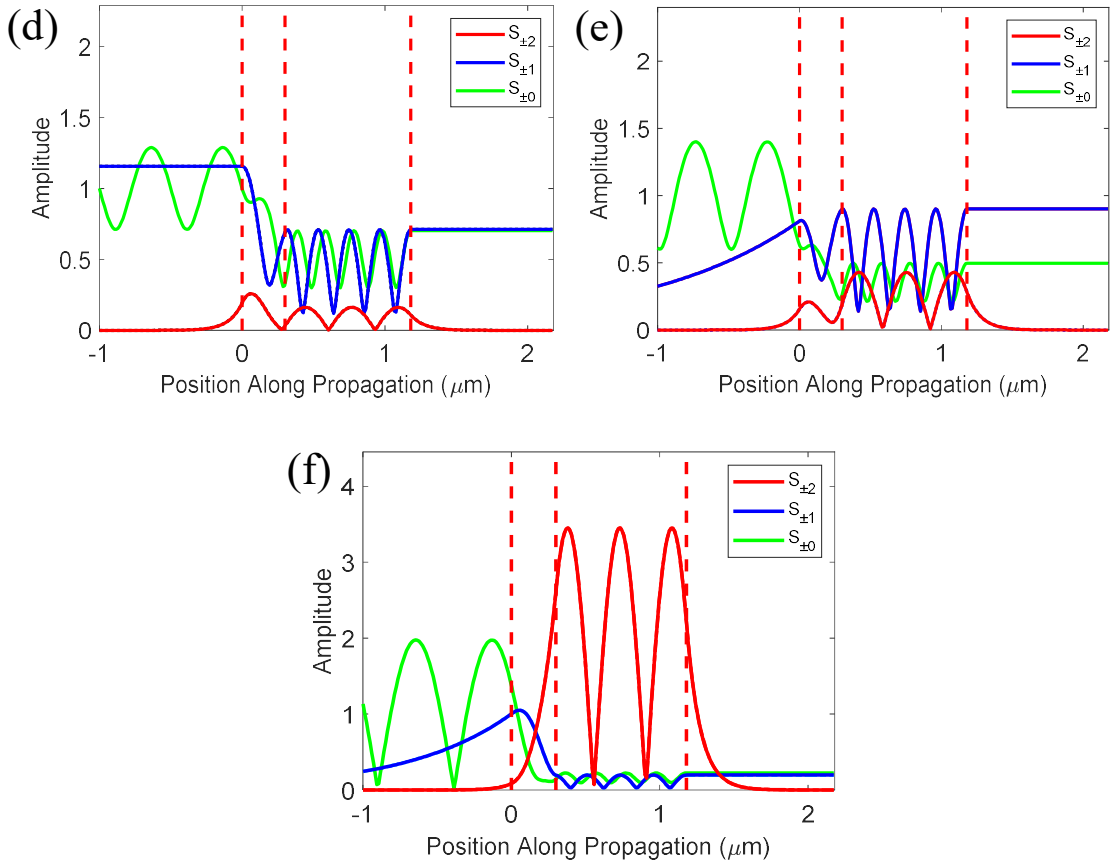

Figure 4-14 Two neighboring guided-mode resonances assist the Rayleigh transmission peak for the sensor in **Figure 4-9**a. (a) TE-polarization wavelength vs. efficiency response for the sensor in **Figure 4-9**a with bulk index set to 1.4 RIU: zero-order reflection (blue) and transmission (orange). In graph (a) the roman numerals I, II, III, IV, and V indicate the wavelengths 1288, 1352, 1400, 1415 nm, and 1437 nm, respectively. Amplitudes of coupling orders for the device in graph (a) at the resonant wavelengths (b) 1288 nm and (f) 1437, the half maxima of the Rayleigh transmission peak (c) 1352 nm and (e) 1415 nm, and at the Rayleigh transmission peak (d) 1400 nm.

The sensor in **Figure 4-9**a produces a GMR-assisted Rayleigh transmission peak at 1400 nm when the bulk index of refraction is set to 1.4 RIU (a). The $TE_{2,3}$ mode produces a GMR reflection peak near 1288 nm (**Figure 4-14**a). The coupling order amplitudes at 1288 nm show that the 2nd diffraction order couples to a TE_3 mode (**Figure 4-14**b). The half maxima of the

Rayleigh transmission peak, at 1352 and 1415 nm, and the Rayleigh transmission peak at 1400 nm are all shaped by the 2nd diffraction order coupling to a TE_3 mode (**Figure 4-14**c, d, and e). The significant transmission dip (reflection peak) in the spectrum near 1437 nm (**Figure 4-14**a) is due to the 2nd diffraction order coupling to a TE_2 mode and producing a GMR (**Figure 4-14**f).

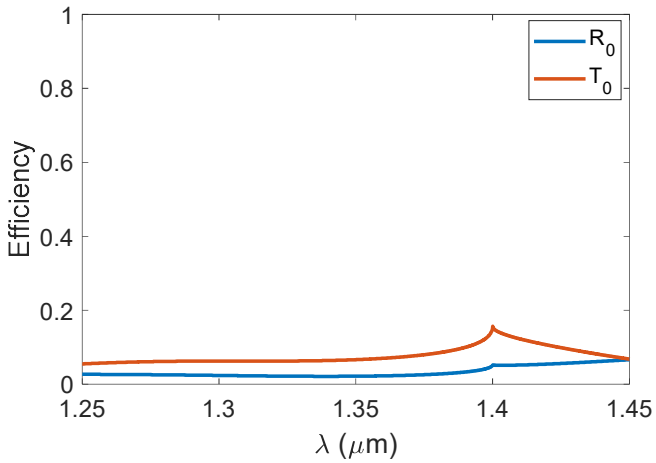

Figure 4-15 The Rayleigh anomaly produced by the sensor in **Figure 4-9**a with substrate index of refraction set to 3.75 RIU. The bulk index of refraction is 1.4 RIU. The first order transmission is shown with the orange line and the first order reflection is shown with the blue line.

When the substrate index of refraction is increased to 3.75 RIU, the guided mode resonances are no longer neighboring the Rayleigh anomaly. As a result, the Rayleigh anomaly no longer produces a high transmittance peak.

4.5.2 Resonance-assisted Rayleigh sensor substrate options

It is of value to determine if a lower index substrate (potentially UV curable resin with n=1.35 RIU) produces a better response for our devices. It can be seen in **Figure 4-16** that the transmittance for the UV curable substrate is ~37% greater than the device with quartz substrate.

The improvement in transmittance shows that future work with a lower index substrate can yield an attractive GMR-assisted Rayleigh transmission sensor.

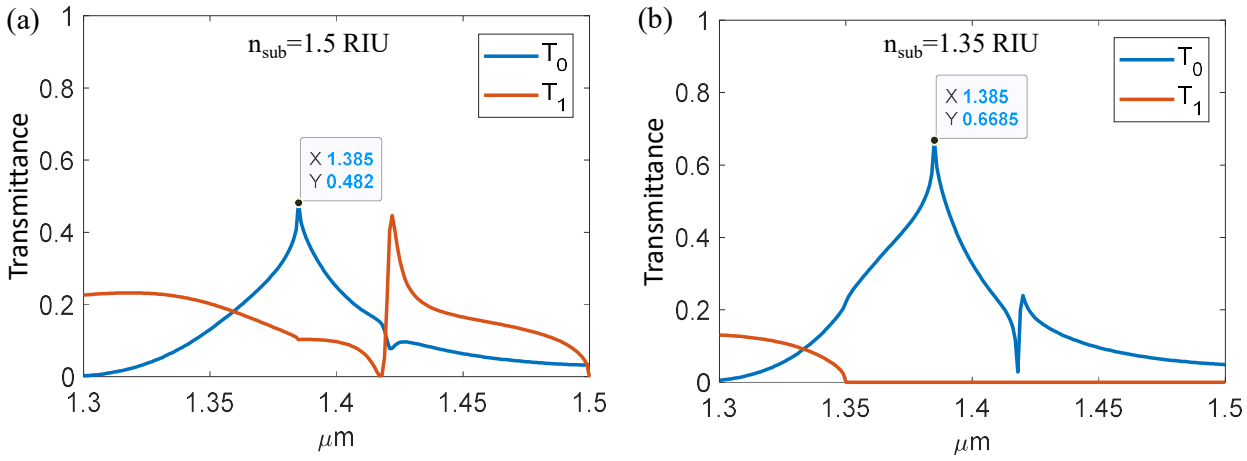

Figure 4-16 The TE-polarization transmissivity vs. wavelength for the sensor in **Figure 4-8**a. The bulk index of refraction is 1.385 RIU and substrate index of refraction values are (a) 1.5 RIU (quartz), and (b) 1.35 RIU (UV curable resin). In both graphs the value of the substrate index of refraction is indicated using n_{sub}.

The proposed Rayleigh assisted device in **Figure 4-9**a can also be further optimized with the use of UV curable resin as the substrate as opposed to quartz. It is shown in **Figure 4-17**b that the lower index of refraction of the UV curable resin eliminates the first order transmission mode at a wavelength lower than the GMR-assisted Rayleigh transmission peak. For this device (**Figure 4-9**a), this translates into a 38% increase in transmittance: around 0.90 transmittance for the UV curable resin (UVCR) substrate.

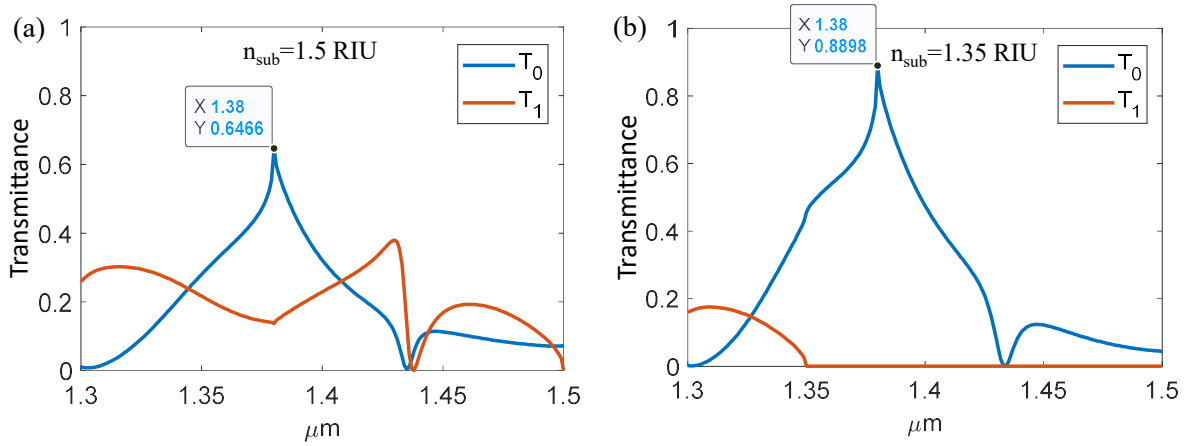

Figure 4-17 The TE-polarization transmissivity vs. wavelength for the sensor in **Figure 4-9**a. The bulk index of refraction is 1.38 RIU and substrate index of refraction values are (a) 1.5 RIU (quartz), and (b) 1.35 RIU (UV curable resin). In both graphs the value of the substrate index of refraction is indicated using n_{sub}.

We compare UV curable resin (UVCR) substrate to quartz substrate for use in the device in **Figure 4-6**. To compare UVCR substrate (n=1.35 RIU) to quartz substrate (n=1.5 RIU), we run simulations keeping all parameters and indexes of our optimized Rayleigh sensor constant, except the substrate: which is set as UVCR (1.35 RIU) or quartz (1.5 RIU). We evaluate the reflectance and transmittance response at the upper, lower, and middle points of the operational range of bulk index of refraction (**Figure 4-18**).

First, the upper and lower limit of the two devices' operational range is determined. This is defined as the highest and the lowest bulk refractive index for which a detectable peak is present. It is determined that for both sensors the bulk refractive index upper limit is 1.46 RIU and the lower limit is 1.34 RIU. Beyond these limits the transmission peaks are not easily detectable via simulation, and thus would likely be undetectable in experiment.

Next, the efficiency is evaluated for the Rayleigh transmission peak at bulk refractive index (n_{bulk}) values of 1.34 RIU, 1.4 RIU, and 1.46 RIU (**Figure 4-18**). It is found that the device with UVCR substrate yields a peak transmittance greater than or equal to the device with quartz substrate. The UVCR substrate device transmittance at n_{bulk}=1.34, 1.4 and 1.46 RIU are 0.38, 0.51, and 0.35, respectively (**Figure 4-18**b, d, and f, respectively). The quartz substrate device transmittance at n_{bulk}=1.34, 1.4 and 1.46 RIU are 0.31, 0.46, and 0.35, respectively (**Figure 4-18**a, c, and e, respectively). This results in the UVCR substrate device having transmittances at n_{bulk}=1.34, 1.4, 1.46 RIU that are 22%, 11% and 0% greater, respectively. While the operation range of both sensors is the same, the transmittance of the UVCR substrate device outperforms that of the quartz substrate device.

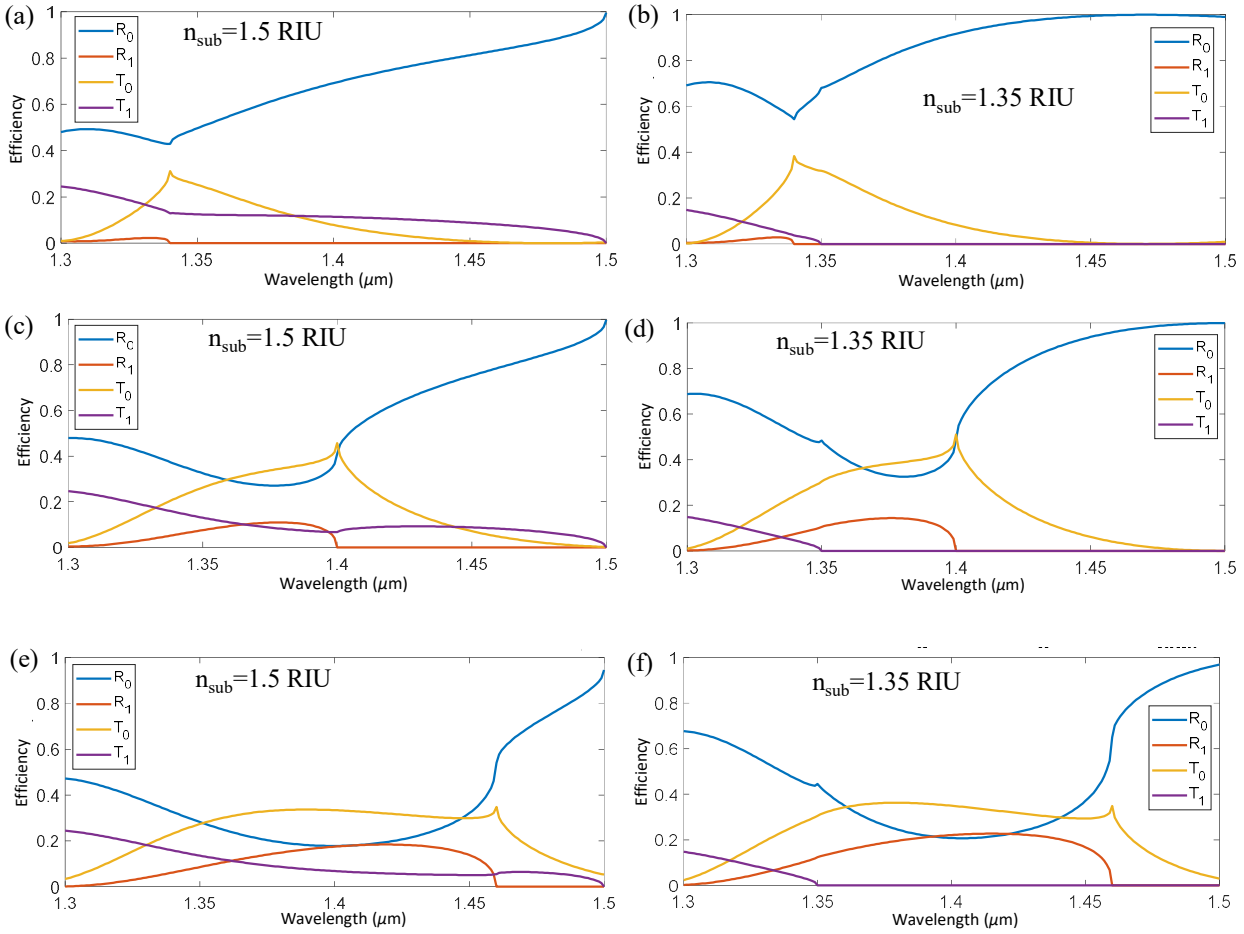

Figure 4-18 The device response from the sensor in **Figure 4-6** with varied substrate. The quartz substrate is evaluated at bulk indexes of refraction of (a) 1.34 RIU, (c) 1.4 RIU, and (e) 1.46 RIU. The UVCR substrate is evaluated at bulk indexes of refraction of (b) 1.34 RIU, (d) 1.4 RIU, and (f) 1.46 RIU. In each graph the zero and first-order reflectance is shown with a blue line and orange line, respectively. The zero and-first order transmittance is shown with a gold line and purple line, respectively.

The primary advantage of UV curable resin (UVCR) is that these materials are dielectrics that can have an index of refraction much lower than quartz. Lowering the index of refraction of the substrate of our device will lower the Rayleigh wavelength of the substrate. Above this

substrate Rayleigh wavelength, higher order (>0) transmitted light goes to zero transmittance; this is important because less energy in the higher order transmitted waves translates into more energy for the zero-order transmitted wave.

To fabricate the superiorly performing UVCR substrate device, a flat layer of resin must be attached to silicon. This interface must be absent of defects to prevent the scattering incident light. UVCR is difficult to work with and not feasible with current methods of production. Contrastingly, silicon on quartz (SOQ) is readily available and easy to fabricate into a device. Although the efficiency of the SOQ device is below that of the UVCR substrate device, the low barriers of production for the SOQ device currently make it the preferred choice.

4.5.3 Rayleigh sensor explanation

At the Rayleigh wavelength, corresponding to the bulk refractive index, the first-order reflection is completely extinguished for the spectrum investigated with the sensor in **Figure 4-6**; this is also true for the other sensors in this chapter. The refractive index of the sensor's substrate correlates with the wavelength at which the first-order transmission is completely extinguished: this also is true for all the sensors shown in this chapter. We show that a Rayleigh transmission peak (associated with the bulk refractive index) can draw energy from the zero-order reflection (**Figure 4-18**a and b), and the first-order transmission (**Figure 4-18**a, c, and e). In all devices in this chapter, the first-order reflection goes to 0 at the Rayleigh wavelength produced by the bulk index of refraction; this loss of energy frees up energy for the zero-order transmission peak (Rayleigh anomaly transmission peak). In addition, we show in the section Coupling orders that neighboring guided-mode resonance(s) shape the spectrum allowing the Rayleigh anomaly to produce a high transmittance peak.

4.6 Conclusion

The Rayleigh anomaly can be utilized when assisted by neighboring guided-mode resonance(s) to produce a transmission peak that shifts as the bulk index of refraction changes. The resulting guided-mode resonance-assisted Rayleigh sensor has a high sensitivity that is equal to the period (S_{Bulk}=period/RIU) of the GMR device. Past work using the Rayleigh anomaly with GMR and SPR devices have more complex structures, and/or they have sensitivities lower than the device period per RIU.

In this work we show how to evaluate the spectrum of proposed materials (SOQ) for use as a GMR-assisted Rayleigh sensor to optimize the value of fill factor, grating thickness, and waveguide thickness. We also show that there are multiple devices that can be developed with a given set of materials. Periodic devices with non-zero transmissivity extending into the desired operational wavelength range (derived from the operational bulk index of refraction range) exhibit the best sensor performance.

The GMR-assisted Rayleigh transmission peak wavelength corresponds to the dying off R_1, a possible dip in R_0, and – in cases of high substrate index – a small dip in T_1. It is also shown that at the Rayleigh peak wavelength, the evanescent coupling order associated with the T_0 peak is due to a neighboring GMR.

Chapter 5

Silicon-enhanced GMR sensors

5.1 Introduction

In this chapter we choose GMR sensors used in past work from our research group and others, and we use silicon to increase the bulk sensitivity of the sensors by altering the field distribution within the GMR sensors.

5.1.1 Multiparametric GMR sensor

The sensor presented here is from our previous work on multiparametric biosensors [84]. The period (Λ) is 500 nm, the fill factor (ff) is 0.42, the grating height (d_g) is 260 nm, and the waveguide height (d_h) is 500 nm (**Figure 5-1**). The grating and waveguide are silicon nitride with an index of 1.8 RIU, the substrate is quartz with an index of 1.52 RIU, and the bulk medium in the input region has an index from 1.33 RIU to 1.43 RIU. This sensor was designed to be easily fabricable with the goal of having multiple resonant peaks in the near IR spectrum. The multiple peaks were then used in an inversion algorithm to take three resonant wavelength shifts as input, and yield biolayer index of refraction, biolayer thickness, and bulk index of refraction as output.

The strengths of this GMR sensor are the multiple peaks in the sensor reflection response that are used to measure shifts in multiple sensor variables. Another strength is the distinct position of each resonance peak: this allowed the implementation of this sensor without using a polarizer [84]. A weakness of this sensor is the low sensitivity that the resonant peaks have with respect to bulk and biolayer value shifts: this is deleterious to the limit of detection of the device. Another weakness of this device is the similar sensitivity value for some of the resonant modes: this complicates the inversion process.

The bulk sensitivity of a GMR sensor is calculated by with the following equation.

$$S = \frac{\Delta\lambda}{\Delta n_{Bulk}} \tag{5.1}$$

where S is the sensitivity, $\Delta\lambda$ is the change in resonant wavelength, and Δn_{Bulk} is the change in bulk index of refraction. In short, the more the resonance wavelength shifts for a fixed amount of change in bulk index of refraction, the greater the sensitivity. The TM reflection spectrum is shown in **Figure 5-1**. The TM_1 bulk sensitivity is 78.8 nm/RIU, and the TM_0 bulk sensitivity is 28.5 nm/RIU (**Figure 5-1**).

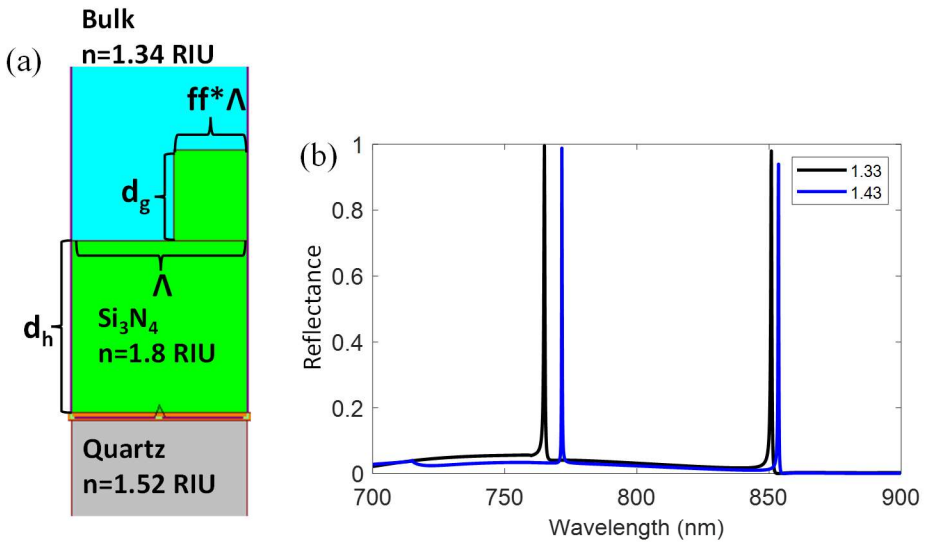

(c)

Bulk Index (RIU)	TM_1 Peak Wavelength (nm)	TM_1 Sensitivity (nm/RIU)
1.33	765	-
1.43	771.6	66

(d)

Bulk Index (RIU)	TM_0 Peak Wavelength (nm)	TM_0 Sensitivity (nm/RIU)
1.33	850.9	-
1.43	853.6	27

Figure 5-1 Multiparametric sensor TM sensitivity. (a) Schematic of the multiparametric sensor: silicon nitride (Si_3N_4) grating and homogeneous layer on a quartz substrate. The orange horizontal line at the substrate/homogeneous layer interface represents a light source directed upward. The grating parameters are as follows: fill factor (ff) = 0.42, grating depth (d_g) = 260 nm, homogeneous layer depth (d_h) = 500 nm, and period (Λ) = 500 nm. (b) The device from (a) RCWA simulated zero-order TM reflection spectrum at a bulk index of refraction 1.33 RIU (black) and 1.43 RIU (blue). (c) TM_1 bulk index sensitivity. (d) TM_0 bulk index sensitivity.

The TE reflection spectrum is shown in **Figure 5-2**. The TE_1 bulk sensitivity is 69 nm/RIU, and the TE_0 bulk sensitivity is 18 nm/RIU (**Figure 5-2**).

(a)

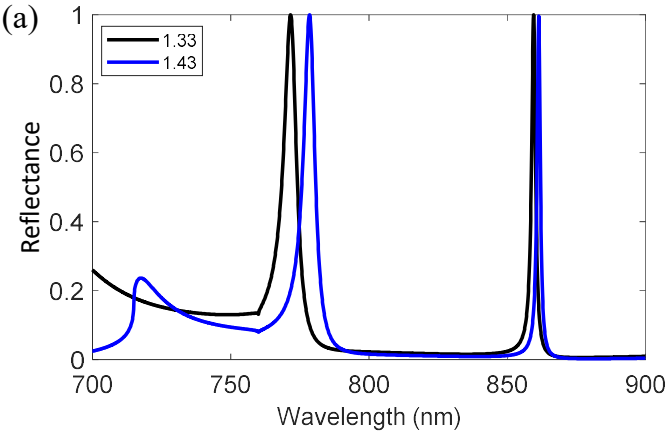

(b)

Bulk Index (RIU)	TE_1 Peak Wavelength (nm)	TE_1 Sensitivity (nm/RIU)
1.33	771.6	-
1.43	778.5	69

(c)

Bulk Index (RIU)	TE_0 Peak Wavelength (nm)	TE_0 Sensitivity (nm/RIU)
1.33	859.5	-
1.43	861.3	18

Figure 5-2 Multiparametric sensor TE sensitivity. (a) The device from **Figure 5-1**a RCWA simulated zero-order TE reflection spectrum at a bulk index of refraction 1.33 RIU (black) and 1.43 RIU (blue). (b) TE_1 bulk index sensitivity. (c) TE_0 bulk index sensitivity.

5.1.2 Silicon-incorporated multiparametric sensor

The bulk sensitivity of the TM_1 mode in the unaltered structure is 66 nm/RIU. The resonant wavelength shift for the TM_1 mode is shown in the above figure. In an effort to increase the bulk index of refraction sensitivity of the device, we add a thin layer of silicon (Si) to the top of the GMR grating (**Figure 5-3**). We choose a thin layer of silicon to limit absorption at the resonant wavelength ensuring the response has optimal reflectivity at the peak wavelengths. As show in **Figure 5-4**, the addition of the Si layer on the GMR device causes the TM_1 resonant wavelength to have a greater resonant wavelength shift as the bulk index of refraction shifts. This clearly shows that Si enhances the sensitivity of the GMR sensor for the TM_1 mode. The device TM_1 bulk RIU sensitivity with and without the 20 nm Si layer on the grating pillar is ~80.8 nm/RIU

and 66 nm/RIU, respectively. This translates into a ~22% increase in bulk RIU sensitivity with the addition of Si.

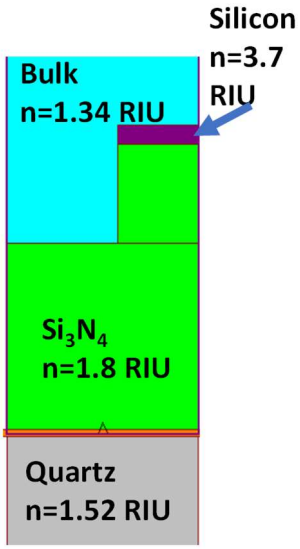

Figure 5-3 Multiparametric sensor schematic implementing the GMR sensor in **Figure 5-1**a with a thin layer of silicon on top of the grating.

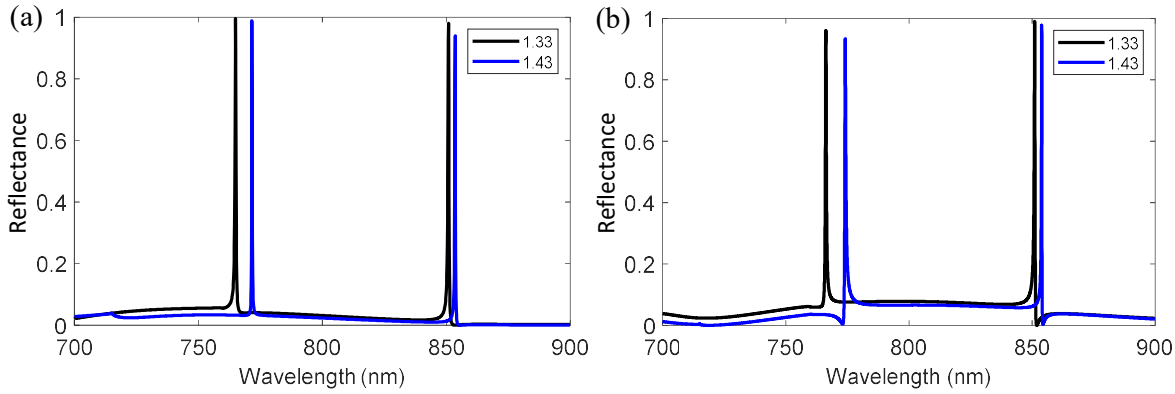

(c)

Si Thickness	TM_1 Sensitivity (nm/RIU)	TM_0 Sensitivity (nm/RIU)
0	66.0	27.0
10	73.9	28.1
20	80.8	28.9

Figure 5-4 Silicon-enhanced multiparametric sensor TM data. (a) The device from **Figure 5-3** RCWA simulated zero-order TM reflection spectrum at a bulk index of refraction 1.33 RIU (black) and 1.43 RIU (blue). (b) The device from **Figure 5-3** with a 20 nm layer of silicon TM reflection spectrum at a bulk index of refraction 1.33 RIU (black) and 1.43 RIU (blue). (c) TM bulk index sensitivity with a silicon layer of thickness 0 nm, 10 nm, and 20 nm.

The TM_0 mode only shows a modest improvement in sensitivity (from 27.9 nm/RIU to 28.9 nm/RIU) with the added 20 nm Si on top of the GMR grating (3.5% increase). However, there is not a decrease in the sensitivity of the TM_0 mode, so this device is still viable for its original application and improved compared to its original state.

The bulk sensitivities of the TE_1 and TE_0 modes with an unaltered structure is 70.0 nm/RIU and 18.8 nm/RIU, respectively. The resonant wavelength shifts are shown in **Figure 5-5**a. For the TE polarization, the addition of a thin Si layer on top of the GMR grating pillar produces a very significant increase in sensitivity.

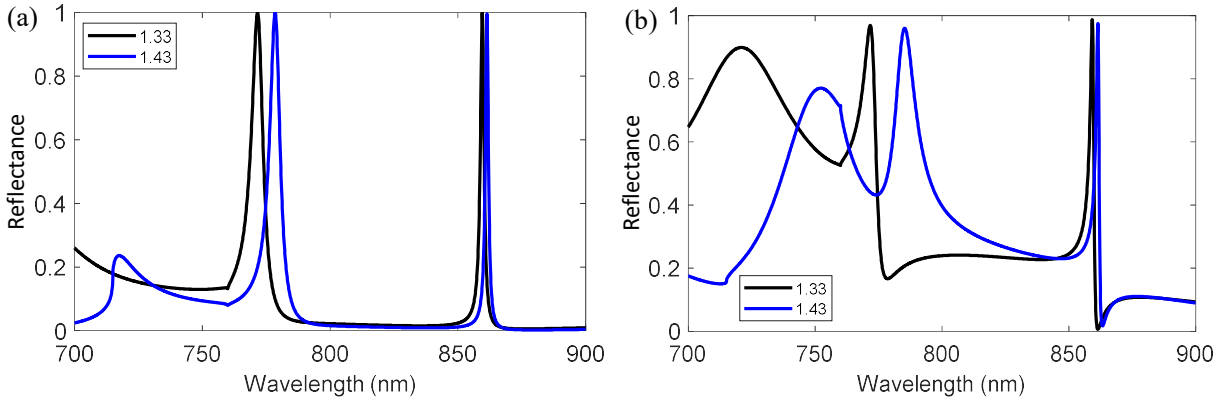

(c)

Si Thickness	TE_2 Sensitivity (nm/RIU)	TE_1 Sensitivity (nm/RIU)	TE_0 Sensitivity (nm/RIU)
0	-	70.0	18.8
10	-	90.8	20.3
20	320.0	138.4	22.7

Figure 5-5 Silicon-enhanced multiparametric sensor TE data. (a) The device from **Figure 5-1**a RCWA simulated zero-order TE reflection spectrum at a bulk index of refraction 1.33 RIU (black) and 1.43 RIU (blue). (b) The device from **Figure 5-1**a with a 20 nm layer of silicon TE reflection spectrum at a bulk index of refraction 1.33 RIU (black) and 1.43 RIU (blue). (c) TE bulk index sensitivity with a silicon layer of thickness 0 nm, 10 nm, and 20 nm.

Most notably, an additional resonant mode (TE_2) signature is present in the reflection response due to the increased index of the effective medium of the grating (**Figure 5-5**b). This additional mode signature can be seen without the Si layer in **Figure 5-5**a at n_{Bulk}=1.43 RIU; however, for the TE_2 mode to achieve a high reflectivity, the index of the high index grating pillar must increase. The bulk RIU sensitivity of the TE_2 mode is 320.0 nm/RIU. This sensitivity is ~4.6 times greater than the unaltered device's most sensitive modes (TM_1 and TE_1).

The addition of the Si layer increases the resonance wavelength shift for the TE_1 mode as can be seen in the **Figure 5-5**b and c. It can also be seen that the TE_1 resonance peak broadens.

This broadening is due to the increased index contrast in the lattice. The addition of a 20 nm Si layer improves the TE_1 sensitivity from 70.0 nm/RIU to 138.4 nm/RIU. This translates to a 98% improvement in bulk RIU sensitivity for the TE_1 mode. The TE_0 mode also has improvement in bulk RIU sensitivity (18.8 nm/RIU to 22.7 nm/RIU) with the addition of a 20 nm Si layer on the grating pillar. Although this 21% improvement is not as significant as the TE_1 mode, the sensitivity is increased, and this improves the viability of this sensor.

The addition of a thin silicon layer on the grating high index pillar increases the sensitivity of all resonant modes – especially the TE_1 mode in this example– and gives rise to the extremely sensitive TE_2 resonant mode. Even though there is significant broadening associated with the mode in the short-wavelength band, it is still detectable in spectral measurements and thus potentially useful.

5.1.3 Silicon-incorporated high-Q sensor

The GMR device example presented next is a high Q (small FWHM) bulk index of refraction sensor. The device has a period (Λ) of 500 nm, a fill factor (ff) of 0.41, a grating height (d_g) of 30 nm, and a waveguide height (d_h)of 150 nm (**Figure 5-6**) [85]. The grating of this device is silicon oxide and has an index of 1.46 RIU, the waveguide is silicon nitride and has an index of 2.00 RIU, the substrate is quartz and has an index of 1.48 RIU, and the bulk media can have an index from 1.33 RIU to 1.43 RIU. The design of this GMR sensor is rooted in optimizing the quality factor of the resonant peak, having a bulk RIU sensitivity, achieving a high signal to noise ratio, and achieving a superior limit of detection. These attributes were demonstrated in the work by detecting bovine serum albumin (BSA) at a concentration of 1 ng/ml [85].

(a)

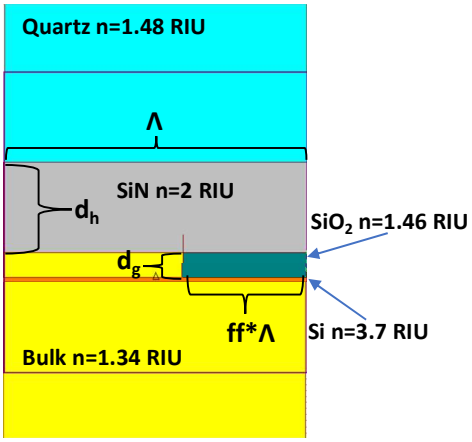

(b)

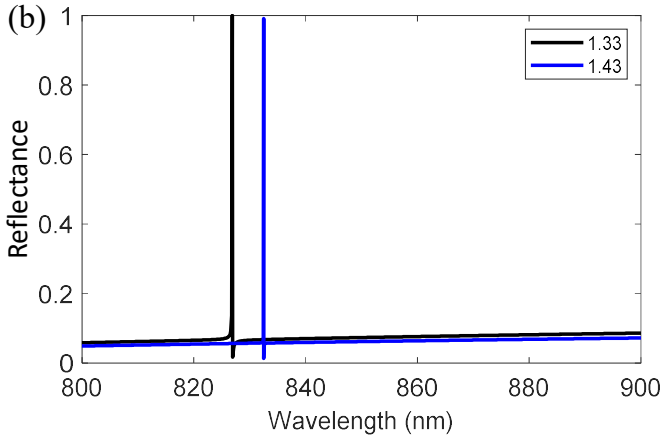

(c)

Bulk Index (RIU)	TE Peak Wavelength (nm)	TE Sensitivity (nm/RIU)
1.33	826.9	-
1.43	832.5	56.2

Figure 5-6 High-Q sensor. (a) Schematic of the high-Q sensor: silicon oxide (SiO_2) grating, silicon nitride (SiN) homogeneous layer on a quartz substrate. The orange horizontal line at the substrate/homogeneous layer interface represents a light source directed upward. The grating parameters are as follows: fill factor (ff) = 0.41, grating depth (d_g) = 30 nm, homogeneous layer depth (d_h) = 150 nm, and period (Λ) = 500 nm. (b) The device from (a) RCWA simulated zero-order TE reflection spectrum at a bulk index of refraction 1.33 RIU (black) and 1.43 RIU (blue). (c) TM bulk index sensitivity.

The strengths of this device are the high Q factor, superior limit of detection, and the ~100% reflectivity of the resonant peak. The weaknesses of this device are the single resonant peak in the spectrum of interest: this prevents multiparametric detection.

The sensor high Q reflection sensor has a single peak in the spectrum of interest in the TE mode. The bulk RIU sensitivity of the unaltered high Q reflection sensor is 57.0 nm/RIU. The resonant shift is shown above.

The addition of a Si layer on the grating pillar increases the resonant wavelength shift produced by the sensor as the bulk index of refraction shifts (**Figure 5-7**) The sensitivities of the GMR device in **Figure 5-6**a with a 20 nm Si layer and with no Si layer are 83.7 nm/RIU and 57.0 nm/RIU, respectively. This translates into a 47% increase in bulk RIU sensitivity with the addition of a 20 nm layer of silicon.

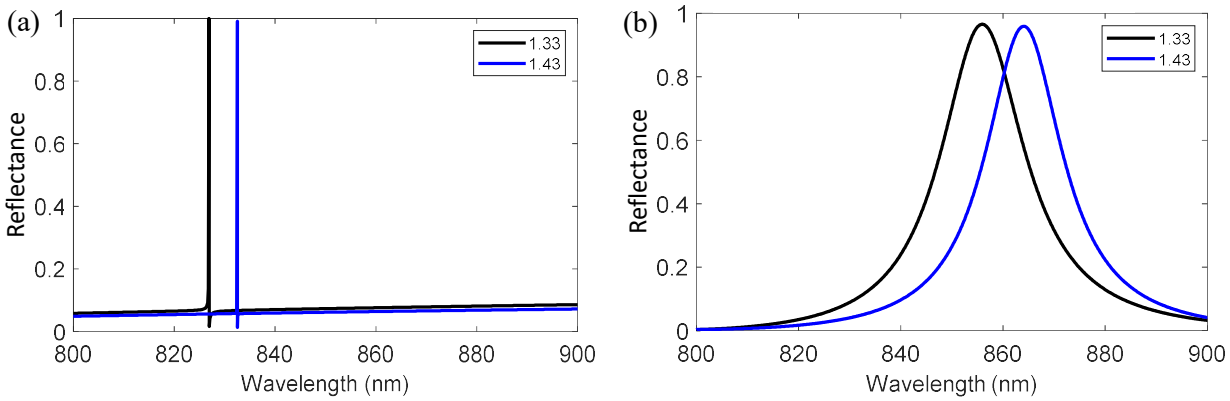

(c)

Si Thickness (nm)	TE Sensitivity (nm/RIU)
0.0	57.0
6.7	65.2
13.3	74.0
20.0	83.7

Figure 5-7 Silicon-enhanced high-Q sensor performance. (a) The device from **Figure 5-6**a RCWA simulated zero-order TE reflection spectrum at a bulk index of refraction 1.33 RIU (black) and 1.43 RIU (blue). (b) The device from **Figure 5-6**a with a 20 nm layer of silicon TE reflection spectrum at a bulk index of refraction 1.33 RIU (black) and 1.43 RIU (blue). (c) TE bulk index sensitivity with a silicon layer of thickness 0 nm, 6.67 nm, 13.3 nm, and 20 nm.

5.1.4 Si-incorporated fiber-faceted-integrated sensor

The final GMR sensor presented here is designed to perform as a compact fiber mounted bulk refraction index sensor [86]. This GMR sensor has a period (Λ) of 1030 nm, a fill factor (ff)

of 0.77, a grating height (d_g) of 200 nm, and a waveguide height (d_h) of 150 nm (**Figure 5-8**a). The grating and waveguide are silicon nitride (Si_3N_4) with an index of 1.9 RIU, the substrate is a multimode optical fiber core with an index of 1.45 RIU, and the bulk media can have an index of 1.33 RIU to 1.43 RIU. This device was designed for simplicity of fabrication because the waveguide and grating are deposited and patterned on the end of a fiber optic cable.

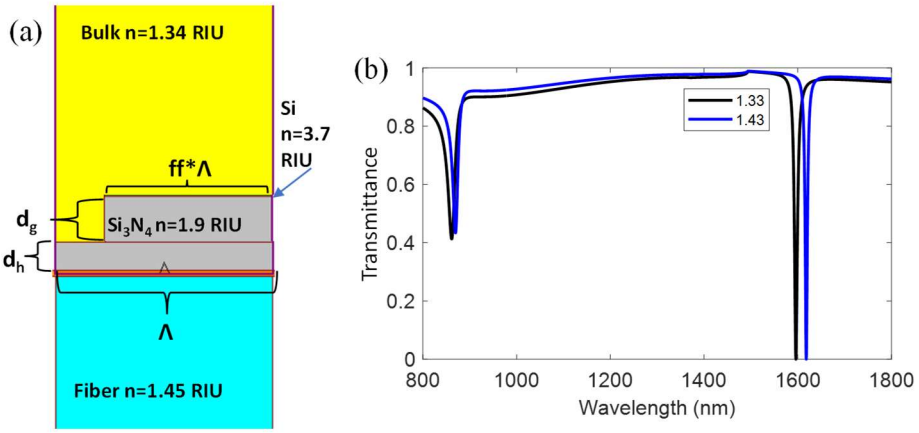

(c)

Bulk Index (RIU)	TE_1 Peak Wavelength (nm)	TE_1 Sensitivity (nm/RIU)
1.33	879.4	-
1.43	893.8	144.0

(d)

Bulk Index (RIU)	TE_0 Peak Wavelength (nm)	TE_0 Sensitivity (nm/RIU)
1.33	1633.4	-
1.43	1659.9	265.0

Figure 5-8 Fiber-faceted-integrated (FFI) sensor TE spectrum and sensitivity. (a) Schematic of the fiber-faceted-integrated sensor: silicon nitride (Si_3N_4) grating and homogeneous layer, and an optical fiber core substrate. The orange horizontal line at the substrate/homogeneous layer interface represents a light source directed upward. The grating parameters are as follows: fill factor (ff) = 0.77, grating depth (d_g) = 200 nm, homogeneous layer depth (d_h) = 150 nm, and period (Λ) = 1030 nm. (b) The device from (a) RCWA simulated zero-order TE reflection spectrum. (c) TE_1 bulk index sensitivity. (d) TE_0 bulk index sensitivity.

The strengths of this device include its compact size enabling easy implementation of bulk sensing with this GMR sensor. Another strength of this device is the dual resonance peaks that can be used to monitor two sensor variables simultaneously. This device has ordinary sensitivity. The TE_1 mode of this device has a moderate change in transmissivity from the passband to the stopband: this may produce a low signal to noise ratio in practice.

The fiber-faceted-integrated (FFI) sensor has two resonant modes of interest in the TE polarization **Figure 5-8**b. The TE_1 mode of the unaltered sensor has a bulk index of refraction sensitivity of 82.2 nm/RIU. The resonance shift can be seen above as a dip at the lower wavelength. Qualitatively, the magnitude of the bulk sensitivity of the TE_1 mode is moderate. The TE_0 resonant mode of the unaltered fiber-faceted-sensor has a bulk index of refraction sensitivity of 224 nm/RIU.

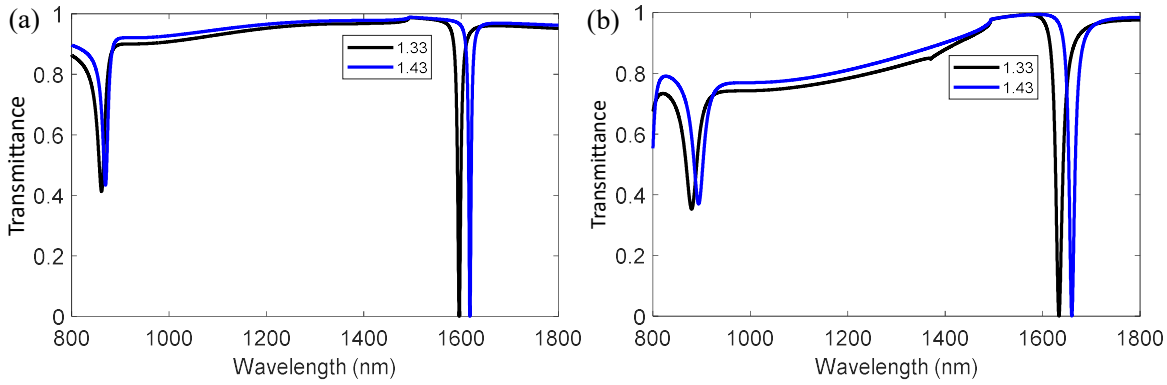

(c)

Si Thickness (nm)	TE_1 Sensitivity (nm/RIU)	TE_0 Sensitivity (nm/RIU)
0.00	82.2	224.4
6.67	98.9	242.2
13.33	121.1	258.9
20.00	150.0	274.4

Figure 5-9 Silicon-enhanced fiber-faceted-integrated (FFI) sensor performance. (a) The device from **Figure 5-8**a RCWA simulated zero-order TE-polarization transmission spectrum at a bulk index of refraction 1.33 RIU (black) and 1.43 RIU (blue). (b) The device from **Figure 5-8**a with a 20 nm layer of silicon TE reflection spectrum at a bulk index of refraction 1.33 RIU (black) and 1.43 RIU (blue). (c) TE bulk index sensitivity with a silicon layer of thickness 0 nm, 6.67 nm, 13.33 nm, and 20 nm.

The addition of a Si layer on top of the grating pillar is shown to increase the dip wavelength shift of the TE_1 mode as the bulk RIU shifts (**Figure 5-9**b). The difference between the transmission dip (stop band) and the transmission passband decreases with the addition of the Si layer, but this change is minute. The TE_1 bulk RIU sensitivity of the GMR device in **Figure 5-8**a with a 20nm Si layer on top of the grating and with no additional layer is 150.0 nm/RIU and 82.2 nm/RIU, respectively. This translates into an 82% increase in bulk RIU sensitivity.

The addition of a Si layer on top of the grating pillar increases the dip wavelength shift of the TE_0 mode as the bulk RIU shifts (**Figure 5-9**b). With the addition of the Si layer, the depth of the transmission stop band is maintained. The FWHM increases to a small extent. The TE_0 bulk RIU sensitivity of the device in the **Figure 5-8**a with a 20nm Si layer on top of the grating and with no additional layer is 274.4 nm/RIU and 224.4 nm/RIU, respectively. This translates into a 22% increase in bulk RIU sensitivity.

5.1.5 Silicon-incorporated sensor fabrication

The inclusion of silicon on the GMR grating can be achieved by depositing silicon, of the desired thickness, on the unetched grating material. Next, photoresist is deposited on the silicon, the photoresist is patterned, and the device surface is etched. RIE (reactive ion etching) can be used to etch the silicon layer and the grating material to achieve the desired grating depth and fill-factor. This is a simple strategy to fabricate a silicon-incorporated GMR sensor.

5.2 Sensor EM field distribution

5.2.1 Multiparametric sensor EM field distribution

We now analyze the EM field distribution of the unaltered multiparametric GMR sensor from section 5.1.1 at the resonant wavelengths. This is done to determine if an altered field distribution is the cause of increased sensitivity with the addition of a silicon layer. All field analysis is done with at a bulk index value of 1.34 RIU. The TM_1 resonance of the unaltered multiparametric sensor is evaluated at 766 nm: at this wavelength, the sensor has some of its resonant electromagnetic (EM) field concentrated in the low index part of the diffraction grating. The low index portion of the grating consists of the bulk media (**Figure 5-10**a). Thus, changes in the bulk media refractive index affect this portion of the EM field and cause the resonant wavelength to shift. The EM field concentration for the multiparametric sensor with a 20 nm Si

layer is also analyzed at the TM_1 resonant wavelength (768 nm). There is a qualitatively small increase in the EM field concentration in the bulk of the sensor with the of 20 nm of Si layer – as can be seen in **Figure 5-10**a and b. Although slight, the change in field distribution occurs because the high index of the Si layer moves fields of the TM_1 resonant mode toward the bulk media portion of the device. The EM fields are the areas of energy concentration of the evanescent waves that leak out of the device to form a resonant feature in the spectrum. Therefore, the more energy is moved towards the bulk of the device the more sensitive the resonant modes will be to a change in bulk RIU.

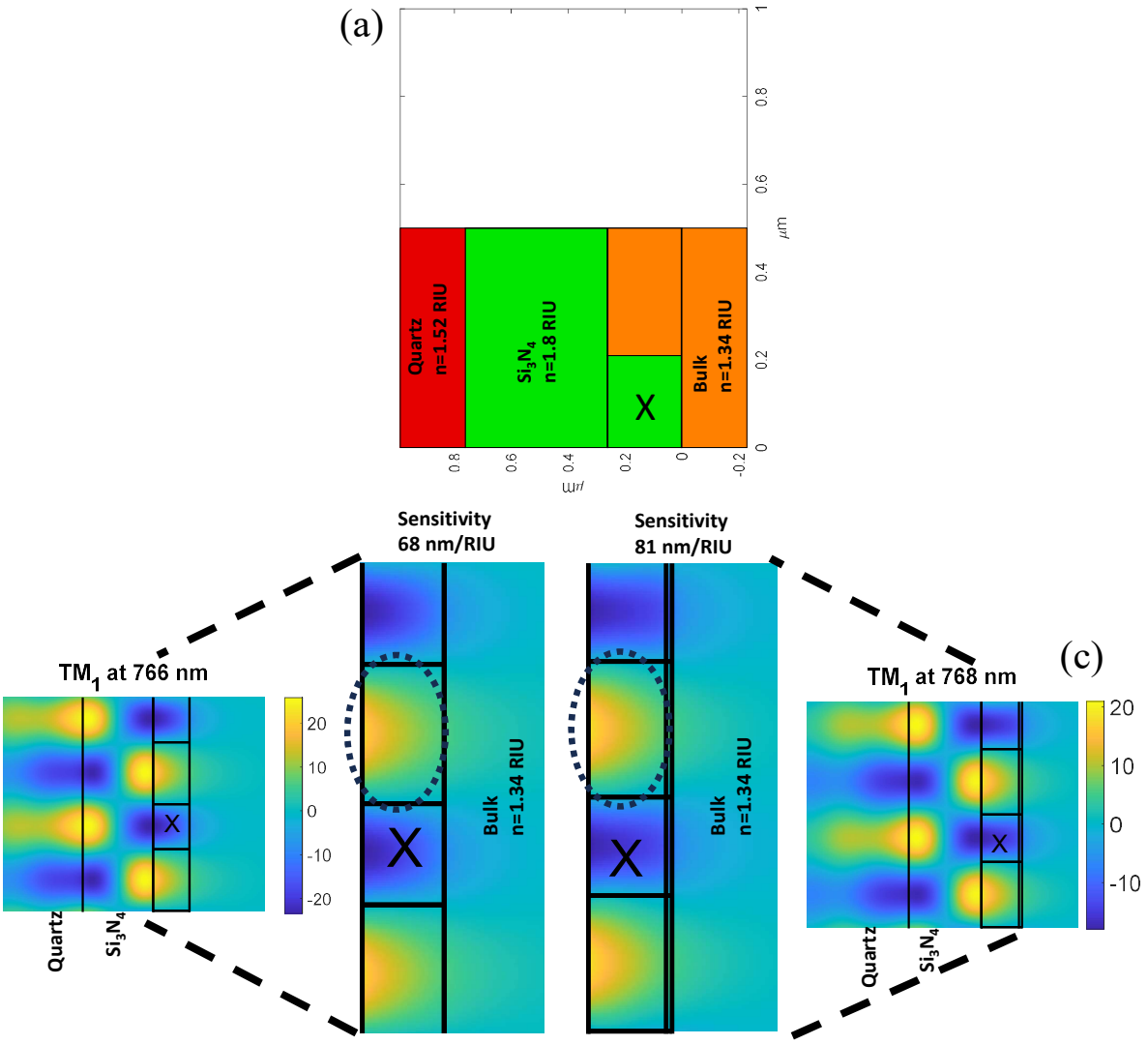

Figure 5-10 Multiparametric sensor TM_1 fields. (a) Schematic of the multiparametric sensor from **Figure 5-1**a. (b) EM field distribution at the TM_1 resonant wavelength (766 nm). (c) EM field distribution, of the sensor with and silicon layer added, at the TM_1 resonant wavelength (768 nm). The X corresponds to the high index portion of the grating. The enlarged portion of the figure is the grating and bulk. The dotted oval is the EM field in the low index portion of the grating (bulk): this is done to highlight a difference in field distribution between (b) and (c).

The multiparametric GMR sensor's small increase in bulk index sensitivity of the TM_0 resonance (27.3 nm/RIU to 28.9 nm/RIU) translates into a lack of qualitative change in the EM field distribution for this resonant wavelength. Thus, field distribution is not pictured.

The TE_2 resonant mode does not produce a reflection peak for the unaltered multiparametric GMR sensor; thus, it can not be displayed. However, the addition of a 20 nm layer of Si to the multiparametric GMR sensor generates the TE_2 mode resonance peak. The distribution of the EM fields for the TE_2 resonant mode is primarily in the low index portion of the grating: the bulk. Also, the fields concentrated in the high index portion of the grating have nearly half of their area the bulk region of the schematic (**Figure 5-11**b): this is due to the field confinement in the high index silicon layer of the sensor. The presence of fields in the bulk media results in a very high sensitivity to shifts in bulk RIU. The TE_2 mode is the most sensitive resonant mode for this sensor, and this is qualitatively evident by the EM field distribution.

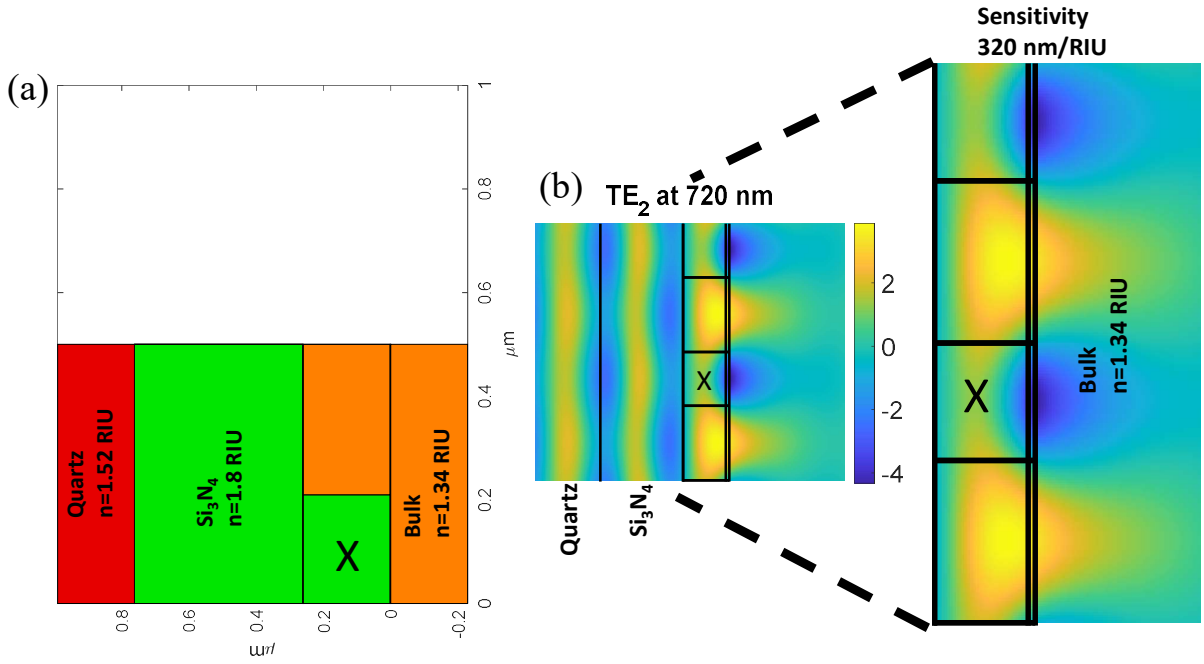

Figure 5-11 Multiparametric sensor TE_2 fields. (a) Schematic of the multiparametric sensor from **Figure 5-1**a. (b) EM field distribution, of the sensor with a silicon layer, at the TM_2 resonant wavelength (720 nm). The X corresponds to the high index portion of the grating. The enlarged portion of the figure is the grating and bulk.

The EM field distribution of the TE_1 resonant mode for the unaltered multiparametric sensor is primarily located in the substrate, waveguide, and high index grating of the sensor. However, there is a locus of energy that has about half of its area in the waveguide and half in the bulk (**Figure 5-12**b). With the addition of the 20 nm Si layer, the locus of energy that was halfway in the waveguide migrates farther into the bulk, specifically a significant majority of this field locus is in the bulk. Due to the Si addition, there is also a greater field concentration at the boundary of the grating pillar and the bulk media. This migration of fields towards the bulk media is quantitatively evident by the increased bulk RIU sensitivity of the device for the TE_1 mode (70 nm/RIU to 138 nm/RIU).

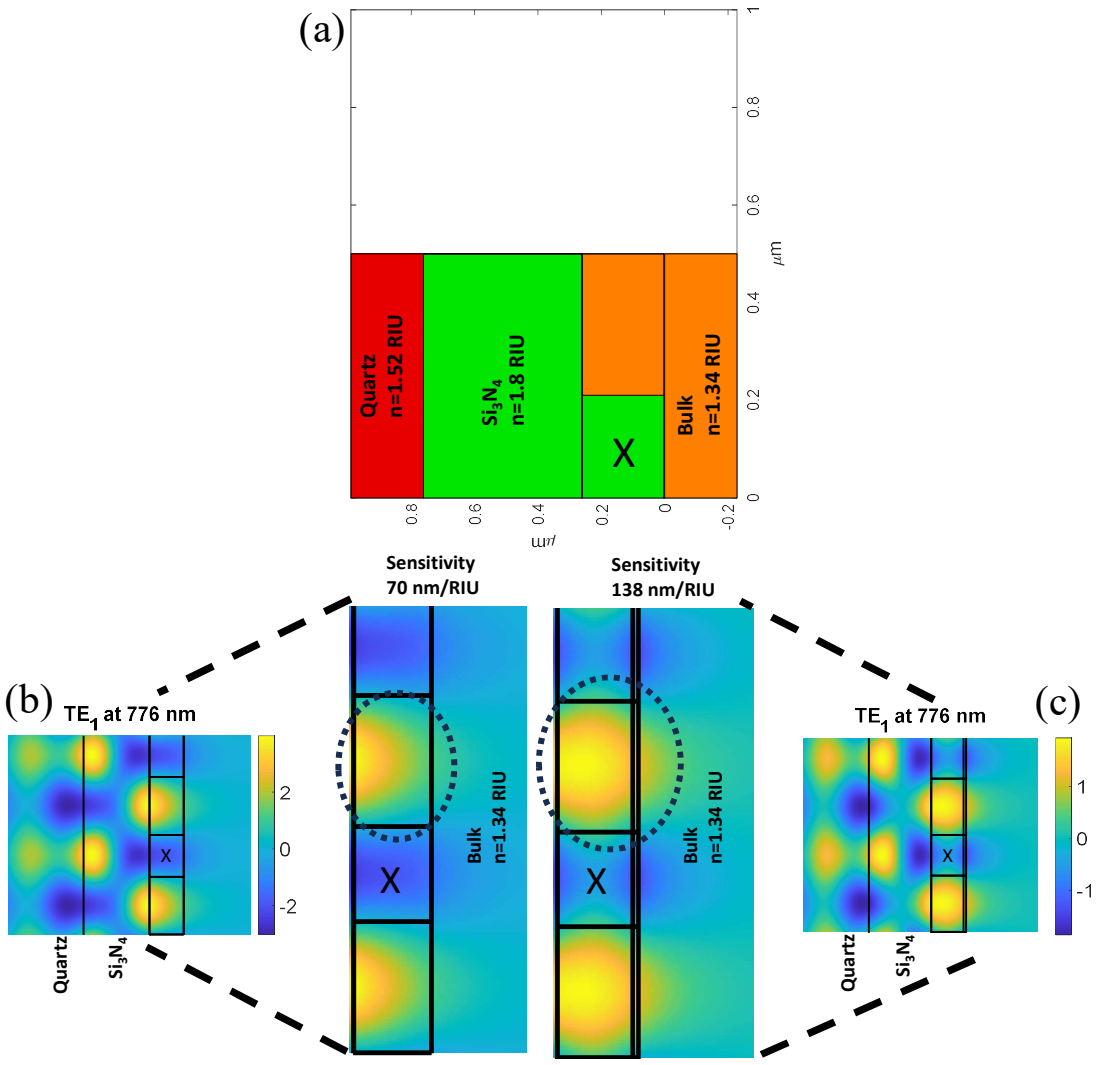

Figure 5-12 Multiparametric sensor TE_1 fields. (a) Schematic of the multiparametric sensor from **Figure 5-1**a. (b) EM field distribution at the TE_1 resonant wavelength (776 nm). (c) EM field distribution, of the sensor with and silicon layer added, at the TE_1 resonant wavelength (776 nm). The X corresponds to the high index portion of the grating. The enlarged portion of the figure is the grating and bulk. The dotted oval is the EM field in the low index portion of the grating (bulk): this is done to highlight a difference in field distribution between (b) and (c).

The multiparametric GMR sensor has a small increase in TE_0 bulk index sensitivity with the addition of a silicon layer (19 nm/RIU to 23 nm/RIU) and thus a small change in EM field distribution. Thus, field distribution for this mode is not pictured.

5.2.2 High-Q sensor EM field distribution

The EM field distribution for the resonant TE mode for the unaltered high-Q sensor, from section 5.1.3, is located primarily in the waveguide **Figure 5-13**c. The resonant mode evanescent tail hangs into the bulk, but the field strength dissipates significantly as the distance into to bulk increases. The addition of the 20 nm Si layer changes the field distribution to be much further into the bulk media (**Figure 5-13**b). Therefore, there is an increase in the bulk index sensitivity of the resonant TE mode.

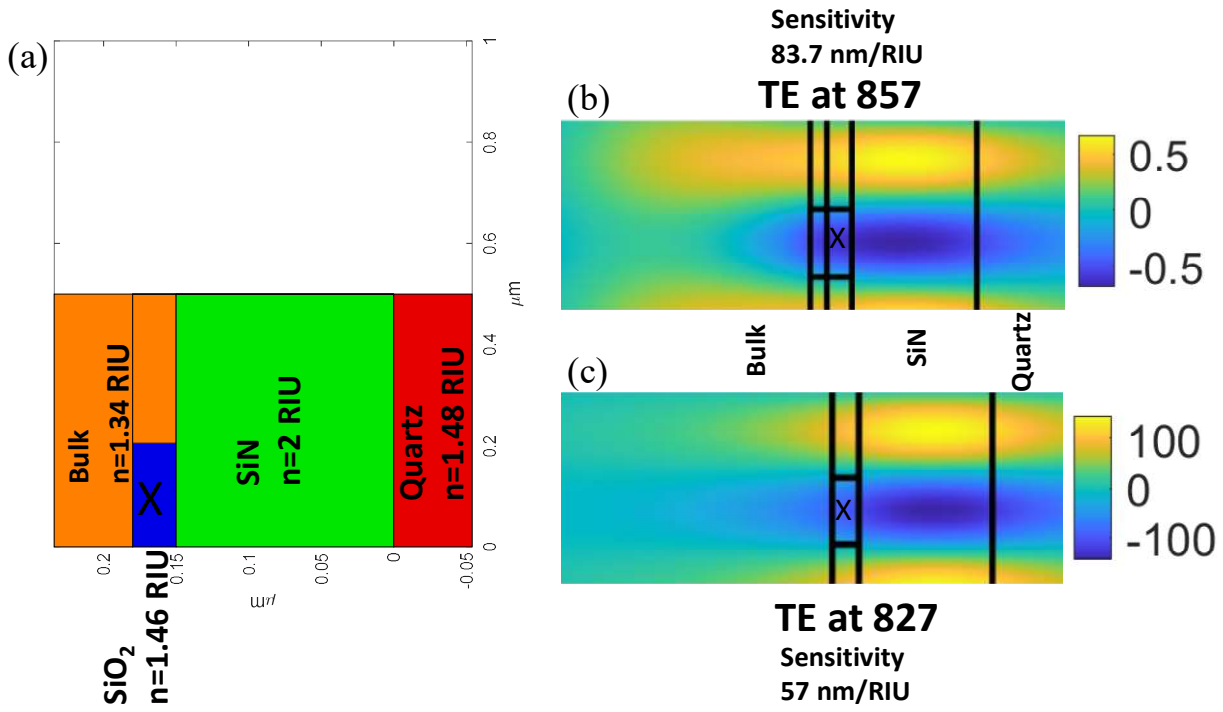

Figure 5-13 High-Q sensor TE fields. (a) Schematic of the high-Q sensor from **Figure 5-6**a. (b) EM field distribution, of the sensor in (a) with and silicon layer added, at the TE resonant wavelength (857 nm). (c) EM field distribution, of the sensor in (a), at the TE resonant wavelength (827 nm). The X corresponds to the high index portion of the grating.

4.3.3 Fiber-facet-integrated sensor EM field distribution

The TE_1 mode EM field distribution for the unaltered fiber-faceted-integrated (FFI) sensor is primarily located in the high index portion of the grating and the waveguide **Figure 5-14**c. There is an oval shaped locus of EM energy that is in the waveguide and the low index portion of the grating – the bulk media. The 20 nm layer of Si causes the oval shaped locus of energy, that had energy in the waveguide and bulk, to move further into the bulk media (**Figure 5-14**b). This increase in EM field distribution in the bulk media is the cause of the increased bulk index sensitivity of the TE_1 resonant mode (81 nm/RIU to 144 nm/RIU).

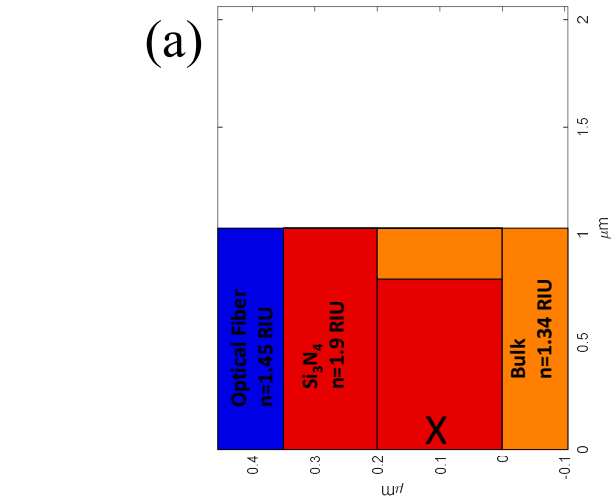
(a)
Optical Fiber
n=1.45 RIU
Si3N4
n=1.9 RIU
Bulk
n=1.34 RIU
X
μm
Sensitivity
150 nm/RIU
TE1 at 882
(b)
X
2
1
0
-1
Optical
Fiber
Si3N4
Bulk
(c)
X
1
0
-1
TE1 at 862
Sensitivity
82.2 nm/RIU

Figure 5-14 FFI sensor TE_1 fields. (a) Schematic of the fiber-faceted-integrated sensor from **Figure 5-6**a. (b) EM field distribution, of the sensor in (a) with and silicon layer added, at the TE_1 resonant wavelength (882 nm). (c) EM field distribution, of the sensor in (a), at the TE_1 resonant wavelength (862 nm). The X corresponds to the high index portion of the grating.

The increase in sensitivity for the TE_0 mode of the FFI sensor is due to an increase in EM field distribution in the bulk media of the sensor. The TE_0 bulk index sensitivity has a moderate increase with the added silicon layer (224.4 nm/RIU to 274.4 nm/RIU). The moderate bulk index sensitivity change with the presence of the Si layer translates into a moderate EM field change that is not visually significant. Thus, the field distribution for the TE_0 mode is not displayed.

The trend shown with all the sensors is that the high refractive index of silicon enhances the resonant mode confinement in the region of the silicon. The silicon is deposited on the boundary between the grating and the bulk media and this moves/confines the EM fields of the resonant modes closer to the bulk media compared to the sensors with no silicon layer. As a result of the increased resonant mode confinement in and/or near the bulk media, the resonant modes are more sensitive to changes in the refractive index of the bulk media. This causes an increased peak wavelength shift, for sensors with a ~20 nm silicon layer on the grating, as the index of refraction of the bulk media (often water or saline based) changes.

5.3 Conclusion

A thin layer of silicon on the grating of a GMR sensor is shown to increase the bulk index of refraction sensitivity. We demonstrate that the resultant silicon-enhanced sensors' bulk index sensitivity can increase up to ~98%. In this work we show by presenting selected example sensor embodiments that the addition of a thin layer of silicon can enhance the sensitivity of these GMR sensors.

The cause of the GMR sensors' increased bulk index sensitivity is the high refraction index of silicon. Applied to the sensors in a thin (~20 nm) layer, the silicon addition results in a region of high index and low absorption. The high refractive index region confines the fields of the resonant modes near the bulk media. Fields of resonant modes in or near the bulk media are more responsive to refractive index changes of the bulk media.

The inclusion of the Si layer can be executed by depositing Si on the grating material before a photoresist is deposited, patterned, and etched. The addition of Si is readily applicable to several sensors, and this serves as possible method to significantly increase bulk index of refraction sensitivity of GMR sensors.

Chapter 6

GMR enabled quantification of neuropeptide Y

6.1 Introduction

Assessing levels of neuropeptide Y (NPY) in the human body has many medical uses. Accordingly, we report the quantitative detection of NPY biomarkers applying guided-mode resonance (GMR) biosensor methodology. The label-free sensor operates in the near-infrared spectral region exhibiting distinctive resonance signatures. The interaction of NPY with bioselective molecules on the sensor surface causes spectral shifts that directly identify the binding event without additional processing. In the experiments described here, NPY antibodies are attached to the sensor surface to impart specificity during operation. For the low concentrations of NPY of interest, we apply a sandwich NPY assay in which the sensor-linked anti-NPY molecule binds with NPY that subsequently binds with anti-NPY to close the sandwich. The sandwich assay achieves a detection limit of ~0.1 pM NPY. The photonic sensor methodology applied here enables expeditious high-throughput data acquisition with high sensitivity and specificity. The entire bioreaction is recorded as a function of time, in contrast to label-based methods with single-point detection. The convenient methodology and results reported are significant, as the NPY detection range of 0.1–10 pM demonstrated is useful in important medical circumstances.

Nanopatterned dielectric films provide effective and economic platforms for a host of biological detection applications. The sensor basis is provided by photonic resonance effects originating in lateral leaky Bloch modes propagating along the film. Attendant surface-localized electromagnetic field features enable sensitive biolayer interrogation. Thus, the guided-mode resonance (GMR) sensor operates with quasi-guided waveguide modes induced in the film by

incident light [87] [2]. The useful resonance signatures are generated in one-dimensional (1D) or two-dimensional (2D) nanopatterns that can be fabricated in large arrays in a reliable, repeatable, and cost-effective manner using nanoimprint methods. Label-free GMR photonic sensors are immune to electromagnetic interference and permit effective light input and output, yielding compact architectures and effective sensing approaches. These sensors can be interrogated with unpolarized white light that excites all allowed resonant modes in the classic orthogonal polarization states where the number of existing modes and associated sensor peaks is controllable by design. GMR sensors exhibit high sensitivity while being arrayable in a compact format and integrated with microwell upper structures in standard formats. Here, we apply this sensor concept and attendant engineered reader system to the detection of neuropeptide Y.

The label-free GMR biosensor was first implemented more than two decades ago. Magnusson and Wang suggested the use of guided-mode resonance for sensor applications and demonstrated optical filters that were tunable by varying the parameters of the resonance structure, including thickness and refractive index [87] [2]. Wawro et al. presented new GMR biosensor embodiments, as well as possible applications of these sensors when integrated on optical fiber tips [36]. Refractive index sensing by GMR gratings [88] and use for biochemical assays [89] were subsequently reported. An experiment using a GMR aptasensor showed the capability of real-time, label-free detection of thrombin ranging in concentrations from 0.25–1 μM, with a limit of detection (LOD) of 0.19 μM [90]. GMR biosensors are used for the real-time monitoring of the action of saponin on live cells in the absence and presence of cytoskeleton modulators [91]. In another embodiment, the GMR biosensor consisted of a glass substrate, a waveguide film with an embedded grating structure, and a cell layer used for monitoring ligand-induced dynamic mass redistribution in living cells that were directly cultured on the sensor

surface [92]. In general, a major advantage of this sensor methodology is the adaptability to various chemical- and biological-sensing needs via facile modifications of pertinent surface chemistry for any particular application.

Neuropeptide Y (NPY) is the most abundant neuropeptide in the brain; it is a member of a family of proteins that include pancreatic polypeptide, peptide YY, and seminalplasmin [93]. Practical NPY analysis is challenging because NPY exists in the human body at picomolar levels [94] [95]; in blood at 0.14–0.6 pM; in urine at 0.1–0.7 pM; and in saliva at 10–12 pM [96]–[99]. NPY is associated with stress resilience for the diagnosis of post-traumatic stress disorder, traumatic brain injury, and neurotrauma [100]. Liquid chromatography-mass spectrometry (LCMS) is used to detect NPY in plasma samples, but it exhibits a poor sensitivity, of 5 μM [101]. NPY fluorescence immunoassays demonstrate a sensitivity of 50 pg/mL and a linear range of 0.1–100 ng/mL for NPY; however, this method is time-consuming, requiring a specific clinical environment and instruments to prepare the plate and process the samples [102]. Millipore Human NPY 96-Well Plate Assay (Cat. # EZHNPY-25K) uses fluorescent colorimetry to measure and quantify NPY levels. The standard curve ranges from 5 pg/mL (~2 pM) to 1000 pg/mL (~235 pM).

Recently, an aptamer-functionalized graphene-gold nanocomposite (Gr–AuNs) was used for the label-free detection of dielectrophoretic enriched NPY, where aptamer-NPY binding sufficiently close to the Gr–AuNs surface promotes electron transfer and carries out the electrochemical oxidation of tyrosine. The electrochemical oxidation of tyrosine occurs when NPY molecules bind to the aptamer, while other molecules containing tyrosine do not bind to the aptamer and are incapable of electron transfer. NPY can be detected at 10 pM levels, with linear signal characteristics in the physiologically relevant range of 10–1000 pM NPY [103]. Further, a

functionalized graphene field-effect transistor (GFET) device captures NPY directly via bi-domain peptides. A specific biological recognition element P1N3 was used to functionalize GFET devices to produce a biosensor device with picomolar sensitivity to NPY. The GFET shows alteration in the direct voltage for a range of NPY of 1–100 pM [104].

In this research, a guided-mode resonance sensor platform is used to capture NPY using an antibody for rapid and ultrasensitive detection. The platform consists of GMR sensor elements incorporated into the bottom of 96-well microtiter plates, so that a high-throughput assay can be processed instantaneously under the same conditions and with controlled temperature. In concert with the appropriate surface chemistry, NPY is immobilized on the sensor surface. A secondary antibody is added to the well, thus realizing a sandwich assay that enables NPY quantification at sub-picomolar levels. The results presented here show ~×5000 improvement in the LOD over recent preliminary data [105].

6.2 Materials and methods

6.2.1 Materials and instruments

All analytical grade reagents used in this work were purchased from Sigma-Aldrich (St. Louis, MO, USA), unless noted otherwise. Avidin-D (deglycosylated) was purchased from Santa Cruz Biotechnology (Dallas, TX, USA). The neuropeptide Y (NPY) antibody conjugated with Biotin was purchased from Novus Biotechnology (Centennial, CO, USA). Neuropeptide Y was purchased from Abcam (Cambridge, UK). The sensor plates used were supplied by Resonant Sensors Incorporated (RSI, Arlington, TX, USA). The ResoSens bioassay system, which includes a light source, a temperature control module, and a reader with the Bionetic microarray plates applied here, was manufactured by RSI. [106]

6.2.2 Sensor plate preparation

The biosensors used in this research were fabricated using low-cost submicron molding methods. We employed polymers imprinted with submicron grating patterns (~500 nm grating periods, ~100 nm grating height) coated with a high-index dielectric material (such as TiO2) to realize resonant sensors. **Figure 6-1**a shows an atomic force microscope (AFM) image of a ~500 nm-period grating and the corresponding measured profile.

Wawro et al. described the sensor measurement methodology, where a broadband light source illuminates the GMR biosensors, and where a specific wavelength of light is reflected (**Figure 6-1**b). These sensors are designed to operate in the near-IR wavelength range (700–900 nm), where most biochemical materials have minimal absorption [36]. The reflectance spectral response for TM polarization (magnetic vector normal to the plane of incidence, which is normal to the grooves) and TE polarization (electric vector normal to the plane of incidence) was calculated by a rigorous coupled-wave analysis (RCWA) for the GMR sensor element [107]. **Figure 6-1**c shows the reflection spectrum measured for deionized (DI) water and a calculated spectrum using RCWA for a refractive index of 1.33.

The quality (Q) factor can be extracted by calculating the wavelength linewidth ratio ($\lambda/\Delta\lambda$). The calculated Q-factors for TM and TE peaks were ~130 and ~368, respectively. Notice that the TE "peak" is turned downwards on account of the Gaussian shape of the readout incident light beam. The sensitivity for the TM peak was 107 nm/RIU and for the TE peak 338 nm/RIU. For optical resonance sensors, high sensitivity and Q-factors are desired in order to improve the sensing performance. Circular or tubular-shaped whispering gallery mode optical microcavities are well known to have a narrow linewidth and high Q-factors. Label-free sensing of bovine serum albumin molecules is estimated down to 10 fg/mL [108]. Thus, microring sensor concepts

possess high sensitivities but with drawbacks including fabrication and alignment challenges. The GMR sensor technology is attractive based on low cost, easy fabrication, and easy input light coupling, while possessing ample sensitivity and specificity for most applications, as exemplified in this work. The analyte binding changes the local refractive index and therefore the TM and TE resonance peak locations. Moreover, bulk background index variation will affect the resonance positions. **Figure 6-1**d illustrates calculated peak location changes for an example bulk refractive-index variation from 1.34 to 1.44. Such GMR wavelength shifts are used to quantify analyte binding that generates local biofilms with finite thickness and density representing a refractive-index increase.

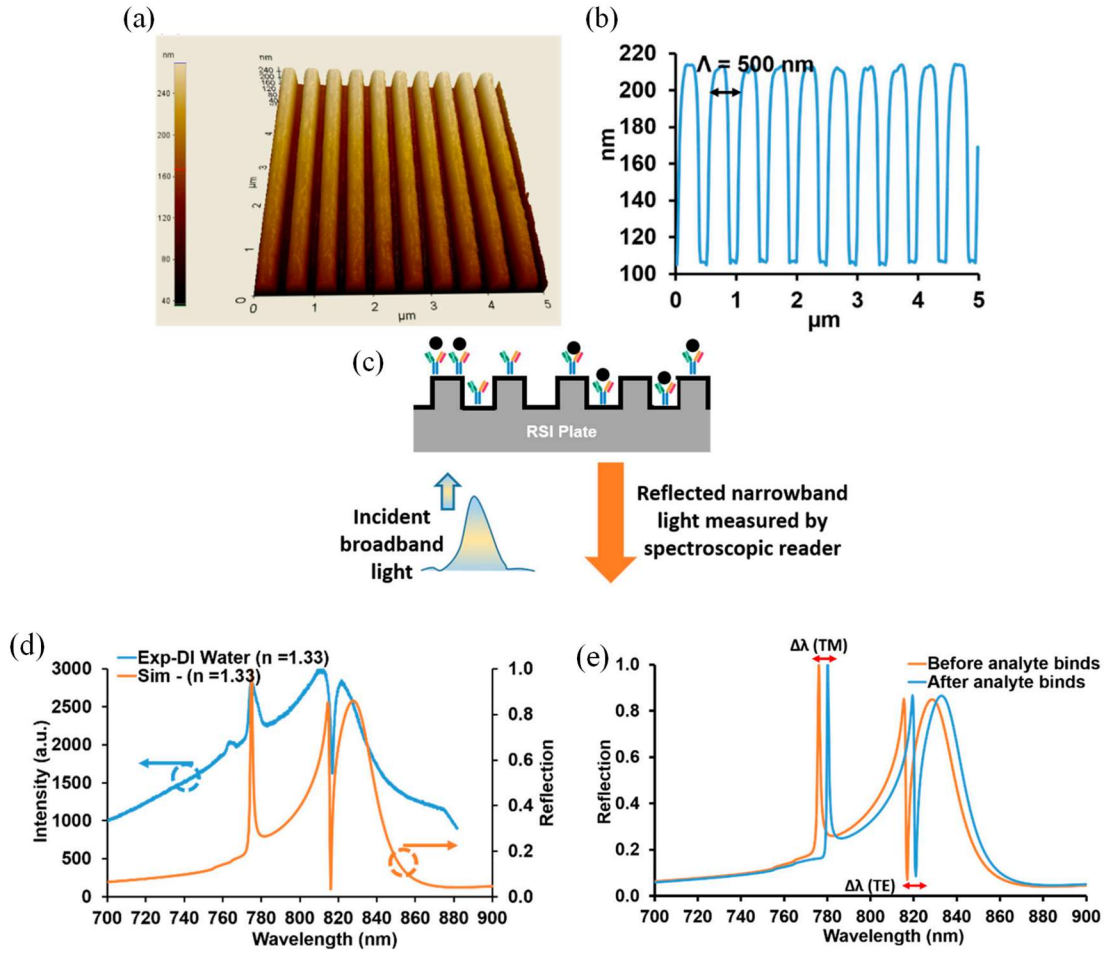

Figure 6-1 RSI sensor. (a) 3D atomic force microscope (AFM) image of a guided-mode resonance (GMR) sensor surface with a grating period of ~500 nm and the attendant measured profile. (b) Schematic of a GMR sensor operating in reflection mode. Broadband unpolarized light was incident on the sensor in the form of a Gaussian beam. The reflected spectral response was monitored in real-time with an optical spectrum analyzer. (c) A measured reflection spectrum of a GMR sensor vs. a rigorous coupled-wave analysis (RCWA) calculated spectrum. (d) Calculated reflection spectrum for TM and TE mode resonance by RCWA. Shown is a computed GMR optical biosensor resonance-peak shift due to a change of refractive index from 1.34 to 1.44. In the subsequent sections, these shifts are monitored to quantify the NPY bioreactions.

Proceeding to the experiments, first, the plate was rinsed with ethanol and then washed with deionized (DI) water and dried in N_2 flow. Next, the plate was treated with oxygen plasma (PSD Pro-digital UV ozone system) for 10 min to promote the surface hydrophilicity, then it was immersed in 3% (3-Aminopropyl) triethoxysilane (APTES) in a methanol solution for 30 min [109]. The plate was rinsed with methanol and DI water and dried with N2 flow. Subsequently, the plate was baked at 95 ◦C for 30 min. A dimethylformamide (DMF) solution containing 10% pyridine and 5 mmol/L phenyldiisothiocyanate (PDITC) was prepared, and the plate was immersed in it overnight. The plate was washed with DMF and 1,2-dichloroethane and dried under a stream of nitrogen. Finally, the plate was stored at 4 ◦C. **Figure 6-2**a summarizes this procedure.

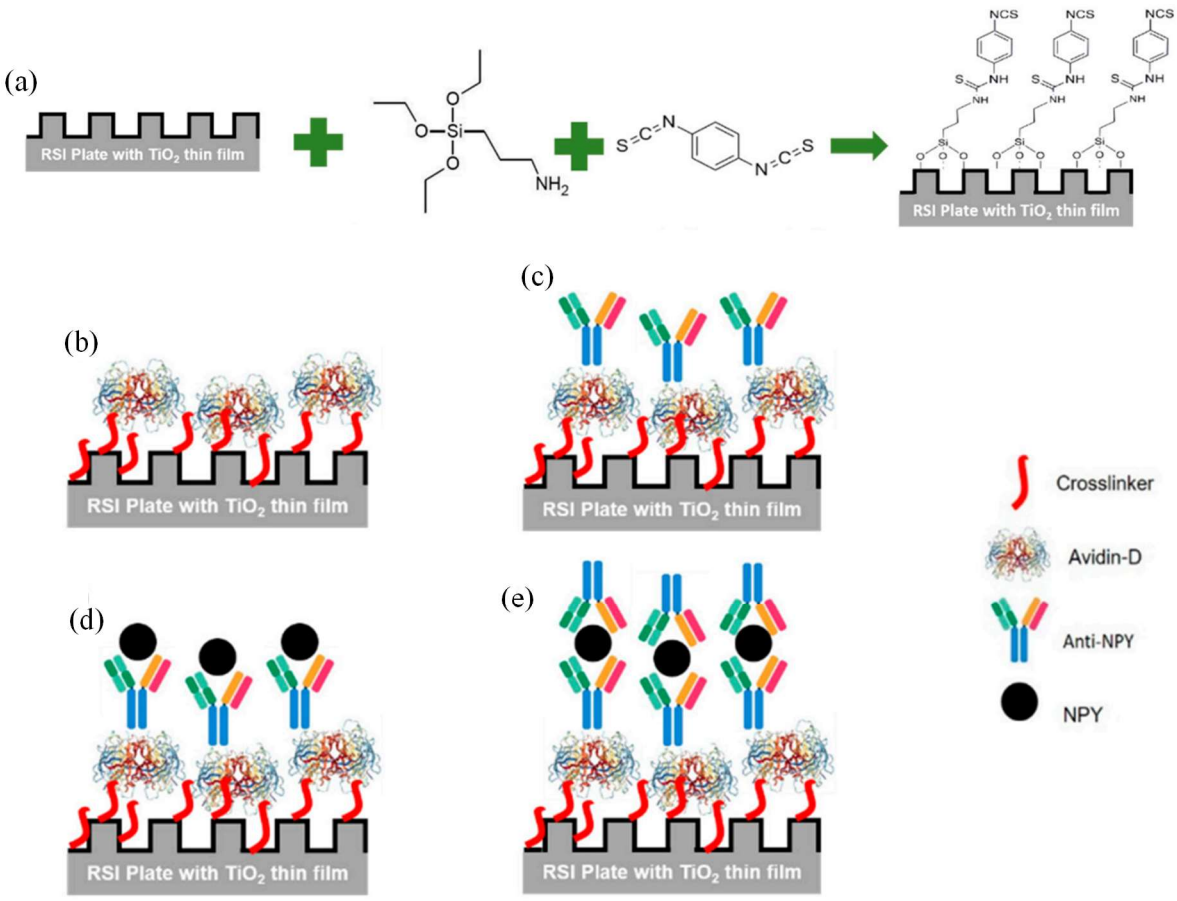

Figure 6-2 The sandwich neuropeptide Y (NPY) assay principle used in this work. (a) Plate preparation for Avidin-D attachment defining cross-linker chemistry. (b) Avidin-D immobilization at the sensor surface. (c) Covalent coupling of Avidin-D and anti-NPY [Biotin] to form the biorecognition element (BRE). (d) NPY attachment to the immobilized BRE. (e) NPY sandwich-type detection using secondary anti-NPY molecules.

6.2.3 Surface immobilization of avidin-D

First, we prepared 50, 100, 200, and 250 µg/mL solutions of Avidin-D in phosphate buffer saline (PBS). Next, 50 µL were added to a well and the wavelength shift measured at a controlled temperature of 30 °C to minimize any sensitivity changes due to thermal fluctuations. The wells were washed three times with washing buffer (PBS @ pH 7.4) and measured again to confirm

the immobilization of Avidin-D on the surface (**Figure 6-2**b). The wavelength shifts of reference wells containing PBS @ pH 7.4 were only measured concurrent with Avidin-D data collection and subtracted from the Avidin-D data to report the net wavelength shift without the background changes (# of wells n = 2). The wavelength shift was plotted vs. time, and the average wavelength shift and standard deviation after the washing step were reported. Then, SuperBlock™ (PBS) blocking buffer purchased from ThermoFisher was added to each well and washed with a washing buffer after 30 min to reduce nonspecific binding on the sensor surface.

6.2.4 Surface Immobilization of anti-NPY [biotin]

Solutions of anti-NPY [Biotin] with 20 µg/mL (117.65 nM) and 10 µg/mL (58.82 nM) in PBS were prepared. Next, 50 µL were added in the well, and the wavelength shift was measured at a controlled temperature of 30 ◦C to minimize any sensitivity changes due to thermal fluctuations. The wells were washed three times with a washing buffer (PBS @ pH 7.4), to remove excess unbound antibodies, and measured again to confirm the coupling of Avidin-D/Anti-NPY [Biotin] to the surface and the formation of the biorecognition element (BRE) (**Figure 6-2**c). The wavelength shifts of the reference wells (# of wells n = 2) (immobilized Avidin-D) with PBS @ pH 7.4 were measured concurrent with anti-NPY [Biotin] data collections and subtracted from anti-NPY [Biotin] data to report the net wavelength variation. The wavelength shift was plotted vs. time, and the average shift and standard deviation after the washing step were reported.

6.2.5 Sandwich NPY assay

The NPY concentration was quantified between two layers of antibodies: the capture and the detection antibody. First, NPY solutions with a final concentration of 0.1 pM (0.4 pg/mL), 0.5 pM (2 pg/mL), 5 pM (21 pg/mL), 62.5 pM (0.3 ng/mL), 125 pM (0.5 ng/mL), 0.5 nM (2 ng/mL),

1.0 nM (4 ng/mL), 5.0 nM (21 ng/mL), and 10.0 nM (43 ng/mL) in PBS @ pH 7.4 were prepared from a 1 µg/mL NPY stock solution. 50 µL were added to the anti-NPY [Biotin] loaded sensor assay wells, and wavelength shifts were measured at a controlled temperature of 30 ◦C to minimize any sensitivity changes due to thermal fluctuations (**Figure 6-2**d). Then, the wells were washed three times with a washing buffer, and 50 µL of the anti-NPY solution (10 µg/mL) were added to the assay wells. Finally, the wavelength shift was measured; then, the wells were washed three times with washing buffer and measured to confirm the capture of NPY (**Figure 6-2**e). Again, the wavelength shifts of the reference wells (# of wells = 2) (immobilized anti-NPY [Biotin]) with PBS @ pH 7.4 were measured concurrent with sandwich NPY assay data collection and subtracted from the sandwich NPY assay data. The wavelength shift was plotted vs. time, and the average wavelength shift and standard deviation after the washing step were reported.

6.3 Results and discussion

6.3.1 Avidin-D characterized

The Avidin-D wavelength shift was measured for different concentrations (50, 100, 200, and 250 µg/mL). The 50 µg/mL concentration showed the average wavelength shift after washing ~0.67 ± 0.011 nm. The shifts for 100, 200, and 250 µg/mL of Avidin-D were ~0.86 ± 0.009, ~1.03 ± 0.012, and 0.92 ± 0.008 nm, respectively (**Figure 6-3**). The data showed a linear relationship between the Avidin-D concentration and wavelength shift between 50–200 µg/mL. At 250 µg/mL, the wavelength shift declined. Thus, a ~200 µg/mL concentration of Avidin-D suffices to saturate the sensor surface.

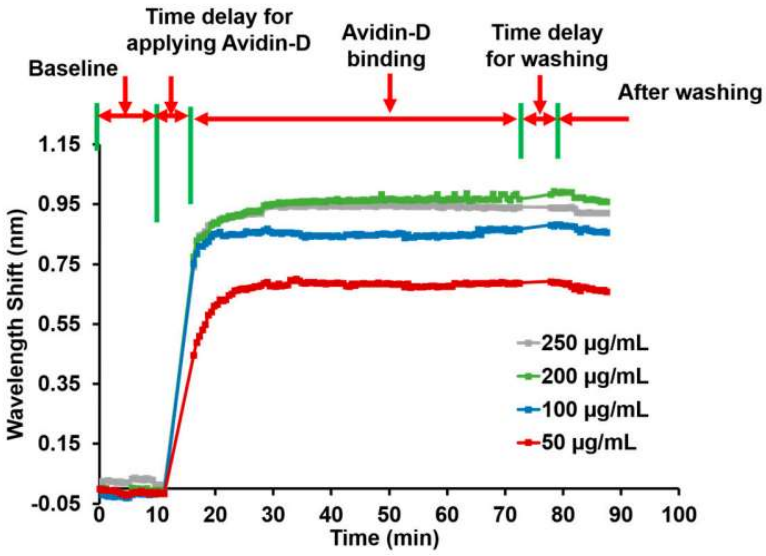

Figure 6-3 Avidin-D incubation. Wavelength shift and process steps as a function of time for 50, 100, 200, and 250 µg/mL Avidin-D concentrations. The final wavelength shifts are approx. 0.67, 0.86, 1.03, and 0.92 nm for 50, 100, 200, and 250 µg/mL Avidin-D, respectively.

Nonspecific binding can be a problem and reduce the sensitivity of the assay. The blocking of remaining active sites on Avidin-D immobilized sensor surfaces with a blocking buffer significantly reduces the nonspecific binding of proteins to the sensor surface, thus yielding lower detection limits.

6.3.2 Anti-NPY characterization

Avidin-Biotin coupling captures Biotin-tagged anti-NPY on an Avidin-D loaded sensor surface. **Figure 6-4** shows the resonance wavelength shift monitoring for anti-NPY binding to Avidin-D over time. The first step was the baseline measurement to set the reference for all subsequent measurements. Applying anti-NPY produced a resonance wavelength shift that implied a successful binding reaction between the anti-NPY [Biotin] molecules and the Avidin-D layer. The average wavelength shift measured in triplicates was ~0.55±0.005 nm for 20 µg/mL (117.65 nM) of anti-NPY and ~0.24 ± 0.001 nm for 10 µg/mL (58.82 nM) of anti-NPY after the

washing step. Avidin-D and Biotin had an equilibrium dissociation constant of ~10–15 M, which produced strong binding affinity, confirming the presence of Biotin-tagged anti-NPY on the sensor surface even with a lower concentration of anti-NPY. The higher wavelength shift for 20 µg/mL anti-NPY showed that more Avidin-D binding sites were available to bind specifically to Biotin-tagged anti-NPY. For the NPY sandwich assay, 10 µg/mL of anti-NPY were used to conduct all the experiments. Further investigation must be completed to find the optimal concentrations and the effect of the BRE concentration on the sensitivity.

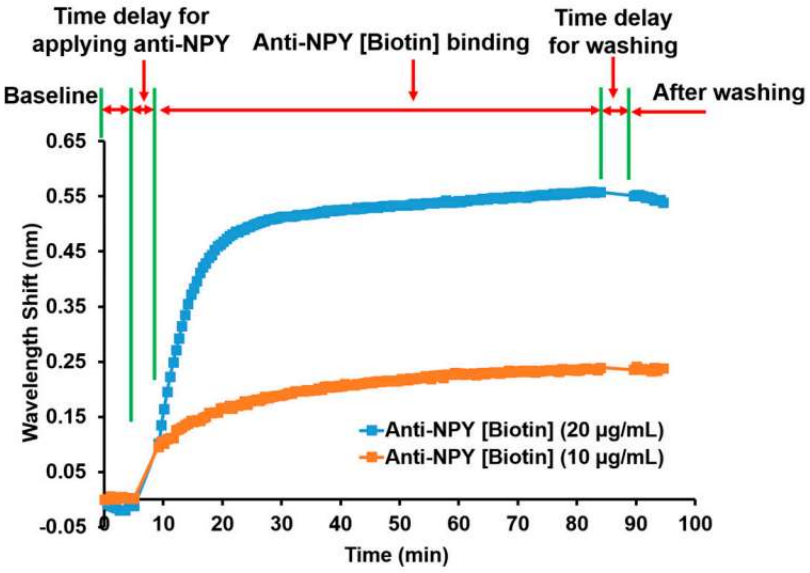

Figure 6-4 Biotin incubation. Wavelength shift and process steps as a function of time for anti-NPY [Biotin] binding to Avidin-D. The curves represent triplicate (n = 3) averages.

6.3.3 Sandwich NPY assay

The anti-NPY/NPY/anti-NPY sandwich assay approach was used to quantify low concentrations of NPY. The process steps are shown in **Figure 6-5**a. We applied different concentrations (0.1, 0.5, and 5 pM and 0.0625, 0.125, 0.5, 1.0, 5.0, and 10.0 nM) of the NPY solution to the anti-NPY loaded sensor surface and measured the corresponding resonance

wavelength shifts during the ~20–60 min interval; we saw minimal shifts. Next, the second anti-NPY was added to bind to, and detect, NPY over ~60–115 min, as indicated in **Figure 6-5**a. We measured averaged wavelength shifts of ~11 ± 5 pm (n = 3), 20 ± 5 pm (n = 3), 27 ± 2 pm (n = 3), 46 ± 3 pm (n = 3), 62 ± 4 pm (n = 3), 96 ± 5 pm (n = 3), 149 ± 3 pm (n = 3), 183 ± 7 pm (n = 3), and 225 ± 4 pm (n = 3) for 0.1, 0.5, 5, 62.5, and 125 pM and 0.5, 1, 5, and 10 nM concentrations of NPY, respectively. Thus, we see that the sandwich assay was extremely successful in detecting miniscule concentrations of NPY. To quantify the limit of detection applicable here in more detail, we focused in on the lowest concentration data. Thus, **Figure 6-5**b shows zoomed-in results for 0.1 and 0.5 pM NPY after washing. It is clear that these concentrations provided measurable wavelength shifts and established the final LOD for the class of biomaterials under study.

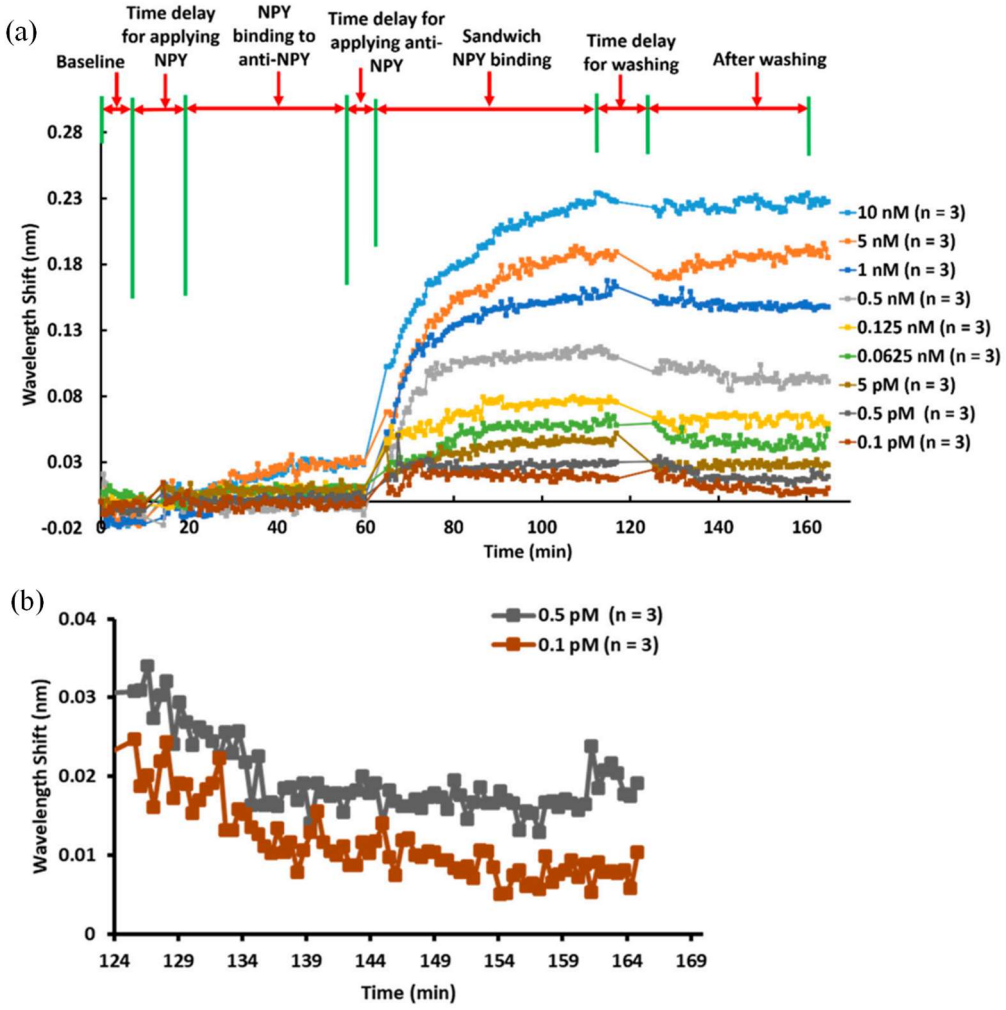

Figure 6-5 NPY sandwich incubation. (a) Process steps and averaged (in triplicates) wavelength shift response for the NPY sandwich assay as a function of NPY concentration. (b) Zoomed-in results for 0.1 and 0.5 pM NPY after the washing step, demonstrating the limit of detection (LOD) pertinent to these experiments.

Figure 4-6a shows a bar chart of wavelength shift vs. NPY concentration (n = 3; error bars = ± standard deviation) for the results shown in **Figure 6-5**. One-way ANOVA statistical analysis was performed on the wavelength changes for the collected data and showed p value < 0.0005, which means the wavelength shifts measured for each NPY concentration were statistically

different. The LOD is the lowest amount of NPY concentration that can be detected using the GMR sensor methodology, which was 0.1 pM for NPY in our experiments.

The data were transformed into a logarithmic scale to verify a linear relationship between concentration and resonance wavelength shift. A regression fit was used to estimate the degree of linearity. **Figure 4-6**b establishes a linear response of NPY concentrations ranging from 0.1 pM to 10 nM vs. wavelength shift with R2 = 0.982. For this data representation, the sensitivity can be expressed as 0.258 Log (Δλ, pm)/Log ([NPY], nM).

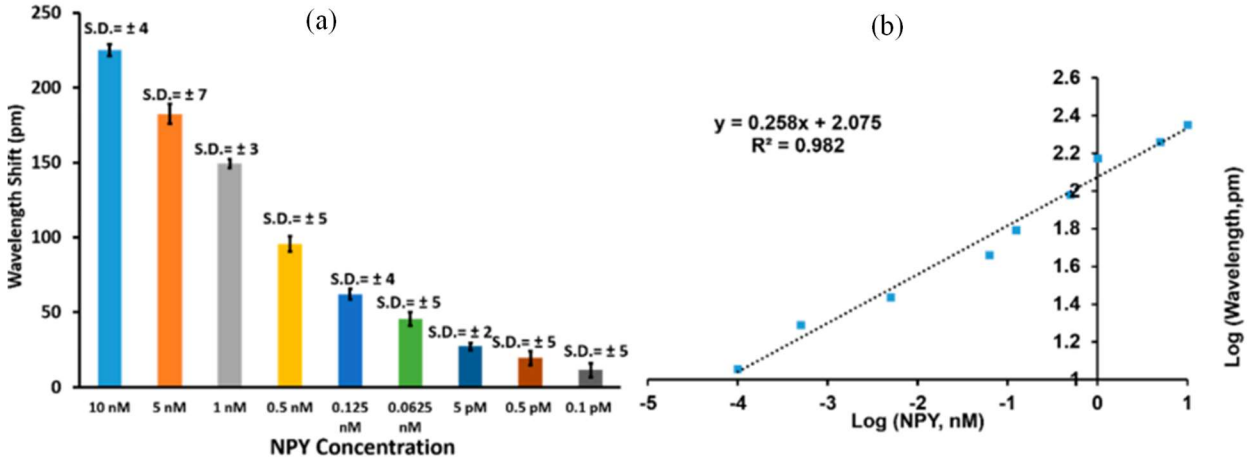

Figure 6-6 GMR NPY detection. (a) Bar chart of wavelength shift vs. NPY concentration. (b) Log-log plot of wavelength shift versus concentration. The logarithmic transformation was applied to establish a linear relationship for the concentration range from 0.1 pM to 10 nM of NPY.

6.4 Conclusions

We report the measurement of low concentrations of NPY enabled by the anti-NPY sandwich-type capture of NPY. The initial anti-NPY capture molecules were successfully immobilized on a submicron grating-based sensor surface coated with TiO2. We demonstrated a rapid and accurate detection of NPY via the sandwich assay, such that NPY could be detected at

levels of 0.1 pM (0.4 pg/mL), which is a ~×20 increase above the Millipore commercialized kit and ~×10 better than the detection limit of functionalized GFETs. The sensor data analysis for NPY indicated a linear response for NPY concentrations in the range of 0.1 pM–10 nM NPY. The optical resonance sensing method, coupled with the rapid assay technique deployed here, with controlled sample temperature and 96-well plates for high throughput, is likely applicable to other technology areas, including enzymes, anti-fouling surfaces, and nanobodies. Further work is necessary to use this approach to detect NPY from human samples and in clinical settings; such experiments are beyond the scope of the current report.

Chapter 7

Future work

In Chapter 2 and Chapter 3 it is demonstrated that a multimode guided-mode resonance (GMR) device can be implemented as a multiparametric sensor. This sensor simultaneously yields data quantifying changes in biolayer thickness, biolayer index of refraction, and bulk index of refraction. The design and implementation of a more sensitive multimode sensor would result in resonance shifts that significantly differ from each other given biolayer and bulk changes. This would give the lookup table value sets uniqueness which would improve the inversion process. Also, the development of a lookup table with a denser grid of simulated biolayer and bulk values would reduce the error in the inversion algorithm results.

The GMR-assisted Rayleigh sensor was introduced in Chapter 4. Under conditions where a GMR shapes a wavelength range of interest, the Rayleigh anomaly can produce a transmission peak that shifts with the bulk index of refraction. The resonant peak of these devices shifts by an amount equal to the device period per RIU. Fabricating a GMR-assisted Rayleigh sensor and experimentally establishing the device sensitivity would be meaningful progress for this class of device.

In Chapter 5 we show that the addition of a thin layer of silicon to the top of the high index portion of a GMR grating can increase the sensitivity of a device nearly 5-fold. Developing a method to fabricate silicon-incorporated devices and experimentally measuring the sensitivity of these devices is a potential next step in this work.

Lastly, in Chapter 6 we apply sandwich assay to neuropeptide Y at picomolar concentrations using a GMR sensor. The limit of detection achieved in this work is significant in the field of biomolecule sensing. Application of sandwich assay using a GMR sensor with other analytes at

low concentrations can make this detection method more common place in the field of GMR sensors.

List of publications

Journal publications

1. **J. A. Buchanan-Vega**, and R. Magnusson, “Rayleigh-anomaly-transmission sensors assisted by modal resonance modal effects,” (in progress) 2024
2. **J. A. Buchanan-Vega**, and R. Magnusson, “Multiparametric GMR Biosensor to Monitor Bulk and Surface-Film Variations,” Chemosensors, vol 10, no. 541, 2022.
3. M. G. Abdallah, **J. A. Buchanan-Vega**, B. R. Wenner, J. W. Allen, M. S. Allen, S. Gimlin, D. Wawro Weidanz and R. Magnusson, "Attachment and Detection of Biofouling Yeast Cells Using Biofunctionalized Resonant Sensor Modality," IEEE Sensors Journal, vol. 21, no. 5, pp. 5995-6002, 2021.
4. M. G. Abdallah, **J. A. Buchanan-Vega**, K. J. Lee, B. R. Wenner, J. W. Allen, M. S. Allen, S. Gimlin, D. W. Weidanz, R. Magnusson*, “Quantification of Neuropeptide Y with Picomolar Sensitivity Enabled by Guided-Mode Resonance Biosensors,” *Sensors (Basel, Switzerland),* vol. 20, no. 126, 2020.

Conference proceedings

1. R. Magnusson, Y. H. Ko, N. Razmjooei, K. J. Lee, F. A. Simlan, R. Chen, **J. A. Buchanan-Vega**, P. Bootpakdeetam, and N. Gupta, “Properties and principles of resonant optical lattices,” IEEE Research and Applications of Photonics In Defense Conference (RAPID), Miramar Beach, Florida, USA, 12-14 September 2022. Invited.
2. R. Magnusson, Y. H. Ko, K. J. Lee, P. Bootpakdeetam, N. Razmjooei, F. A. Simlan, R. Chen, **J. A. Buchanan-Vega**, D. J. Carney, H. Hemmati, N. Gupta, "Perfect reflection by dielectric subwavelength particle arrays: causes, implications, and technology," Proc. SPIE 11689, Integrated Optics: Devices, Materials, and Technologies XXV, 1168912 (5 March 2021); https://doi.org/10.1117/12.2578953 Photonics West, San Francisco, 6-11 March 2021. Invited.

References

[1] M. S. Amin, J. W. Yoon and R. Magnusson, "Optical transmission filters with coexisting guided-mode resonance and Rayleigh anomaly," *Applied Physics Letters,* vol. 103, no. 13, p. 131106, 2013.

[2] R. Magnusson and S. S. Wang, "New Principle for Optical Filters," *Applied Physics Letters,* vol. 61, no. 9, pp. 1022-1024, 1992.

[3] E. Popov, L. Mashev and D. Maystre, "Theoretical study of the anomalies of coated dielectric gratings," *Optica Acta: International Journal of Optics,* vol. 33, no. 5, pp. 607-619, 1986.

[4] G. A. Golubenko, V. A. Svakhin, V. A. Sychugov and A. V. Tishchenko, "Total reflection of light from a corrugated surface of a dielectric waveguide," *Journal of Quantum Electronics,* vol. 15, no. 7, pp. 886-887, 1985.

[5] Y. Ding and R. Magnusson, "Resonant leaky-mode spectral-band engineering and device applications," *Optics Express,* vol. 12, no. 23, pp. 5661-5674, 2004.

[6] R. Magnusson, J. W. Yoon, M. S. Amin, T. Khaleque and M. J. Uddin, "Extraordinary capabilities of optical devices incorporating guided-mode resonance gratings: application summary and recent examples," in *In Integrated Optics: Devices, Materials, and Technologies XVIII. SPIE*, 2014.

[7] M. Niraula, J. W. Yoon and R. Magnusson, "Mode-coupling mechanisms of resonant transmission filters," *Optics Express,* vol. 22, no. 21, pp. 25817-25829, 2014.

[8] P. Vincent and Nevière, "Corrugated dielectric waveguides: a numerical study of the second-order stop bands," *Applied Physics,* vol. 20, no. 4, pp. 345-351, 1979.

[9] L. Mashev and E. Popov, "Zero order anomaly of dielectric coated gratings," *Optics Communications,* vol. 55, no. 6, pp. 377-380, 1985.

[10] A. Avrutsky and V. A. Sychugov, "Reflection of a beam of finite size from a corrugated waveguide," *Journal of Modern Optics,* vol. 36, no. 11, pp. 1527-1539, 1989.

[11] M. G. Moharam, E. B. Grann, D. A. Pommet and T. K. Gaylord, "Formulation for stable and efficient implementation of the rigorous coupled-wave analysis of binary gratings," *Journal of the Optical Society of America,* vol. 12, no. 5, pp. 1068-1076, 1995.

[12] S. S. Wang and R. Magnusson, "Theory and applications of guided-mode resonance filters," *Applied Optics,* vol. 32, no. 14, pp. 2606-2613, 1993.

[13] R. Magnusson and M. Shokooh-Saremi, "Physical basis for wideband resonant reflectors," *Optics Express,* vol. 16, no. 5, pp. 3456-3462, 2008.

[14] M. Shokooh-Saremi and R. Magnusson, "Wideband leaky-mode resonance reflectors: influence of grating profile and sublayers," *Optics Express,* vol. 16, no. 22, pp. 18249-18263, 2008.

[15] D. Maystre, "Theory of Wood's Anomalies," in *Plasmonics: from basics to advanced topics*, Berlin, Heidelberg: Springer Berlin Heidelberg, 2012, pp. 39-83.

[16] K. J. Lee, Y. H. Ko, N. Gupta and R. Magnusson, "Unpolarized resonant notch filters for the 8-12 μm spectral region," *Optics Letters,* vol. 45, no. 16, pp. 4452-4455, 2020.

[17] R. Magnusson, D. Wawro, S. Zimmerman and Y. Ding, "Resonant Photonic Biosensors with Polarization-Based Multiparametric Discrimination in Each Channel," *Sensors,* vol. 11, no. 2, pp. 1476-1488, 2011.

[18] M. Maleki and M. Mehran, "Guided-mode resonance sensors: different schemes for different applications," *Journal of the Optical Society of America B,* vol. 39, no. 6, pp. 1634-1643, 2022.

[19] M. G. Abdallah, J. A. Buchanan-Vega, B. R. Wenner, J. W. Allen, M. S. Allen, S. Gimlin, D. Wawro Weidanz and R. Magnusson, "Attachment and Detection of Biofouling Yeast Cells Using Biofunctionalized Resonant Sensor Modality," *IEEE Sensors Journal,* vol. 21, no. 5, pp. 5995-6002, 2021.

[20] S. Kaja, J. D. Hilgenberg, J. L. Collins, A. A. Shah, D. Wawro, S. Zimmerman, R. Magnusson and P. Koulen, "Detection of novel biomarkers for ovarian cancer with an optical nanotechnology detection system enabling label-free diagnostics," *Journal of Biomedical Optics,* vol. 17, no. 8, pp. 1-8, 2012.

[21] K. Tantiwanichapan, R. Jolivot, A. Jomphoak, N. Srisuai, C. Chananonnawathorn, T. Lertvanithpol, M. Horprathum and S. Boonruang, "Demonstration of cross reaction in hybrid graphene oxide/tantalum dioxide guided mode resonance sensor for selective volatile organic compound," *Scientific Reports,* vol. 13, no. 1, pp. 1-10, 2023.

[22] Y. H. Joo, S. H. Song and R. Magnusson, "Demonstration of long-range surface plasmon-polariton waveguide sensors with asymmetric double-electrode structures," *Applied Physics Letters,* vol. 97, no. 3, pp. 1-3, 2010.

[23] S. Romano, A. Lamberti, M. Masullo, E. Penzo, S. Cabrini, I. Rendina and V. Mocello, "Optical biosensors based on photonic crystals supporting bound states in the continuum," *Materials,* vol. 11, no. 526, pp. 1-11, 2018.

[24] S. Mesli, H. Yala, M. Hamidi, A. BelKhir and F. I. Baida, "High performance for refractive index sensors via symmetry-protected guided mode resonance," *Optics Express,* vol. 29, no. 14, pp. 21199-21211, 2021.

[25] G. Lan, S. Zhang, H. Zhang, Y. Zhu, L. Qing, D. Li, J. Nong, W. Wang, L. Chen and W. Wei, "High-performance refractive index sensor based on guided-mode resonance in all-dielectric nano-slit array," *Physics Letter A,* vol. 383, no. 13, pp. 1478-1482, 2019.

[26] X. Lu, G. G. Zheng and P. Zhou, "High performance refractive index sensor with stacked two-layer resonant waveguide gratings," *Result in Physics,* vol. 12, pp. 759-765, 2019.

[27] L. Qian, T. Gu, S. Xu, X. Zhang and K. Wang, "Guided-mode resonance sensors with ultrahigh bulk sensitivity and figure of merit assisted by a metallic layer and structural symmetry-breaking," *Optics Express,* vol. 31, no. 2, pp. 1844-1857, 2023.

[28] H. Vyas and R. S. Hegde, "Improved refractive-index sensing performance in medium contrast gratings by asymmetry engineering," *Optical Materials Express,* vol. 10, no. 7, pp. 1616-1629, 2020.

[29] V. Canalejas-Tejero, A. López, R. Casquel, M. Holgado and C. A. Barios, "Sensitive metal layer-assisted guided-mode resonance SU8 nanopillar array for label-free optical biosensing," *Sensors and Actuators B: Chemical,* vol. 226, pp. 204-210, 2016.

[30] D. Maksimov, V. S. Gerasimov, S. Romano and S. P. Polyutov, "Refractive index sensing with optical bound states in the continuum," *Optics Express,* vol. 28, no. 26, pp. 38907-38916, 2020.

[31] Y. Zhou, B. Wang, Z. Guo and X. Wu, "Guided mode resonance sensors with optimized figure of merit," *Nanomaterials,* vol. 9, no. 837, pp. 1-14, 2019.

[32] P. Edmonds and J. J. Cooney, "Identification of Microorganisms Isolated from Jet Fuel Systems," *American Society for Microbiology,* vol. 15, no. 2, pp. 411-416, 1967.

[33] C. M. Jung, C. Broberg, J. Giuliani, L. L. Kirk and L. F. Hanne, "Charactrization of JP-7 Jet Fuel Degradation by the Bacterium Nocardioides Luteus Strain BAFB," *Journal of Basic Micro Biology,* vol. 42, no. 2, pp. 127-131, 2002.

[34] D. Wawro, P. Koulen, Y. Ding, S. Zimmerman and R. Magnusson, "Guided-Mode Resonance Sensor System for Early Detection of Ovarian Cancer," *Proceedings of SPIE,* vol. 7572, no. 1, pp. 75720D - 75720D-6, 2010.

[35] F. J. Passman, "Microbial Contamination and its Control in Fuels and Fuel Systems since 1980 - a Review," *International Biodeterioration and Biodegradation,* vol. 81, pp. 88-104, 2013.

[36] D. D. Wawro, S. Tibuleac, R. Magnusson and H. Liu, "Optical Fiber Endface Biosensor Based on Resonances in Dielectric Waveguide Gratings," *Proceedings of the SPIE,* vol. 3911, pp. 86-94, 2000.

[37] Z. Ding, P. Liu, J. Chen, D. Dai and Y. Shi, "On-Chip Simultaneous Sensing of Humidity and Temperature with a Dual-Polarization Silicon Microring Resonator," *Optics Express,* vol. 27, no. 20, pp. 28649-28659, 2019.

[38] M. N. Hossain, J. Justice, P. Lovera, A. O'Riordan and B. Corbett, "Dual Resonance Approach to Decoupling Surface and Bulk Attributes in Photonic Crystal Biosensor," *Optics Letters,* vol. 39, no. 21, pp. 6213-6216, 2014.

[39] B. Cunningham, B. Lin, J. Qiu, P. Li, J. Pepper and B. Hugh, "A plastic colorimetric resonant optical biosensor for multiparallel detection of label-free biochemical interactions," *Sensors and Actuators B,* vol. 85, no. 3, pp. 219-226, 2002.

[40] M. R. Saleem, R. Ali, S. Honkanen and J. Turunen, "Bio-molecular sensors based on guided mode resonance filters," in *IOP Conference Series: Materials Science and Engineering*, Islamabad, 2016.

[41] K. A. Peterlinz and R. Georgiadis, "Two-Color Approach for Determination of Thickness and Dielectric Constant of thin Films Using Surface Plasmon Resonance Sprectroscopy," *Optics Communications,* vol. 130, no. 4, pp. 260-266, 1996.

[42] K. S. Johnston, S. R. Karlsen, C. C. Jung and S. S. Yee, "New Analytical Technique for Characterization of Thin Films Using Surface Plasmon Resonance," *Materials Chemistry and Physics,* vol. 45, no. 4, pp. 242-246, 1995.

[43] P. Adam, J. Dostálek and J. Homola, "Multiple Surface Plasmon Spectroscopy for Study of Biomolecular Systems," *Sensors and Actuators B: Chemical,* vol. 113, no. 2, pp. 774-781, 2006.

[44] H. E. de Bruijn, B. S. F. Altenburg, R. P. H. Kooyman and J. Greve, "Determination of Thickness and Dielectric Constant of Thin Transparent Dielectric Layers Using Surface Plasmon Resonance," *Optics Communications,* vol. 82, no. 5, pp. 425-432, 1991.

[45] F. Bahrami, J. S. Aitchison and M. Mojahedi, "Multimode Spectroscopy Using Dielectric Grating Coupled to a Surface Plasmon Resonance Sensor," *Optics Letters,* vol. 39, no. 13, pp. 3946-3949, 2014.

[46] Q. Shi, J. Zhao and L. Liang, "Two Dimensional Photonic Crystal Slab Biosensors Using Label Free Refractometric Sensing Schemes: A Review," *Progress in Quantum Electronics,* vol. 77, 2021.

[47] S. Das, S. C. Samudrala, K. J. Lee, M. G. Abdallah, B. R. Wenner, J. W. Allen, M. S. Allena, R. Magnusson and M. Vasilyev, "SiN-Microring-Resonator-Based Optical Biosensor for Neuropeptide Y Detection," *IEEE Photonics Technology Letters,* p. doi: 10.1109/LPT.2021.3069765, 2021.

[48] M. G. Abdallah, J. A. Buchanan-Vega, K. J. Lee, B. R. Wenner, J. W. Allen, M. S. Allen, S. Gimlin, D. Wawro Weidanz and R. Magnusson, "Quantification of Neuropeptide Y with Picomolar Sensitivity Enabled by Guided-Mode Resonance Biosensors," *Sensors,* vol. 20, no. 1, p. 126, 2019.

[49] M. A. Cooper, "Current Biosensor Technologies in Drug Discovery," *Drug Discovery,* vol. 7, pp. 68-82, 2006.

[50] R. Chandrasekar, Z. J. Lapin, A. S. Nichols, R. M. Braun and I. A. W. Fountain, "Photonic Integrated Circuits for Department of Defense-Relevant Chemical and Biological Sensing Applications: State-of-the-Art and Furture Outlooks," *Optical Engineering,* vol. 58, no. 2, 2019.

[51] W. Wang and L. Qi, "Light Management with Patterned Micro- and Nonostructure arrays for Photocatalysis, Photovoltaics and Optoelectronic and Optical Devices," *Advanced Functional Materials,* vol. 29, no. 25, p. 1807275, 2019.

[52] X. Guo, "Surface Plasmon Resonance Based Biosensor Technique: A Review," *Journal of Biophotonics,* vol. 5, no. 7, pp. 483-501, 2012.

[53] T. M. Chinowsky and S. S. Yee, "Quantifying the Information Content of Surface Plasmon Resonance Reflection Spectra," *Sensors and Actuators B: Chemical,* vol. 51, no. 1, pp. 321-330, 1998.

[54] J. Homola, "Present and Future of Surface Plasmon Resonance Biosensors," *Analytical and Bioanalytical Chemistry,* vol. 377, no. 3, pp. 528-539, 2003.

[55] A. L. Fannin, B. R. Wenner, J. W. Allen, M. W. Allen and R. Magnusson, "Properties of Mixed Metal-Dielectric Nanogratings for Application in Resonant Absorption, Sensing, and Display," *Optical Engineering,* vol. 56, no. 12, p. 121905, 2017.

[56] J. H. Schmid, W. Sinclair, J. Garcia, S. Janz, J. Lapoint, D. Poitras, Y. Li, T. Mischki, G. Lopinski, P. Cheben, A. Delage, A. Densmore, P. Waldron and D.-X. Xu, "Silicon-on-Insulator Guided Mode Resonant Grating for Evanescent Field Molecular Sensing," *Optics Express,* vol. 17, no. 20, pp. 18731-18380, 2009.

[57] S. Tibuleac, D. Wawro and R. Magnusson, "Resonant Diffractive Structures Integrating Waveguide Gratings on Optical Fiber Endfaces," in *Proceedings of the IEEE Lasers and Electro-Optics Society 12th Annual Meeting*, San Francisco, 1999.

[58] R. Magnusson, "The Complete Biosensor," *Biosensors and Bioelectronics,* vol. 4, no. 2, pp. 1-2, 2013.

[59] M. G. Moharam, E. B. Grann, D. A. Pommet and T. K. Gaylord, "Formulation for Stable and Efficient Implementation of the Rigorous Coupled-Wave Analysis of Binary Gratings," *Journal of the Optical Society of America A,* vol. 12, no. 5, pp. 1068-1076, 1995.

[60] RSoft Photonic Device Tools (Diffract MOD Synopsys), https://www.synopsys.com/photonic-solutions.

[61] D. H. Dusane, Y. V. Nancharaiah, A. P. Venugopalan, A. R. Kumar and S. S. Zinjarde, "Biofilm formation by a biotechnologically important tropical marine yeast isolate, Yarrowia Lipolytica NCIM 3589," *Water Sci. Technol.,* vol. 58, pp. 1221-1229, 2008.

[62] J. S. Tkacz, E. B. Cybulska and J. O. Lampen, "Specific staining of wall mannan in yeast cells with fluorescein-conjugated concavalin A. J.," *J. Bacteriol.,* vol. 105, pp. 1-5, 1971.

[63] U.S. Food Drug Administration. Accessed: Dec. 4, 2020. [Online]. Available: https://www.fda.gov/regulatory-information/search-fda-guidance-documents/q2b-validation-analytical-procedures-methodology.

[64] S. Tibuleac and R. Magnusson, "Narrow-linewidth bandpass filters with diffractive thin-film layers," *Optics Letters,* vol. 26, no. 9, pp. 584-586, 2001.

[65] S. Tibuleac and R. Magnusson, "Experimental verification of waveguide-mode resonant transmission filters," *IEEE Microwave and Guided Wave Letters,* vol. 9, no. 1, pp. 19-21, 1999.

[66] R. Magnusson, M. Shokooh-Saremi and X. Wang, "Dispersion engineerirng with leaky-mode resonant photonic lattices," *Optics Express,* vol. 18, no. 1, pp. 108-116, 2010.

[67] J. M. Foley, S. M. Young and J. D. Phillips, "Narrowband mid-infrared transmission filtering of a single layer dielectric grating," *Applied Physics Letters,* vol. 103, no. 7, pp. 071107-1 - 071107-5, 2013.

[68] T. Sang, T. Cai, S. Cai and Z. Wang, "Tunable transmission filters based on double-subwavelength periodic membrane structures with an air gap," *Journal of Optics,* vol. 13, no. 12, pp. 1-7, 2011.

[69] R. Magnusson and S. S. Wang, "Transmission bandpass guided-mode resonance filters," *Applied Optics,* vol. 34, no. 35, pp. 8106-8109, 1995.

[70] S. Tibuleac and R. Magnusson, "Reflection and transmission guided-mode resonance filters," *Journal of the Optical Society of America A,* vol. 14, no. 7, pp. 1617-1626, 1997.

[71] Y. Ding and R. Magnusson, "Doubly resonant single-layer bandpass optical filters," *Optics Letters,* vol. 29, no. 10, pp. 1135-1137, 2004.

[72] S.-G. Lee, S.-Y. Jung, H.-S. Kim, S. Lee and J.-M. Park, "Electromagnetically induced transparency based on guided-mode resonances," *Optics Letters,* vol. 40, no. 18, pp. 4241-4244, 2015.

[73] Y. Kanamori, M. Shimono and Y. Hane, "Fabrication of transmission color filters using silicon subwavelength gratings on quartz substrates," *IEEE Photonics Technology Letters,* vol. 18, no. 20, pp. 2126-2128, 2006.

[74] R. Sayeed, M. Mamun, V. Avrutin and Ü. Özgür, "Pixel-scale minitiarization of guided mode resonance transmission filters in short wave infrared," *Optics Express,* vol. 30, no. 8, pp. 12204-12214, 2022.

[75] R. He, C. Chen, R. Shen, E. Hu, R. Zhang, L. Chen and J. Guo, "Weakly coupled hybrid guided mode resonance optical transmission filter," *Journal of the Optical Society of America B,* vol. 39, no. 4, pp. 925-933, 2022.

[76] G. Sun and Q. Wang, "Electrically tunable polarization-independent visible transmission guided-mode resonance filter based on polymer-dispersed liquid crystals," *Microwave Optical Technology Letters,* vol. 65, no. 12, pp. 3727-3732, 2020.

[77] L. Rayleigh, "On the dynamical theory of gratings," *Proceedings of the Royal Society of London,* vol. 79, no. 532, 1907.

[78] D. B. Mazulquim, K. J. Lee, J. W. Yoon, L. V. Muniz, B. V. Borges, L. G. Neto and R. Magnusson, "Efficient band-pass color filters enabled by resonant modes and plasmons near the Rayleigh anomaly," *Optics Express,* vol. 22, no. 25, pp. 30843-30851, 2014.

[79] A. L. Fannin, B. R. Wenner, J. W. Allen, M. S. Allen and R. Magnusson, "Properties of mixed metal-dielectric nanogratings for application in resonant absorption, sensing, and display," *Optical Engineering,* vol. 56, no. 12, pp. 1-10, 2017.

[80] R. Magnusson, "Flat-top resonant reflectors with sharply delimited angular spectra: an application of the Rayleigh anomaly," *Optics Letters,* vol. 38, no. 6, pp. 989-991, 2013.

[81] H. Gao, M. M, M. H. Lee, J. Henzie, S. K. Gray, G. C. Schatz and T. W. Odom, "Rayleigh anomaly-surface plasmon polariton resonances in palladium and gold subwavelength hole arrays," *Optics Express,* vol. 17, no. 4, pp. 2334-2340, 2009.

[82] H. Deb, N. Srisuai, R. Jolivot, C. Promptmas, W. Mohammed and S. Boonruang, "Enhanced sensitivity of guided mode resonance sensor through super-mode excitation at near cut-off diffraction," *Optics and Laser Technology,* vol. 132, pp. 1-6, 2020.

[83] Y. Nazirizadeh, V. Behrends, A. Prósz, N. Orgovan, R. Horvath, A. M. Ferrie, Y. Fang, C. Selhuber-Unkel and M. Gerken, "Intensity interrogation near cutoff resonance for label-free cellular profiling," *Scientific Reports,* vol. 6, no. 1, pp. 1-6, 2016.

[84] J. A. Buchanan-Vega and R. Magnusson, "Multiparametric guided-mode resonance biosensor monitoring bulk and surface-film variation," *Chemosensors,* vol. 10, no. 541, pp. 1-17, 2022.

[85] Y. Zhou, Z. Guo, W. Zhou, S. Li, Z. Liu and X. Zhao, "High-Q guided mode resonance sensors based on shallow sub-wavelength grating structures," *Nanotechnology,* vol. 31, no. 32, pp. 1-7, 2020.

[86] H. Hemmati, Y. H. Ko and R. Magnusson, "Fiber-faceted-integrated guided-mode resonance filters and sensors: experimental realization," *Optics Letters,* vol. 43, no. 3, pp. 358-361, 2018.

[87] R. Magnusson and S. S. Wang, "Optical Guided-Mode Resonance Filter.," U.S. Patent 5,216,680, 1 June 1993.

[88] H. Kikuta, N. Maegawa, A. Mizutani, K. Iwata and H. Toyota, "Refractive index sensor with a guided-mode resonant grating filter," *Proc. SPIE,* vol. 4416, pp. 219-222, 2001.

[89] B. Cunningham, P. Li, B. Lin and J. Pepper, "Colorimetric resonant reflection as a direct biochemical assay technique," *Sens. Actuators B Chem.,* vol. 81, pp. 316-328, 2002.

[90] S. Lin, T. Ding, J. Lui, C. Lee, T. Yang, W. Chen and J. A. Chang, "A guided mode resonance aptasensor for thrombin detection," *Sensors,* vol. 11, pp. 8953-8965, 2011.

[91] Y. Fang, A. M. Ferrie and G. Li, "Probing cytoskeleton modulation by optical biosensors," *FEBS Lett.,* vol. 579, pp. 4175-4180, 2005.

[92] Y. Fang, A. G. Frutos and R. Verklereen, "Label-free cell-based assays for gpcr screening," *Comb. Chem. High. Throughput Scr.,* vol. 11, pp. 357-369, 2008.

[93] J. C. Erickson, K. E. Clegg and R. D. Palmiter, "Sensitivity to leptin and susceptibility to seizures of mice lacking neuropeptide Y," *Nature,* vol. 381, pp. 415-418, 1996.

[94] G. Cizza, A. H. Marques, F. Eskandari, I. C. Christie, S. Torvik, M. N. Silverman and E. M. Sternberg, "Elevated neuroimmune biomarkers in sweat patches and plasma of premenopausal women with major depressive disorder in remission: the power study," *Biol. Psychiatry,* vol. 64, pp. 907-911, 2008.

[95] S. H. Gruber, G. G. Nomikos and A. A. Mathé, "Effects of acute and subchronic d-amphetamine on ventral striatal concentrations of neurotensin and neuropeptide Y in rats treated with antipsychotic drugs," *Eur. Neuropsychopharmacol,* vol. 16, pp. 592-600, 2006.

[96] L. E. Kuo and Z. Zukowska, "Stress NPY and vascular remodeling: implications for stress-related diseases," *Peptides,* vol. 28, pp. 435-440, 2007.

[97] A. M. Rasmusson, S. M. Southwick, R. L. Hauger and D. S. Charney, "Plasma neuropeptide Y (NPY) increases in humans in response to the α2 antagonist yohimbine," *Neurophychopharmacology,* vol. 19, pp. 95-98, 1998.

[98] C. A. Morgan, A. M. Rasmusson, S. Wang, G. Hoyt, R. L. Hauger and G. Hazlett, "Neuropeptide-Y, cortisol, and subjective distress in humans exposed to acute stress: replication and extension of previous report," *Biol. Psychiatry,* vol. 52, pp. 136-146, 2002.

[99] C. Tu, D. Zhao and X. Lin, "Levels of neuropeptide-Y in the plasma and skin tissue fluids of patients with vitiligo," *J. Derm. Sci.,* vol. 27, pp. 178-182, 2001.

[100] J. A. Andrews and K. D. Neises, "Cells, biomarkers, and post-traumatic stress disorder: evidence for peripheral involvement in a central disease, peripheral cells, biomarkers, and PTSD," *J. Neurochem.,* vol. 120, pp. 26-36, 2012.

[101] K. Racaityte, E. Lutz, K. Unger, D. Lubda and K. Boos, "Analysis of neuropeptide Y and its metabolites by high-perfomance liquid chromatography-electrospray ionization mass spectrometry and integrated sample clean-up with a novel restricted-access sulphonic acid cation exchanger," *J. Chromatogr. A,* vol. 890, pp. 135-144, 2000.

[102] M. Jia, E. Belyavskaya, P. Deuster and E. M. Sternberg, "Development of a sensitive microarray immunoassay for the quantitative analysis of neuropeptide Y," *Anal. Chem.,* vol. 84, pp. 6508-6514, 2012.

[103] R. E. Fernandez, B. J. Sanghavi, V. Farmehini, J. L. Chávez, J. Hagen, N. Kelley-Loughnane and N. S. Swami, "Aptamer-functionalized graphene-gold nanocomposites for label-free detection of dielectrophoretic-enriched neuropeptide Y," *Electrochem. Commun.,* vol. 72, pp. 144-147, 2016.

[104] S. Kim, L. Xing, A. E. Islam, M. Hsiao, Y. Ngo, O. M. Pavlyuk and L. F. Drummy, "In operando observation of neuropeptide capture and release on graphene field-effect transistor biosensors with picomolar sensitivity," *ACS Appl. Mater. Interfaces,* vol. 11, pp. 13927-13934, 2019.

[105] R. Magnusson, M. G. Abdallah, K. J. Lee, J. A. Buchanan-Vega, B. R. wenner, J. W. Allen, M. S. Allen, S. Gimlin and D. W. Weidanz, "Guided-mode resonance sensing of neuropeptide-Y with a sandwich assay achieving pg/mL detection," *Proc. SPIE,* vol. 11020, pp. 110200H-1-110200H-6, 2019.

[106] *Available online: http://www.resonantsensors.com (accessed on 12 December 2019).*

[107] M. G. Moharam, T. K. Gaylord, D. A. Pommet and E. B. Grann, "Stable implementation of the rigorous coupled-wave analysis for surface-relief gratings: enhanced transmittance matrix approach," *J. Opt. Soc. Am. A,* vol. 12, p. 1077, 1995.

[108] J. Wang, D. Karnaushenko, M. Medina-Sánchez, Y. Yin, L. Ma and O. G. Schmidt, "Three-dimensional microtubular devices for lab-on-a-chip sensing applications," *ACS Sens.,* vol. 4, pp. 1476-1496, 2019.

[109] Y. Wan, Y. Kim, N. Li, S. K. Cho, R. Bachoo, A. D. Ellington and S. M. Iqbal, "Surface-immobilized aptamers for cancer cell isolation and microscopic cytology," *Cancer Res.,* vol. 70, pp. 9371-9380, 2010.

[110] M. S. Amin, Y. J. W. and R. Magnusson, "Optical transmission filters with coexisting guided-mode resonance and Rayleigh anomaly," *Applied Physics Letters,* vol. 103, no. 13, p. 131106, 2013.

[111] S. Tibuleac and R. Magnusson, "Reflection adn transmission guided-mode resonance filters," *Journal of the Optical Society of America A,* vol. 14, no. 7, pp. 1617-1626, 1997.

[112] H. Gao, M. M, M. H. Lee, J. Henzie, S. K. Gray, G. C. Schatz and T. W. Odom, "Rayleigh anomaly-surface plasmon polariton resnances in palladium and gold subwavelength hole arrays," *Optics Express,* vol. 17, no. 4, pp. 2334-2340, 2009.

[113] B. Wang and Q. Wang, "An Interferometric optical fiber biosensor with high sensitivity for IgG/anti-IgG immunosensing," *Optics Communications,* vol. 426, no. 1, pp. 388-394, 2018.

[114] K. J. Lee, D. Wawro, P. S. Priambodo and R. Magnusson, "Agarose-gel based guided-mode resonance humidity sensor," *IEEE Sensors Journal,* vol. 7, no. 3, pp. 409-414, 2007.

Biographical Information

Joseph Buchanan-Vega earned a Bachelor of Science in Physics from Grambling State University in 2008. He then attended Louisiana Tech University and received a Master of Science in Physics (2010), and a Master of Science in Molecular Science and Nanotechnology (2011). While at Louisiana Tech University, his research was focused on material science: developing hard and fracture tough ceramics with the use of nanoparticles for applications like bullet proof vests. Joseph went on to teach physics in the Dallas area at a collegiate academy and in a traditional high school setting from 2010 to 2015. He then applied to and was accepted into the Electrical Engineering Ph.D. program at the University of Texas at Arlington. He received the Louis Stokes Bridge to Doctoral Fellowship and was an active fellow in the program from 2015 to 2017. Joseph is a proud member of Alpha Phi Alpha Fraternity, and NSBE.